ABSTRACT

Title of dissertation: SPACE-DEPLOYED, THIN-WALLED ENCLOSURE FOR A CRYOGENICALLY-COOLED HIGH TEMPERATURE SUPERCONDUCTING COIL

Allison K. Porter

Dissertation directed by: Dr. Raymond Sedwick
Department of Aerospace Engineering

The interaction of magnetic fields generated by large superconducting coils has multiple applications in space, including actuation of spacecraft or spacecraft components, wireless power transfer, and shielding of spacecraft from radiation and high energy particles. These applications require coils with major diameters as large as 20 meters and a thermal management system to maintain the superconducting material of the coil below its critical temperature. Since a rigid thermal management system, such as a heat pipe, is unsuitable for compact stowage inside a 5 meter payload fairing, a thin-walled thermal enclosure is proposed.

A 1.85 meter diameter test article consisting of a bladder layer for containing chilled nitrogen vapor, a restraint layer, and multilayer insulation was tested in a custom toroidal vacuum chamber. The material properties found during laboratory testing are used to predict the performance of the test article in low Earth orbit. Deployment motion of the same test article was measured using a motion capture system and the results are used to predict the deployment in space.

A 20 meter major diameter and coil current of 6.7 MA is selected as a point design case. This design point represents a single coil in a high energy particle shielding system.

Sizing of the thermal and structural components of the enclosure is completed. The thermal and deployment performance is predicted.

SPACE-DEPLOYED, THIN-WALLED ENCLOSURE FOR A CRYOGENICALLY-COOLED HIGH TEMPERATURE SUPERCONDUCTING COIL

by

Allison K. Porter

Dissertation submitted to the Faculty of the Graduate School of the
University of Maryland, College Park, in partial fulfillment
of the requirements for the degree of
Doctor of Philosophy
2015

Advisory Committee:
Dr. Raymond Sedwick, Chair
Dr. David Akin
Dr. Christopher Cadou
Dr. Bao Yang
Dr. Kenneth Yu

Acknowledgements

First, I would like to acknowledge my adviser, Dr. Raymond Sedwick. Thank you for your honest guidance, for allowing me to sometimes struggle on my own because you knew I would figure it out (even if I had my doubts), for always being willing to point me in the right direction, for trusting me with responsibilities with high visibility, and for your understanding when I faced hardships.

I would also like to acknowledge my other committee members, Dr. Akin, Dr. Yu, Dr. Cadou, and Dr. Yang for their insight, encouragement, and patience.

I would like to acknowledge everyone from the RINGS team. Many successes of my dissertation stand on the hard work and accomplishments of that project. I especially want to thank Dustin Alinger for putting up with me and having confidence in our work.

Thank you to my lab mates over the years. I look back fondly on our road trip. Thank you for your patience and willing to lend hand with my thermal and deployment tests. Special thanks to my undergraduate students, particularly Scott Kindl and Zach Schwartz.

Shout out to the University of Maryland club water polo team for all the years of laughter and good water polo that made me feel youthful and excited even when I was sleep-deprived and stressed.

I would like to acknowledge two siblings: Nathan and my best friend since second grade, Mawlee Davis. Nathan, thank you for convincing me to take a break from my research to go to Korea together. Your family is my family, and I was able to feel their

love. Mawlee, you are my sister. Your love and support encouraged me from 3000 miles away.

Thank you to Gerard Checchia. You always see the best in me and lift me up when the stress and daily grind feels like too much to bear on my own. I also enjoy having my ego inflated with regards to my cooking skills.

Last, and most importantly, I would like to thank my parents, Gary and Denise Porter. You give me unconditional love and support. You encourage me without ever pushing so that I can feel the satisfaction of finding my own way. I feel grateful and inspired by the sacrifices and struggles you have endured.

This work was partially funded by NIAC contract NNX12AQ59G. Other funding for my graduate studies include NASA contract NNH11CC33C and semesters as a teaching assistant for ENAE 457 thanks to Dr. Lee who was always excited to see me and ask about my research progress.

Table of Contents

List of Figures

Table of Tables

Chapter 1: Introduction

The ability to deliver to space and operate large superconducting coils is an enabling technology for non-conventional applications of interacting magnetic fields. Utilizing superconducting material is appealing for its high current density and zero resistivity. The development of second generation (2G) high temperature superconducting (HTS) wire into a thin tape increases the feasibility of developing large superconducting coils. Commercially available superconducting tapes such as the 2G-HTS wire manufactured by SuperPower® boasts current densities as high as 459 A/mm^2 at a temperature of 77 K with a minimum bend diameter of 25 mm [1]. This minimum bend diameter is important for compact stowage and deployment since rigid coils with diameters greater than 5 meters will not fit in typical launch vehicle fairings. Flexibility of the superconducting layer allows for compact stowage during launch and deployment in space.

Superconducting materials must remain below a critical temperature to reach zero resistivity and achieve optimum performance. In order to operate at temperatures as low as 77 K, a cryogenic cooling system is required. This dissertation identifies a thin-walled torus as a solution for enclosing a superconducting coil at cryogenic temperatures. Thin-walled structures are appealing because they achieve a large ratio of deployed-to-stowed volume with lightweight materials. The work discussed in this dissertation presents the development a system concept of a thin-walled enclosure capable of deploying in space for the use of containing and cooling a high temperature superconducting coil.

1.1 Motivation

Three particular space applications of a superconducting coil will be discussed in the following sub-sections. Despite the differences in the mission objectives, each application utilizes the interaction of strong magnetic fields generated by coils with major diameters greater than 5 meters.

1.1.1 Applications for actuation of spacecraft and components

The use of interacting magnetic dipoles for maneuvering spacecraft was patented by Daniel Villani of Hughes Electronics Corporation in 2000 [2]. Large magnetic dipoles can be generated by circulating current in a coil attached to a spacecraft. The two or more free-flying spacecraft equipped with these coils can produce forces and torques that change position and/or orientation relative to the other spacecraft.

This concept has been thoroughly examined by the Space Systems Laboratory at Massachusetts Institute of Technology (MIT-SSL), calling this technology electromagnetic formation flight (EMFF). One system, referred to as a micro-EMFF testbed, utilized 0.25 meter-diameter coils of 25 turns made from power transmission cables and achieved impulses above 1 N-s at an axial separation distance of 0.25 m [3]. The testbed consisted of two identical vehicles. One vehicle was hung from the end of a boom such that the plane of the coil was orthogonal to the floor while the second vehicle was held in a fixed location as shown in Figure 1.1a. The boom was free to rotate using an air-bearing at the center of the boom and a counterweight on the opposing end. Both vehicles were able to pivot about

the vertical axis relative to the floor (through the center coil plane) to allow for alignment of the coils during axial repulsion.

A free-floating testbed was developed by the University of Maryland Space Power and Propulsion Laboratory (UMD-SPPL) and MIT-SSL. The testbed consists of two aluminum coils with a major inner diameter of 75 cm and 100 turns (20 wide, 5 layer stack). The project called Resonant Inductive Near-field Generation System (RINGS) was delivered to the International Space Station (ISS) in August 2013 to operate in conjunction with the pre-existing SPHERES facility [4]. The enclosure and the coil are a rigid assembly (Figure 1.1b), and rely on forced air convection for thermal cooling. Unlike previous EMFF testbeds, RINGS was capable of operating as a free-floating demonstration with six-degrees of freedom in a micro-gravity environment. The system relies on non-superconducting coils for operation which limits the performance compared to the expected performance of a system using superconducting coils.

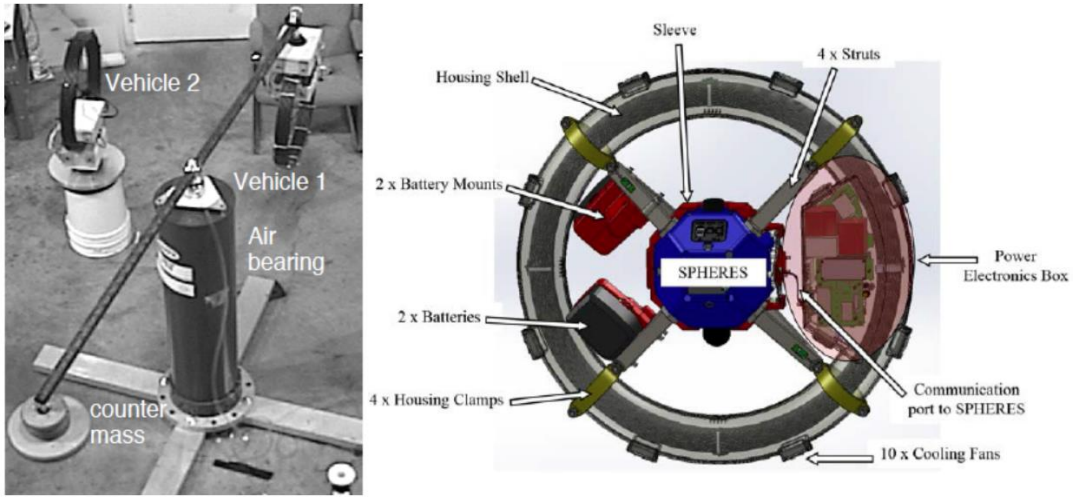

Figure 1.1 a) micro-EMFF testbed [3] and b) free-floating EMFF test [4] for non-HTS coil operation

Ground tests using high temperature superconducting wire have also been demonstrated using two vehicles equipped with a pair of orthogonal coils [5]. Similar to the previous micro-EMFF experiment, one vehicle was held at a fixed location while the other vehicle moved relative to it using compressed carbon dioxide through a tripod of air bearing pucks above a flat surface table as shown in Figure 1.2.

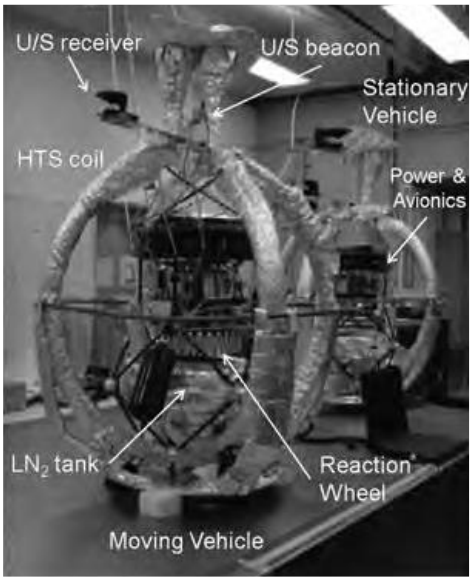

Figure 1.2 Flat floor EMFF testbed using pairs of orthogonal HTS coils [5]

Advances in EMFF have elevated the technology by developing testbeds that have led to characterization of the forces and torques and concurrent maturation of the control algorithms necessary for full on-orbit operation. However, the progression of EMFF hardware falls short in comparison due to the inability to deliver HTS coils of the size required to maneuver most satellites. Development of a deployable HTS coil with a proper cryogenic thermal management system would satisfy this need.

1.1.2 Applications for wireless power transfer

By oscillating current in two coils at the same frequency, power transfer via resonant inductive coupling can be achieved. The concept of inductive coupling was first introduced by Nikola Tesla [6]. The magnetic field produced by the current driven in one

coil (referred to as the “primary” coil) induces a current in the other coil (referred to as the “secondary” coil) in the same way as a traditional transformer. By moving to superconducting material of the coil, and thus eliminating resistive losses, power transfer efficiency was shown to increase when operated at low frequencies [7].

Wireless power transfer using resonant inductive coupling has multiple applications in space. Power generated by one or many spacecraft can be delivered to other spacecraft equipped with coils, but not necessarily gathering their own power. The hardware developed for RINGS is also capable of operating as a testbed for wireless power transfer. In axial alignment and approximately 0.5 meters of separation, power transfer of 30% was demonstrated during an ISS test session [4]. In addition to resistive losses from the use of non-superconducting material, the proximity effect hindered the performance of the system due to the compact geometry of the coil, which consisted of five flat spirals stacked axially and connected in series [8].

1.1.3 Shielding against high energy charged particles

The use of superconducting coils for protecting a spacecraft from high energy charged particles such as solar energetic particles (SEP) and galactic cosmic rays (GCR) was proposed as early as 1961 [9]. While there was debate about the specific configuration of the coils and expected shielding efficiency, advancements in superconducting materials lagged behind, leaving configurations at the theoretical and modeling stages of the design process.

Chapter 1: Introduction

In 2009, Shepard and Shepard proposed a magnetic shield using superconducting coils of various diameters vertically stacked to form a toroidal volume for the purpose of shielding during human space travel [10]. The paper points out the downfalls of a single current loop for magnetic shielding due to the failure to protect against particles traveling along the central axis normal to the plane of the coil as proposed by F.H. Cocks in 1991 [11] and reviewed with further analysis in 1997 by J.C. Cocks et al. [12]. In the design, the spacecraft would be enclosed in the volume of the toroid. A cross-section of the minor diameter of the axially symmetric spacecraft is shown in Figure 1.3b, where the volume for human occupancy is indicated by the dark shaded region. Since the primary application was for human space travel, the paper by Shepard and Shepard also addressed magnetic field strength effects on astronaut health. The recommended static field strength is 70 mT according to the National Radiological Protection Board (NRPB) based on an eight hour workday [13]. To achieve this, a second stack of current loops was placed in the toroid such that the resultant field strength of the toroid was low. Figure 1.3 shows the shielding current loops with current directed in the negative normal to the cross-section plane while the field canceling loops have current flowing in the positive normal direction. The combined external field of the toroid and single coil provided the magnetic shielding against incoming high energy charge particles.

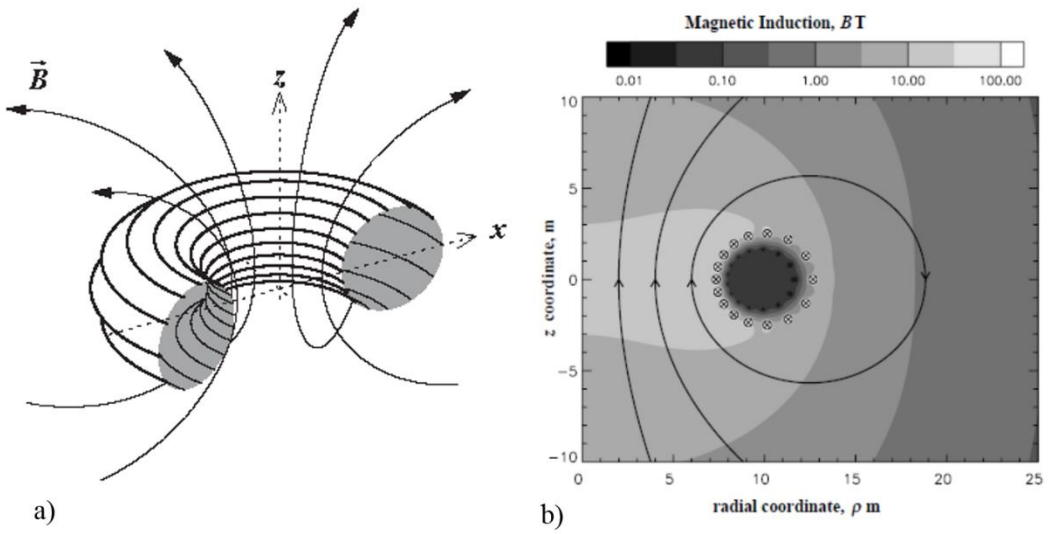

Figure 1.3 Current loops stacked form toroidal enclosure a) isometric cross-section view b), b) magnetic induction for cross-section of minor diameter [10]

A design involving multiple tori was separately proposed with a slightly different design that provided magnetic shielding (Figure 1.4), but also kept field strength levels at a safe level for human occupancy [14]. This design had the spacecraft in the center hole of the tori rather than enclosed by torus surface area. Figure 1.4b shows a side view of the tori creating a cylindrical volume for the spacecraft. A computational model was used to determine the shielding efficiency of charged particles with energies of 0.1 GeV, 1 GeV, and 2 GeV. Of the three configurations examined, the use of a second set of tori nested inside the first layer provided the best shielding efficiency for the 1 GeV and 2 GeV energy levels while still providing above 99% shielding efficiency for the 0.1 GeV particles [14]. This configuration would be challenging for deployment because the wire windings are wrapped around the minor diameter of the torus rather than circumferentially in the plane of the torus like that of Shepard and Shepard.

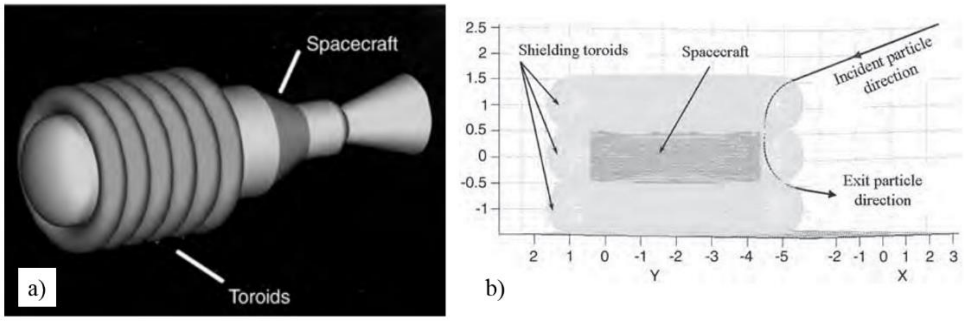

Figure 1.4 a) Concept view of stacked tori, b) side view of with region safe for human occupancy indicated [14]

In contrast, Joshi proposed using a combination of charged spheres and a current loop to produce a spherical shielded region from particles of 1 GeV at 70% efficiency [15]. The discussion focused primarily on the modeling and computation to estimate performance of a system of that configuration. It failed to address the feasibility of how to implement the delivery of hardware to space. The coil described in the design would need to be sufficiently large to fit around the equator of a spherical habitat with a diameter of 20 m shown in Figure 1.5.

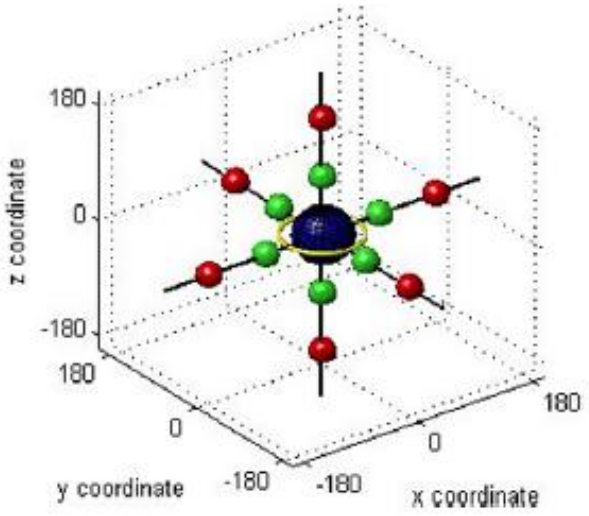

Figure 1.5 Spacecraft in blue, shielded by current loop in yellow and charged spheres in green and red [15]

While the scale and wrapping of the coil vary, all of these proposed magnetic shielding designs could strongly benefit from development of a deployable superconducting coil due to their size.

1.2 Contributions

The contributions of this dissertation are as follows:

1. Presents a concept for deployable thermal enclosure for an HTS coil
2. Develops a method for experimentally determining thermal properties of a thermal enclosure test article using a limited number of locations for measuring temperature
3. Identifies an optimal flight design for a specified requirement set by trading thermal system dimensions and mass with power system mass

4. Uses correlated static and dynamic deployment testing to develop a model for predicting deployment motion in space
5. Identifies several candidate self-healing technologies to address puncture vulnerability

1.3 Outline of dissertation

This dissertation is organized into three primary topics: a thermal investigation, a deployment investigation, and an example system design.

Chapter 2 starts with a literature survey of related technologies which leads into an overview of the thermal enclosure concept. The previous research conducted on thermal management systems leads to the decision to develop a thin-walled enclosure. The chapter also explains the basic fabrication of the test article used in subsequent laboratory tests.

The thermal investigation in Chapter 3 includes testing of a 1.85 meter diameter enclosure in a toroidal vacuum chamber. The thermal material properties of the test article are found using a limited number of locations for measuring temperature. A model that predicts the thermal performance of the test article in space is discussed.

Similarly, the deployment investigation in Chapter 4 starts with using laboratory testing results to find an effective spring constant and damping coefficient. Static tests for a straight sample test section are performed and the results are compared with the dynamic motion of the full test article. Using the properties of the test article, a model is used to predict the dynamics for deployment in space.

Chapter 1: Introduction

Chapter 5 ties together the conclusions made in Chapters 3 and 4 for a specific point design case. The point of interest is identified and the performance is outlined based on the laboratory test article properties. The design space is further examined by looking at the influence of changing certain properties to better match values expected of materials used in flight missions. Lastly, a literature survey is conducted for addressing the vulnerability of a thin-walled gas enclosure to damage due to punctures.

Chapter 2: Concept Overview

2.1 Related work on thermal management systems

The following sub-sections summarize relevant work on thermal management systems that drove the overall concept of the thin-walled, deployable enclosure. Previous investigations also provided useful insight into fabrication of the thermal insulation and feasibility of extracting heat with a cryocooler.

2.1.1 Heat pipe

Heat pipes are an appealing thermal management tool in space because they passively extract heat, and since the working fluid is not a consumable, the lifespan is relatively high. Despite extensive research on heat pipes, there are few investigations that directly advance the feasibility of maintaining a large coil below cryogenic critical temperature of the HTS material that is also capable of compact stowage. While no single research investigation has previously satisfied all of these needs, separate related work has been done.

The Cryogenic Flexible Diode Heat Pipe (CRYOFD) demonstrated by the Air Force Research Laboratory during the Space Shuttle missions STS-83 and STS-94 in 1997 used oxygen and methane working fluids contained in a stainless steel bellow of 3/8 inch outer diameter with a bend radius of 2.7 inches to maintain temperatures between 60 and 145 K (for oxygen), and between 95 and 175 K (for methane) [16]. This showed that a flexible heat pipe could achieve cryogenic temperatures necessary for the operation of an

HTS material. However, the flexibility was limited to the purpose of component vibration isolation so the design is not transferrable to a large toroidal coil.

In contrast, a toroidal cryogenic heat pipe with nitrogen as the working fluid has been demonstrated with intended applications for HTS coils [17]. The path of the heat pipe followed a closed circular loop with a major diameter of 2 m, closer to the size of a potential space operated HTS coil. The HTS coil was enclosed in the core of the heat pipe, rather than an external thermal connection like conventional heat pipes. However, the toroidal heat pipe was rigidly constructed using copper tubing as the outer envelope, making it incapable of deploying for applications that require major diameters in excess of a payload fairing's dimensions.

Given the current state of cryogenic heat pipes, it does not seem feasible to develop a heat pipe flexible enough to compactly stow a coil capable of the missions described in Section 1.1 with a deployed diameter of 5 meters or larger. By shifting to a vapor cooled system using nitrogen as the cryogen, a thin-walled enclosure for the HTS coil with a high stowed deployed volume expansion ratio is found to better satisfy the needs of the target applications.

2.1.2 Multilayer insulation blanket

Multilayer insulation blankets (MLI) were a key technology to the success of the human space exploration and lunar missions. The blankets are an effective method of passive radiation shielding, using highly reflective surfaces separated by insulative materials with low surface contact between layers to reduce thermal conductivity. The

resultant product typically consists of many thin layers of the reflective material (often metals deposited on plastic film) alternated with a spacer material. Figure 2.1 shows the percentage of total heat flux for radiation compared to conduction through the solid insulation material and the gas between layers for 1D heat transfer through slabs of material with the cold bounded wall at 123 K and the warm bounded wall at 273 K [18].

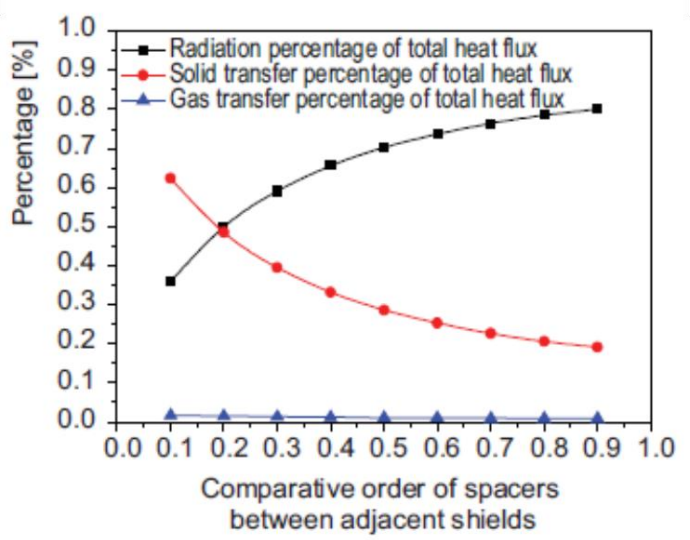

Figure 2.1 Fraction of heat flux due to radiation and conduction between cold wall at 123 K and warm wall of 273 K [18]

For this investigation, the convection due to the gas between layers was neglected. The spacers are the insulative material between reflective surface (shield) layers to prevent direct thermal contact. The shield was a thin deposition of aluminum (0.03 and 0.05 micrometers) on a sheet of polyester film (6 to 12 micrometers) with polyester netting acting as the spacer material. The insulative material conducted thermally in parallel with the conduction through gas. However, as the ratio of shield contact area for gas over

insulation, spacer material, increased beyond 0.2, the radiation heat flux dominated as the primary mode of heat transfer [18].

A study by Neumann that examined MLI for thermally insulating a flexible cryostat found that maintaining sufficient space between the cold wall and the MLI was necessary for good performance [19]. In an experiment comparing the insulation of a cold cylinder, it was found that using a wire mesh to separate two blankets (12 layers each) wrapped around the cold cylinder reduced heat flux into the cylinder by 25.8% compared to a reference case where the same blankets were wrapped directly on the cylinder. This showed that the spatial configuration needed to be considered, in addition to the number of layers. Based on experimental results, an annular design was proposed that used rods and supporting rings to create space between boundary walls and separate two blankets shown in Figure 2.2.

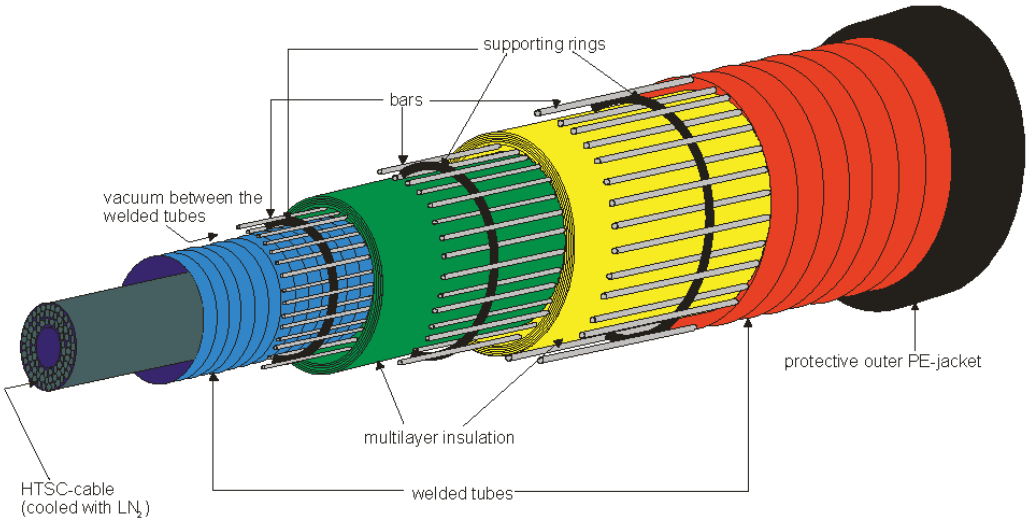

Figure 2.2 Flexible cryostat for HTS power cables using rods and support rings to separate insulation layers [19]

Chapter 2: Concept Overview

The construction of a multi-layer insulation blanket is not simply composed of the shielding reflective layers and the insulative spacer material. An official guideline document for construction of flight multi-layer insulation blankets by NASA asserts that an outer cover and other layers are often used over the insulation blankets. The outer layer, with a possible reflective backing, protects the blanket from "shedding, flaking, and other forms of particulate generation" [20]. Materials listed as suitable for NASA missions included beta cloth, Teflon®, Tedlar®, and Kapton®. The surface properties are necessary for determining the overall heat transfer capability of the blanket.

For applying multilayer insulation, the design will require many seams to follow the curved geometry of a torus enclosure. Experimental data shows that seams create thermal shorts due to conduction through the thread material and increased contact caused by the stitch at the seam location [21,22,23]. In an experiment conducted by Lin et al, it was found that the temperature difference between the inner and outer blanket layers was reduced near the seams, resulting in a larger heat flux in the vicinity of the seams [23]. A MLI blanket was used to thermally protect components on the Cassini spacecraft. The stitching at the seam caused the temperature of the inner layer (warm side) to decrease and the temperature of the outer layer (cold side) to increase. While the main purpose of this blanket was to keep components warm by reflecting radiated heat back onto the spacecraft, the temperature difference observed between the warm and cold sides at the seam compared to the center of the blanket is applicable for a blanket that radiates incident heat away from the spacecraft.

Another practical feature often required during MLI blanket fabrication is the overlapping of two adjacent blanket edges, which is also a source of heat leaking [21,22]. The simple overlap (Figure 2.3b) is often undesirable despite being the easiest to implement because the cold inner layer of the top blanket would come in contact with the warm outer layer of the bottom blanket, leading to large thermal conduction across the seam boundary. In contrast, the interleaved overlap (Figure 2.3a) keeps the corresponding layers of the two blanket edges in contact with each other to prevent thermal shorting across the seam boundary, but this method is much more labor intensive. The butted and outward overlap (Figure 2.3c) offers a middle ground by mating the two cold inner layers with the seam edge pointing outward to prevent thermal shorting of the warm side from the cold side. However, this configuration exposes the edge to the warm surroundings.

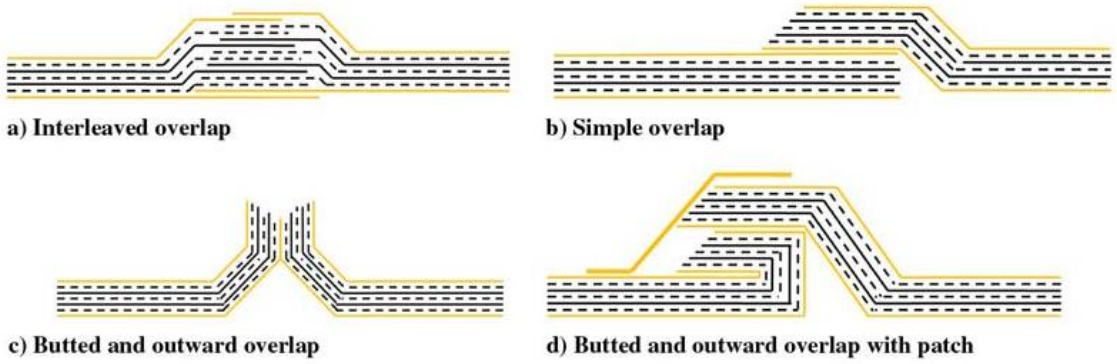

Figure 2.3 Overlap configurations for MLI [21]

A study by Okazaki et al. experimentally measures the effect of a patch that covers a folded over, butted outward overlap (configuration shown in Figure 2.3d) compared to a simple overlap or a butted outward overlap with no seam [21]. The heat flux due to

radiation was assumed constant for all three overlap configurations and determined using analytical methods. The radiation was then subtracted from the total heat flux to determine the combined heat flux due to solid and gas conduction. As expected, the simple overlap allowed the highest heat flux through the seam. The butted and outward overlap without a patch reduce the heat flux by over 63% compared to the simple overlap [21]. By adding the thermal control tape as patch on top of the overlap region, a reduction of the heat flux by 91.5% was achieved [21].

The use of multilayer insulation blankets is very common for spacecraft thermal management. Previous studies related to blanket features, fabrication, and material selection will influence the design details of a thermal management system for a deployable enclosure.

2.1.3 Cryocoolers

Cryocoolers are a popular method in laboratory and space applications for obtaining cryogenic operation temperatures, typically consisting of a regenerator stage and heat exchanger stage. The first NASA mission to use a cryocooler in space was the Upper Atmospheric Research Satellite (UARS) in 1991 [24]. There are several types of cryocoolers with different advantages and disadvantages. Selection is typically dependent upon the refrigeration power required and the operation temperature, but efficiency and mass should also be considered.

The summary of a literature survey is presented to show the state-of-the-art cryocoolers that have cold tips near the critical temperature of HTS material. Table 2-1

lists the cooling power of the cryocoolers from values as low as 0.7 W [25] to and up to 300 W [26]. For better comparison of cryocooler performance across a wide range of refrigeration power, it is useful to examine the efficiency as a percent of the coefficient of performance. The Carnot coefficient of performance (COP) is the COP of the Carnot refrigeration cycle, or reverse Carnot cycle as given by (2-1).

$$COP = \frac{T_{refr}}{T_{rej} - T_{refr}} \tag{2-1}$$

As expected, the coefficient of performance is a function of only the cold tip temperature (T_{refr}) and the rejection temperature (T_{rej}). This ideal COP can be compared to actual refrigeration COP is given by (2-2).

$$\gamma_{refr} = \frac{P_{refr}}{P_{comp}} = \frac{1}{SP_{refr}} \tag{2-2}$$

The COP is the ratio of the refrigeration power (P_{refr}) over the compressor or electrical input power (P_{comp}). Some literature refers to the inverse of this ratio as the specific power. The ratio of the refrigeration COP (γ_{refr}) over the Carnot COP gives the percentage of actual COP compared to the ideal. This is sometimes referred to as the percentage of Carnot COP, and serves as way of comparing the performance of different cryocoolers that may have different operating temperatures and different cooling capabilities. Table 2-1 lists the percentage of COP which ranges from a low of 3.9% for the TRW pulse tube cryocooler developed by Northrop Grumman with a cooling power of 1.5 W at 56 K [27] to a high of 19.6% for the CryoTel® CT Stirling cryocooler developed by Sunpower, Inc. with a cooling power of 11 W at 77 K [28]. For the thermal loading

predicted in Section 3.2.4, the two cryocoolers with cooling power of 15 W should be considered. Interestingly, the mass of the LPT 9710, a pulse tube type developed by THALES Cryogenics [29], is five times heavier compared to the CryoTel® GT, a Stirling type developed by Sunpower, Inc. [28], despite the CryoTel® GT achieving a higher percentage of Carnot.

Table 2-1 Summary of cryocooler state of the art suitable for HTS applications

Model #	Type	Cooling Power (W)	Cold Tip (K)	Input Power (W)	Hot Side (K)	% of COP	Mass (kg)	Manufacturer	Source
Ricor K508	Stirling	0.7	77	12	233	12.3	0.45	CheMin & Ricor	[25]
	pulse tube	1.2	80	42	300	7.9	0.9	Northrop	[32]
TRW	pulse tube	1.5	56	92	190	3.9	8.2*	Northrop	[27]
MPTC	pulse tube	1.6	70	50	288	10.0	2.8	Air Liquide	[34]
RS1	Stirling	3.3	58	108	300	12.7	14	Raytheon	[30]
CryoTel MT	Stirling	5.0	77	80	296	17.8	2.1	Sunpower	[28]
	pulse tube	6.5	67	165	300	13.7	5.0	Northrop	[35]
	turbo Brayton	7.1	73	375	278	5.3	18*		[36]
CryoTel CT	Stirling	11.0	77	160	296	19.6	3.1	Sunpower	[28]
LPT 9710	pulse tube	15.0	80	300	296	13.5	16	THALES Cryogenics	[29]
CryoTel GT	Stirling	15.0	77	240	296	17.8	3.1	Sunpower	[28]
	pulse tube	200.0	70	8600	300	7.6	190*		[31]
HTS-3	pulse tube	300.0	80	4300	300	19.2	114*	Praxair Inc.	[26]

*Calculated using Equation (2-3) [33]

Other cryocoolers included are RS1 made by Raytheon [30] and pulse tube with large cooling power of 200 W [31]. The cryocooler with the smallest mass listed in Table 2-1 is a pulse tube type developed by Northrop Grumman, with a modest cooling capacity of 1.2 W and operating at 7.9% of the Carnot COP [32]. The cryocooler mass was not available for all of the cryocoolers examined in Table 2-1; however, a relationship proposed by Ladner, shown in Equation (2-3), the total cryocooler mass in kilograms as a

function of input power for single stage pulse tube and Stirling cryocoolers. This can be used to estimate an expected mass for input powers between 50 W and 200 kW [33] as shown by the blue line in Figure 2.4.

$$M_{cryo} = 10\text{^}\{-5.5260E(-02)\left(\log\left(P_{comp}\right)\right)^3 + 5.565E(-01)\left(\log\left(P_{comp}\right)\right)^2 - 1.0931\log\left(P_{comp}\right) + 1.3315\} \quad (2\text{-}3)$$

The mass and input power for several cryocoolers (complete list specifications in Appendix A: Cryocooler survey) are indicated by red circles, also in Figure 2.4, which shows a close correlation between the data and the trend line given by Ladner. This allows for a prediction of cryocooler mass for coolers where the mass was not reported. They are marked with an asterisk in the table to indicate that the mass is a calculated value.

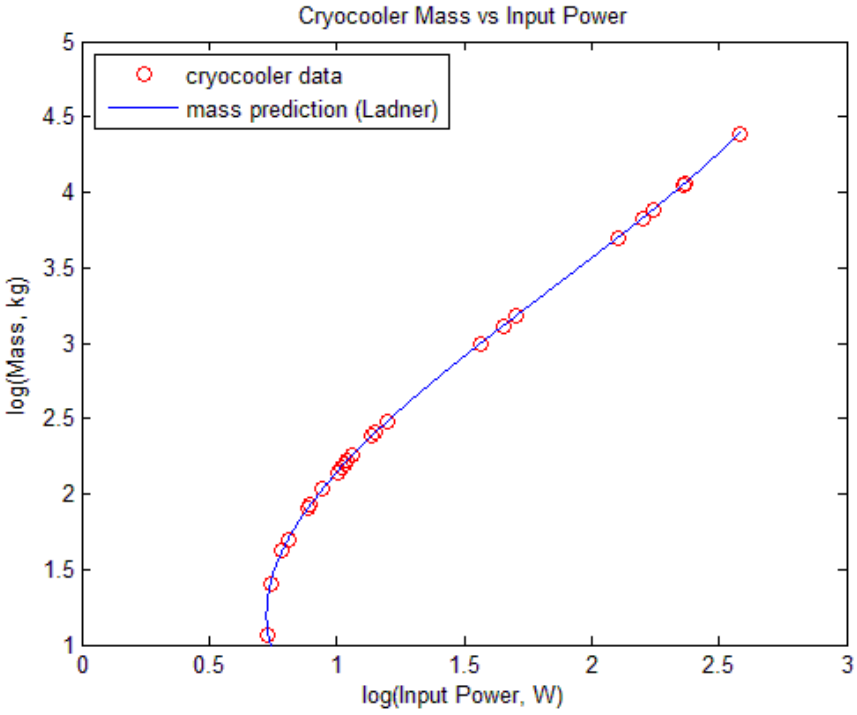

Figure 2.4 Mass and input power for recent cryocoolers compared to trend by Ladner [33]

Only five of the cryocoolers included in Table 2-1 were developed for space applications or have been successfully operated on a space mission. Research regarding state-of-the-art cryocoolers primarily focuses on delivering cooling power of less than 1 W to maintain temperatures of 4 K, which is a different operation range than what is necessary for an HTS coil. The TRW pulse tube was developed to provide cooling to the Atmospheric Infrared Sound (AIRS) instrument on the NASA Aqua spacecraft, which launched in 2002 with over six years of operation in space [27]. The Miniature Pulse Tube Cooler (MPTC) developed by Air Liquide was a component on the ESA Sentinel-3 mission with 5260 operating hours as of April 2008 [34]. Northrop Grumman demonstrated that a coaxial

pulse tube cryocooler similar to the coolers that flew as part of the Japanese Advanced Meteorological Imager (JAMI) in 2005 and the Thermal and Near Infrared Sensor for Carbon Observations (TANSO) payload on the GOSAT in 2009 could achieve 6.5 W cooling at 65 K [35]. The cryocooler with the highest cooling capacity for space applications listed in Table 2-1 is the turbo-Brayton, capable of 7.1 W at 73 K while achieving 5.3% of the Carnot COP for the Near Infrared Camera and Multi-Object Spectrograph (NICMOS) installed on the Hubble Space Telescope during a service mission in March 2002 [36]. Though not developed for a spacecraft, the Ricor K508 Stirling cryocooler was included in the Mars Science Laboratory design for cooling the Chemistry Mineralogy (CheMin) instrument [25].

2.2 Related work for deployed inflatables

Inflatable structures have been extensively researched for aerospace applications. The applications range from using inflatables as a habitat during space travel and exterritorial missions to using inflatables as a structural component [10,37,38]. Inflatables are related to a thin-walled thermal enclosure due to the common need to contain a gas after deployment in a space environment. Of these numerous examples of inflatables in aerospace, there are only a few instances of a toroid being utilized, which will now be discussed.

The In-Space Technology Program (IN-STEP) managed an experimental antenna array that utilized three inflatable booms and an inflatable torus to deploy a large antenna array [39,40,41,42]. The project, called the IN-STEP Inflatable Antenna Experiment (IAE),

was demonstrated on-orbit during the space shuttle Endeavour mission STS-77 and deployed from the Spartan 207 free-flying test spacecraft [42]. The three inflatable booms and torus were used as deployable structures for supporting a 14-meter diameter parabolic reflector [39]. The torus served as a surface for attachment points of the parabolic reflector. The experiment focused on the dynamic response of the structure during deployment and the final precision of the parabolic reflector after deployment. The antenna array assembly was compactly stowed in a canister compartment on the Spartan spacecraft. The initial deployment was initiated by a spring loaded plate inside the canister. The structure slowly unfolded due to the stored strain energy of the material before reaching the final configuration using nitrogen gas shown in Figure 2.5a. The struts and torus were manufactured using Kevlar® fabric coated with neoprene rubber with three layers of multi-layer insulation (MLI) for passive thermal management. The torus experienced a temperature swing from 20 °C to -10 °C as the Sun became occulted by Earth [42]. The results of the IN-STEP IAE are significant because it was an on-orbit demonstration of a nitrogen-inflated torus. Even though it was primarily a structural component and the inflation gas was not at cryogenic temperatures, it bolstered the feasibility of deploying a thin-walled, toroidal thermal enclosure.

In 2001, a paper by Huang detailed a separate effort by NASA at the Jet Propulsion Laboratory to fabricate test articles of inflatable antenna arrays [43]. These test articles supported flat reflectors rather than a parabolic reflector like that of the IN-STEP IAE. Multiple inflatable array frame shapes were tested, including a 1-meter diameter X-band

array consisting of 15 straight segments shown in Figure 2.5b. Similar to the IN-STEP IAE, the material for the inflatable was Kevlar®, but coated with urethane instead of neoprene rubber. Although it was not implemented for this particular test article, it is heavily suggested that an on-orbit system would be capable of becoming rigid after deployment. This study includes two competing approaches for an L-band synthetic-aperture radar (SAR) using inflatable tubes connected to form a rectangular frame. One approach used urethane-coated Kevlar® like the X-band array while the other approaches used thin aluminum. The aluminum was stretched just beyond the yield point during inflation to become rigid. It was noted during testing that while the resultant rigid tubing did not need gas pressure to be constantly applied to retain its inflated shape, the structure was unable to support non-axial or bending loads. Other suggestions for rigidization were made including the use of polymers that cure due to ultra-violet radiation and cold temperatures, or fabric impregnated with “hydro-gel” resin that hardens when the water content evaporates. These techniques could also protect the inflatable structure from small debris or punctures that threaten the operation of a vapor-cooled cryogenic system.

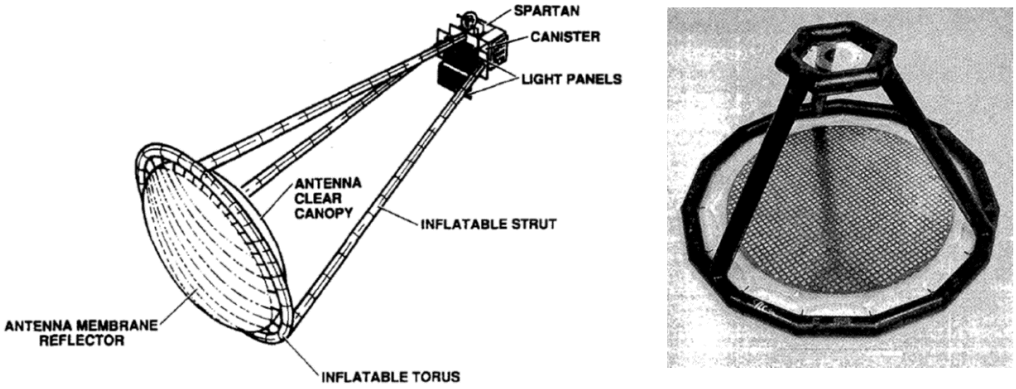

Figure 2.5 a) IN-STEP IAE on-orbit assembly [40], b) X-band flat array [43]

The dynamics of deployment have also been a focus of several other inflatable tori for space applications. The Marshall Space Flight Center completed a series of ground tests for "five full-scale inflatable structures ranging in size from approximately 2 to 6.5 m" between the years 1997 and 2000 [44]. The material for the tori was Kapton®. All torus sizes required gas pressure to be constantly applied to maintain inflation due to leaks in the structure, either due to seams or small punctures. The low stiffness of the structure made it difficult to measure the dynamic response in the laboratory environment due to unintended disturbances, such as the gas flow, for maintaining inflation and ambient air flow.

A computational analysis of the expected dynamic response of a torus due to vibration was performed by Gajbhiye et al. using a finite element formulation [45]. Like the tori built by Marshall Space Flight Center, Kapton® was used for the shell material while comparing the results for two models over a range of aspect ratios (minor cross-sectional diameter over mean ring diameter). The first model was an empty torus shell

with material properties defined by the expected stiffness due to inflation pressure. The second model was the same material shell, but included air as the enclosed gas. The study identified the mode shapes and patterns of the tori, and the natural frequencies that excited particular modal patterns for three inflation pressure. It was found that the number of modes increased and the natural frequency corresponding to particular modal patterns decreased with increased aspect ratio [45]. The major toroid diameter was fixed so the aspect ratio was varied by changing the cross-sectional minor diameter.

Overall, the work on inflatables has focused on providing structural support to spacecraft or components. This differs from the challenge of using the inflatable as a thermal enclosure. However, the development of similar inflatable geometries to the toroidal design of interest adds confidence to the concept of a thin-walled thermal enclosure design discussed in this work.

2.3 Design concept and test article fabrication

After considering previous research, a thermal enclosure concept was designed. A test article used for the thermal and deployment investigations was fabricated based on this concept.

The HTS coil is housed within a toroidal enclosure. Nitrogen vapor is used to extract heat from the HTS coil. The enclosure consists of many material layers shown in Figure 2.6. The inner-most layer is a bladder layer supported by a restraint layer around it. The outer-most layer of multi-layer insulation blankets provides passive thermal radiation shielding. The blankets are attached as overlapping panels to allow for them to bow out

when the enclosure is compressed into its stowed state. The circular structure of the minor diameter cross-section is maintained by large compression springs lined up in series inside the bladder. The springs provide a force to achieve deployment, as well as a rigid mounting point for suspending the coil in the nitrogen vapor. The inner assembly, consisting of the coil, springs, bladder, and restraint layers, is attached to angled collar pieces. The collars constrain the ends of the springs and help define the shape of the enclosure as a segmented torus with straight sides as shown in Figure 2.7.

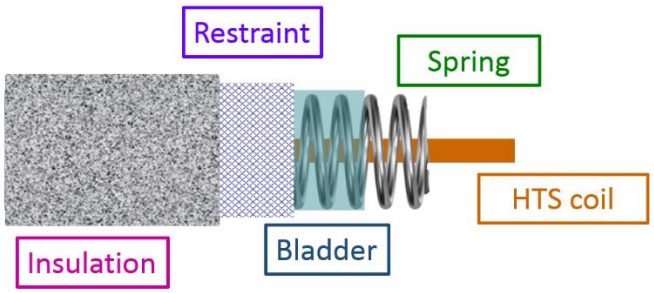

Figure 2.6 Concept design of material layers (side view)

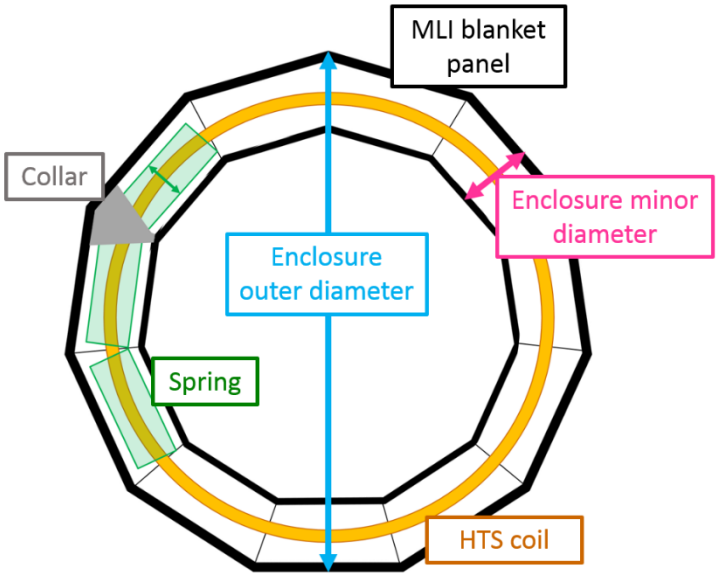

Figure 2.7 Concept drawing of coil contained within segmented torus (top view)

2.3.1 Concept for compact stowage of HTS coil

This concept is feasible due to recent development in Type-II superconductors, also known as high temperature superconductors, which have resulted in wire shaped in a thin ribbon form. The thin superconducting materials are supported by substrates that allow for the ribbon wire to bend at a smaller radius of curvature (2.5 cm) than the older Type-II superconductors that were made of thin filaments encased in silver with a minimum curvature radius of 10 cm. The internal structure of the wire for both superconducting wires are depicted in Figure 2.8.

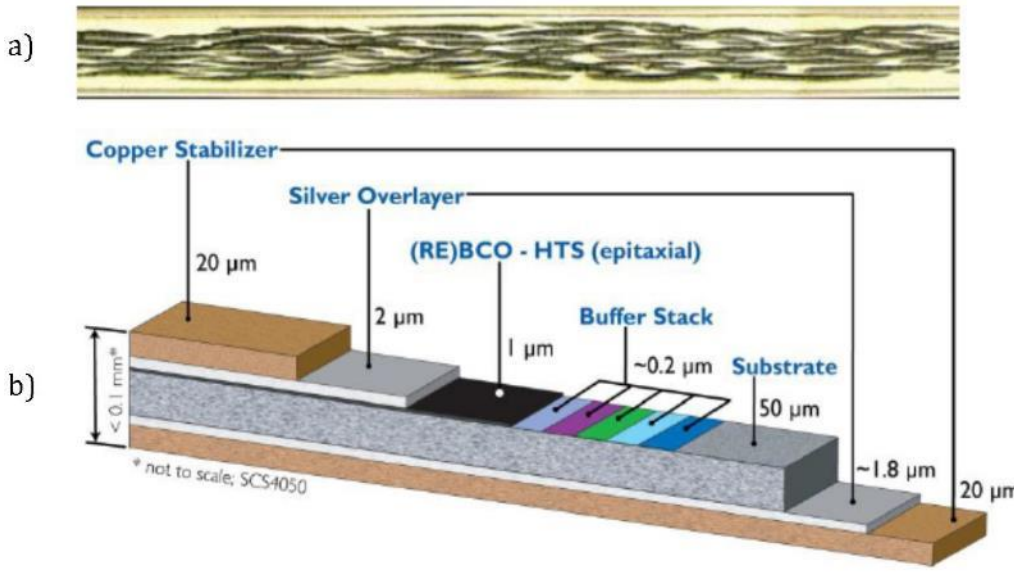

Figure 2.8 HTS superconducting wire a) Generation 1 made by American Superconductor, b) Generation 2 made by SuperPower

The small bend radius of the thin ribbon wire is beneficial for achieving a compact stowed configuration as demonstrated by the concept prototype in Figure 2.9. The red line in Figure 2.9a traces over the curved path of a plastic ribbon used as stand-in material for the superconducting coil. The image in Figure 2.9b shows how the ribbon uncurls to form a nearly circular shape while suspended within the volume of the spring coil. For this proof of concept, four springs were connected to form the torus structure. The plastic ribbon that represented the superconducting coil was held in place by threading it through washers connected to the spring coils using zip ties. Twists in the zip ties encouraged the exaggerated S-curving of the ribbon when the springs were compressed into the stowed configuration.

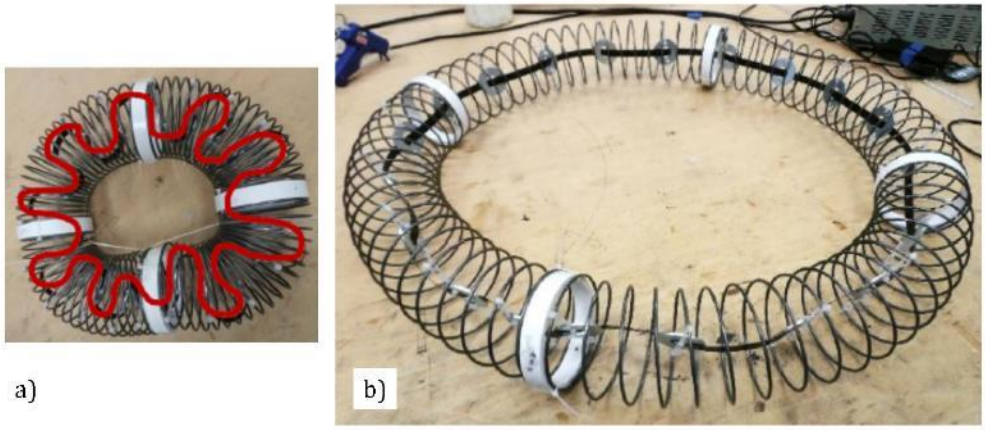

Figure 2.9 Proof of concept of ribbon wire when a) stowed and b) deployed

2.3.2 Fabrication of test article

The full toroidal enclosure was fabricated with the intent to use a pre-existing custom low-vacuum, torus-shaped chamber at the University of Maryland Space Power and Propulsion Laboratory (UMD-SPPL) [5]. The vacuum chamber previously contained a toroidal heat pipe experiment, so the dimensions of the vapor cooled thermal enclosure were primarily governed by the vacuum chamber dimensions. The nitrogen was vapor confined in a double layer bladder of polyethylene plastic. The minimum core diameter was defined by the linear compression springs used to aid in deployment while the maximum core diameter was constrained by a biaxial fiberglass sleeve as the restraint layer, shown in Figure 2.10 (a & b). The bladder diameter exceeded the maximum allowable diameter of the fiberglass sleeve so the pressure forces were transferred to the restraint layer when inflated.

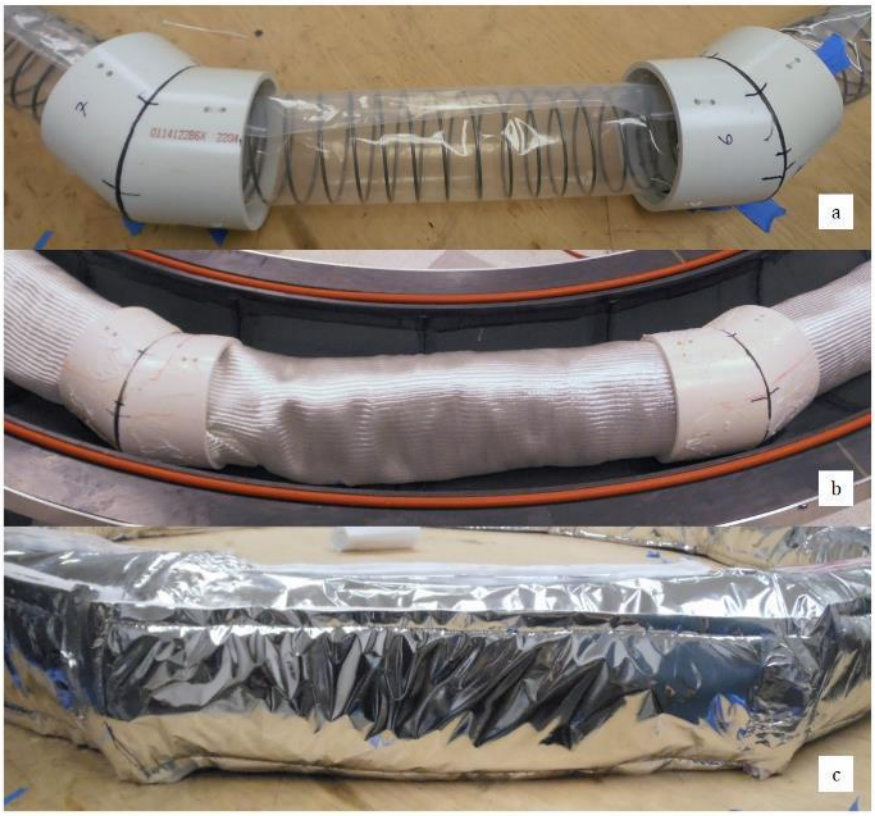

Figure 2.10 Close-up of toroidal enclosure segment with a) inner core, b) fiberglass sleeve over core, c) thermal blanket

An image of the full lab-scale torus, which was built using 11 springs suspended inside larger diameter polyvinyl chloride (PVC) cuffs, is shown at an intermediate stage of construction in Figure 2.11.

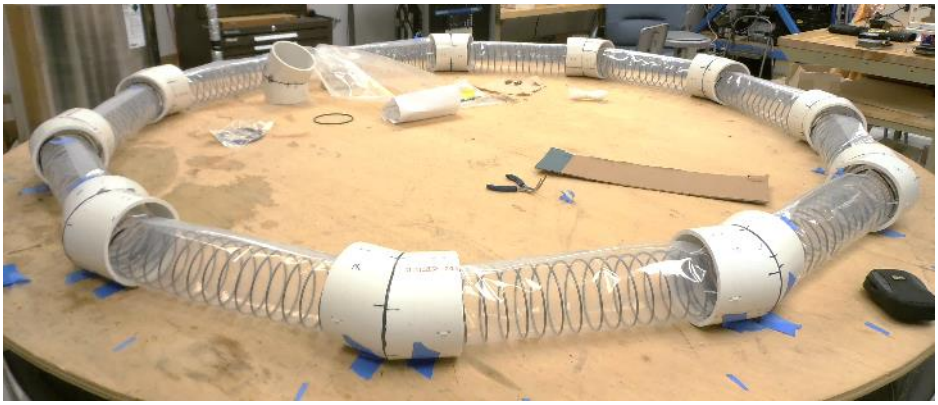

Figure 2.11 Structure of test article

The PVC collars were cut from 5-inch, schedule 80 pipe. The angled collars of the PVC allows for the spring axis to remain straight in the deployed and stowed configuration. The springs are inserted in the bladder layer while the position of the springs relative to the collars are held in place using bands tightly wrapped around the outside of the restraint layer near the ends of the springs. Zip-ties threaded under the band extend radially out to the collars and small holes in the collar lock the position of the spring ends. This allows for the bladder and restraint layers to be a continuous piece, open only where the two ends of the enclosure meet.

The thermal insulation is adhered to the outer surface of the collars. Since the angled collars allow for each spring to compress axially, the blanket pieces lie flat when spanning from one collar surface to an adjacent surface in the fully deployed state. Adhering the insulation to the outer surface of the collars while suspending the vapor containment assembly inside the collars creates a gap between the restraint layer and the

inner most surface of the thermal insulation, reducing heat conduction to the nitrogen vapor.

Flight quality multi-layer insulation was not available for the test article construction since most thermal blankets are uniquely fabricated for each space mission. Custom thermal blankets were made in-house using alternating layers of low density nylon felt and single-sided aluminized polyester film. Each blanket piece was sewn together along the edges. For each collar-to-collar span covered by a single spring length there were four panels of blanket. Each panel was split into an inner and outer stack due to the sewing machine being unable to pass material at the full thickness shown in Figure 2.12. The inner stack consisted of three reflective film layers separated by two layers of nylon cloth. The outer stack also consisted of three reflective film layers alternated with three layers of felt cloth so that the bottom felt layers were in contact with the top reflective film layer of the inner stack. This prevented thermal shorting between the inner and outer stacks of MLI.

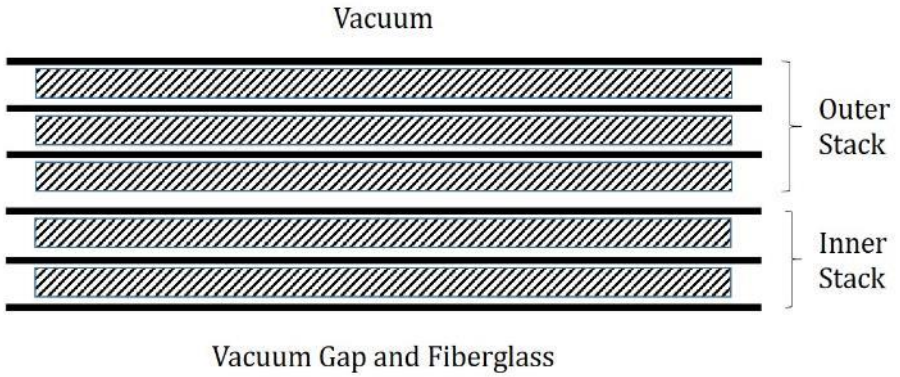

Figure 2.12 Conceptual cross-section showing stack of MLI

The long edges of the panels overlap (concept depicted by the gray regions in Figure 3.3) to prevent any gaps when fully deployed. In the stowed configuration, the center of the panels push out radially from the compressed spring. This prevents the thickness of the blanket layers from restricting the ability of the spring to fully compress. The partial compression of the spring shown in Figure 2.13b demonstrates how the blanket panels bow out in four radial directions using a sample of the enclosure assembly constructed for static deployment force testing using a single spring and the same material layers as the full-sized torus. The top panel in Figure 2.13a is slightly lifted up to show how the edge of the top panel is not restrained by the edge of the front facing panel.

Figure 2.13 Deployed straight thermal enclosure, b) partially compressed

Other design concepts were investigated such as an accordion-inspired folding concept (Figure 2.14), but the four panel design was appealing because it also minimized the labor in constructing the blanket pieces and stitching that created thermal leaking through the insulation layers. The short edges of the blanket pieces located at the collar

seams were butted together (Figure 2.15a) so that the common bottom layers of the stack were touching and then folded over in the same manner as Figure 2.3d. The fold was then covered over using aluminum tape Figure 2.15b. The short edges of the inner and outer stacks were matted together separately.

Figure 2.14 Initial concept for accordion-inspired MLI folding

a b

Figure 2.15 a) Butting of MLI panel short edges of inner insulation stack, b) tape applied to folded seam of outer insulation stack

As previously described, the double bladder layers and restraint sleeve were a continuous piece around the circumference of the enclosure. The edges of the plastic layers

were sealed using fiberglass reinforced packaging tape with the air extracted from between the layers using a laboratory low-vacuum line. This was necessary to prevent undesirable bulging due to air pressure between layers during the pump-down of the vacuum chamber and at the start of pressurized nitrogen vapor flow through the enclosure. The ends of the plastic and fiberglass were strapped to aluminum caps shown in Figure 2.16 and Figure 2.17 using closed cell foam and hose clamps. The end caps also served as the connection point for the inlet and outlet tubing for the nitrogen. The flat bottoms of the end caps were separated using foam insulation to reduce thermal conduction from the outlet side to the inlet side of the enclosure. A small c-clamp was used to keep the end caps facing each other while inflated. Without the clamp, the pressure from the nitrogen gas would push the ends of the enclosure out radially.

Figure 2.16 Vapor containment end caps and closed cell foam

Figure 2.17 End caps with ends of plastic and fiberglass secured

The final dimensions of the full torus used for thermal and deployment laboratory testing are given in Table 2-2.

Table 2-2 Test article dimensions for thermal and deployment testing

Major diameter	185 cm
PVC minor OD	140.9 mm
PVC minor ID	126.mm
Single plastic layer thickness	0.13 mm
MLI total thickness	~ 17 mm (+/- 2 mm)
Fiberglass sleeve thickness	0.6 mm

Chapter 3: Thermal Investigation

3.1 Thermal testing

In order to estimate the thermal performance of the inflatable thermal enclosure during on-orbit operations, laboratory thermal tests were conducted to measure the heat transfer into the system and properties of the thermal insulation. Another goal of the testing was to determine the feasibility of maintaining operational temperatures below the critical temperature of the superconducting material using nitrogen vapor. The performance of the test article was determined from temperature measurements taken at various locations along the circumference of the vapor core and across the thermal insulation layers. The results of the test were used to make predictions for on-orbit performance.

3.1.1 Test setup

The enclosure was placed in the vacuum chamber shown in Figure 3.1 for thermal testing. As previously mentioned, the chamber was custom fabricated for a previous investigation of a toroidal heat pipe [5]. The chamber walls were constructed using 10-inch schedule 80 PVC pipe segments. The top and bottom halves separated in the plane of the major circle of the torus. The flanges and ports were also constructed using PVC material. The port feedthroughs were configured as shown in Figure 3.2. Two ports were dedicated to the thermocouple feedthroughs which passed through five channels per port. The pressure inside the chamber was measured using a cold cathode vacuum transducer made by MKS (P/N: 972B-20134). The nitrogen flow was measured using an Omega flow meter (P/N: FMA 1609A) connected downstream of the outlet using 1/4-inch nylon tubing. Temperature, pressure, mass flow rate, and volumetric flow rate were reported at 1.0153

seconds per sample. The flow meter had a low temperature operating bound of -10 °C so extra tubing was used to allow more heat to warm up the nitrogen before passing through the flow meter. For this reason, the flow meter measurements for temperature and pressure did not match the conditions directly at the outlet of the enclosure.

Figure 3.1 Vacuum chamber used for thermal testing

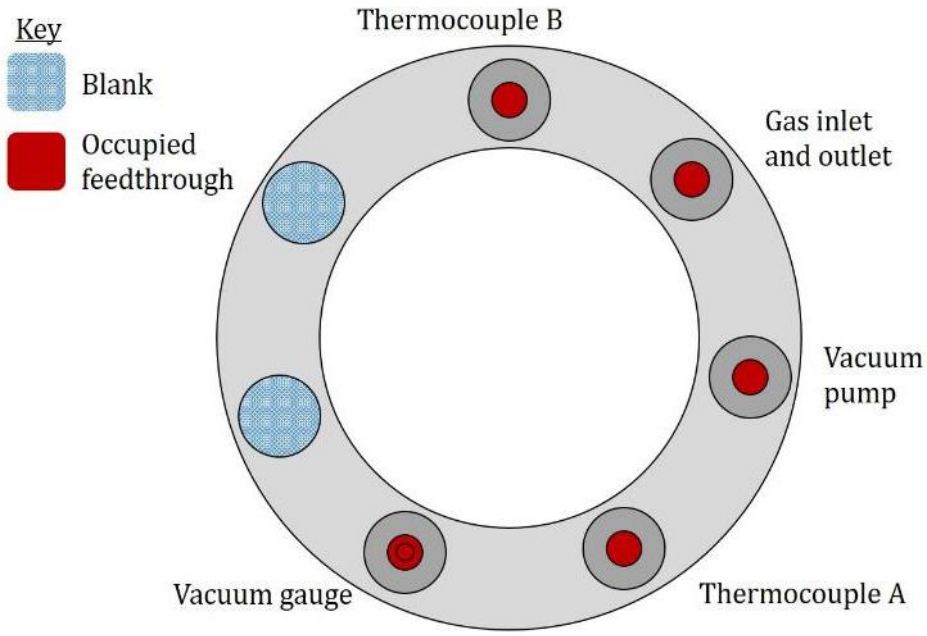

Figure 3.2 Chamber port configuration, view from above

Temperature of the outer plastic surface was measured at four different locations on the enclosure as a representation of the vapor core temperature: near the inlet (x = 0) and outlet (x = L), x = L/2, and x = 3L/4 as shown in Figure 3.4, where L is the circumference length of the torus. Additionally, temperature measurements at three different insulation layers were taken at x = L/2. To reduce the effect of thermal conduction along the thermocouple wire, which would result in erroneous measurements, the thermocouple wire was wrapped around the surface of interest several times, represented by the dashed lines in Figure 3.3. The last thermocouple measured the vacuum chamber wall in the vicinity of the 'Thermocouple B' feedthrough.

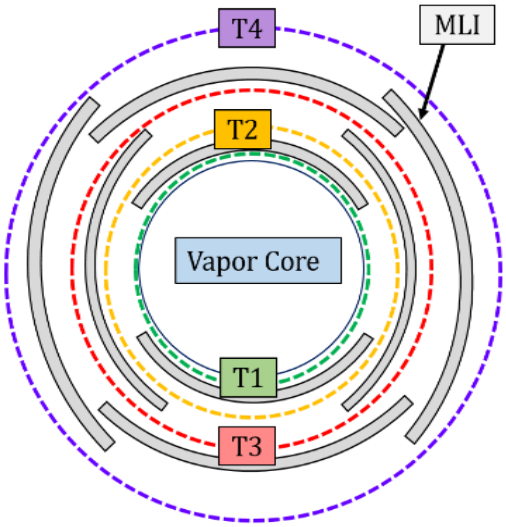

Figure 3.3 Minor diameter cross-section showing thermocouple locations around MLI blanket layers

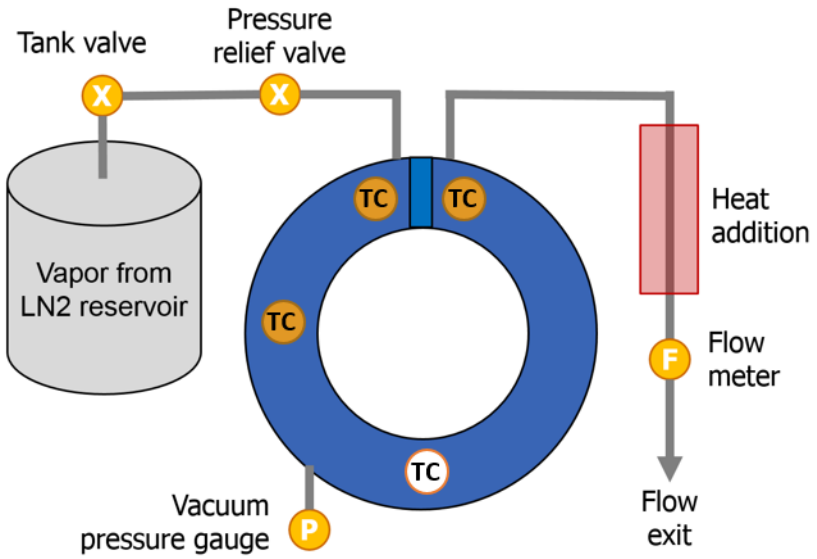

Figure 3.4 Schematic of nitrogen flow path and thermocouple longitudinal locations

To reduce thermal conduction to the chamber walls, 1.5 cm diameter G10 rods were placed underneath each collar to reduce contact between the MLI and the chamber. There was still some contact with the MLI and the inner surface of the chamber as shown in Figure 3.5 that was not quantified.

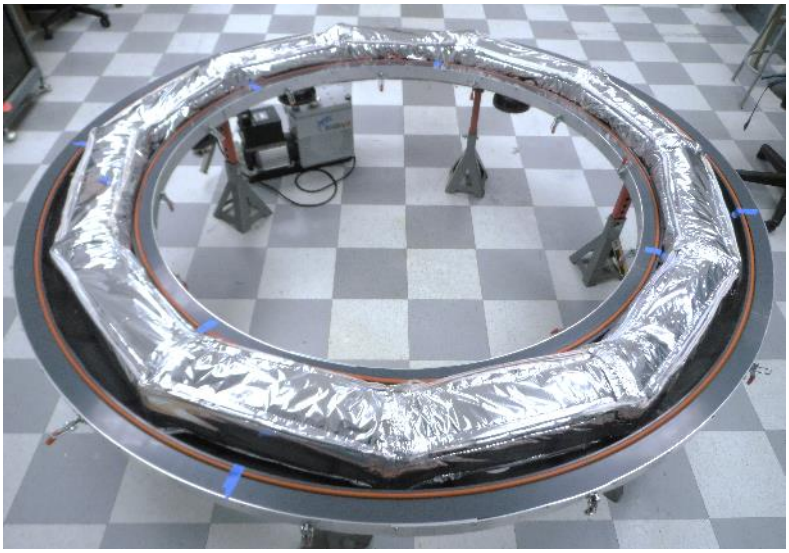

Figure 3.5 Lab-scale thermal enclosure sitting in open vacuum chamber

The temperature measurements were reported using an Omega data logger (P/N: HH309). The data logger could only measure four channels at a time. Each data logger communicated with a separate laptop through an RS-232 communication port. Due to limited resources, only two computers were used for data recording. This meant that one channel at each thermocouple feedthrough port was unused. One of the laptops was simultaneously also reading in data from the flow meter. The vacuum chamber pressure measurements were recorded by hand at irregular intervals.

The chamber vacuum pressure was achieved using a roughing pump. The seams connecting the segments of vacuum chamber PVC and out of plane deformation of the large flange mating surfaces prevented the chamber pressure from reaching below 30 mbar for any of the test runs. For this reason, the turbo pump connected to the system could not

be turned on and instead acted as an intermediate connection between the roughing pump and the chamber port.

The nitrogen vapor used for heat extraction was supplied using a high-pressure liquid nitrogen cylinder. The dewar was pressure limited to 230 psi. The gas line on the dewar was connected to the inlet side of the gas feedthrough port of the chamber using a thermally insulated metal bellow and ¼-inch nylon tubing. It was found that the pressure gauge on gas line of the tank was unable to read the pressure under cold conditions.

3.1.2 Testing procedure

First, the roughing pump was turned on to allow the vacuum chamber to reach a starting pressure of around 70 mbar. The data recording programs had to be started manually. The flow meter does not print out time stamp information so the script that polls the flow meter for data had to be started simultaneously with the start of the thermocouple recording on the other laptop so that the data start time of the flow meter was known. The second set of thermocouple readings was started on the same laptop as the flow meter after a known interval of time.

The liquid nitrogen tank was opened, but not connected to the gas feedthrough for several minutes to allow for a high flow rate while the gas lines wrapped around the inside of the dewar cooled down as liquid nitrogen was drawn out of the central reservoir. Once the tank was outputting nitrogen vapor at temperatures colder than -40 °C, the tank was temporarily closed while the tank hose was connected to the vacuum chamber gas feedthrough. The gas valve on the tank was then opened again and chilled nitrogen vapor

flow inside the enclosure was initiated. Due to the inability to regulate the flow rate or the pressure output of the dewar, the flow conditions and cool down rate of the enclosure varied from test to test.

The procedure for ending of a test was initiated by the closing of the nitrogen tank. The data continued to record while the enclosure slowly warmed up for several of the tests to monitor the heat rate into the system with the flow rate at a minimum. Lastly, the data recording and roughing pumps were shut off to conclude the test.

Data sets collected following this procedure were considered in the analysis phase if the test was completed without catastrophic failure resulting in the roughing pump no longer being able to maintain a chamber pressure below 700 mbar. Failures that discounted tests from further analysis included ruptures to the test article bladder, cracks in the gas feedthroughs, and the formation of cracks in the PVC chamber walls.

3.2 Thermal model

For this analysis, it is assumed that a cryocooler will be used to supply the system with cooling power and a multi-layer insulation blanket will be used to shield the vapor core from incident energy sources.

3.2.1 Model description for laboratory environment

Due to the large pressure fluctuations and weak vacuum conditions during laboratory testing, the modeling of the heat transfer to the chilled nitrogen vapor is modeled

with conduction dominating. To verify the validity of this assumption, heat transfer by convection, radiation, and conduction are compared.

The primary source of gas into the vacuum chamber during testing was determined to be nitrogen leaking out of the bladder through the end cap assembly. The ratio of residual gas thermal conductivity in the chamber over the thermal conductivity at atmospheric conditions is approximated as the ratio of the chamber pressure over standard atmospheric pressure. The conduction through the material layers is calculated as radial heat transfer through concentric cylinders.

For convection, a relationship for the value of the Nusselt number is found for fully developed flow in a circular annular duct [46,47] for heat transfer from the inside surface of the chamber wall to the flow and from the flow to the outside layer of the test article insulation. The thermal conductivity used for the Nusselt relationship is the same value as the purely conductive heat transfer case.

The radiation is approximated using a single source (inside face of chamber wall, subscript 1) and sink (outside surface of MLI, subscript 2) interaction. Equation (2-1) gives the heat transfer to the MLI (q_2) using the blackbody radiation based on the measured surface temperatures, emissivity and surface areas of the source and sink, and the view factor (F_{12}) of radiation from the source to the sink. From reciprocity, it is known that the view factor is equal to the surface area of MLI. The emissivity of the chamber wall is assumed to be 0.9, a typical value for polyvinyl chloride. The emissivity of the MLI was known to be 0.03 from manufacturer specifications of the material.

$$q_2 A_2 = \frac{e_{b1} - e_{b2}}{\frac{1-\varepsilon_1}{\varepsilon_1 A_1} + \frac{1}{A_1 F_{12}} + \frac{1-\varepsilon_2}{\varepsilon_2 A_2}} \tag{3-1}$$

A comparison of heat transfer mechanisms is conducted at every time step using the collected temperature data. An example is shown in Figure 3.6. For all tests, conduction dominates as expected. While convection is shown to be negligible in comparison to conduction, the heat transferred by conduction compared to radiation often differs by less than an order of magnitude. The value of the heat transfer is negative for many data sets due to the temperature of the outer surface of the insulation exceeding the wall temperature.

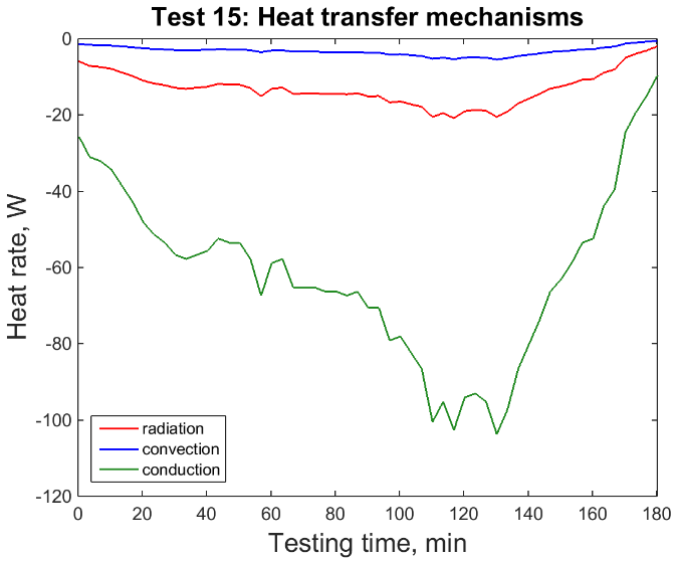

Figure 3.6 Comparison of heat transfer mechanism for Test No. 15

In addition to the radial conduction from the chamber wall through the material layers and into the core of nitrogen vapor, the material layers are considered as three separate regions with respective thermal masses that govern the bulk temperature changes of the material in time. The plastic bladder layer and the residual nitrogen gas in the chamber are assumed to

have no substantial thermal mass. Figure 3.7 shows the designations of the thermal blocks. The vertical axis represents incrementing segments along the path while the radial conduction from the flow to the chamber wall is represented by the horizontal axis. The chilled nitrogen vapor traveling in the core is depicted by the blue regions. The boundaries of material layers of the plastic bladder (green), Material 1 (yellow), Material 2 (red), and Material (purple), as well as the residual nitrogen vapor in the vacuum chamber (grey) are described by the radial distances and temperature. The designation of this product for Material 1 includes the fiberglass restraint layer and polyvinyl collars. Material 2 and Material 3 include the insulation between thermocouple locations 2 and 3, and 3 and 4, respectively. A summary of the subscripts for the radial temperature positions are assigned according to Table 3-1. This correlates with the thermocouple locations depicted in Figure 3.3.

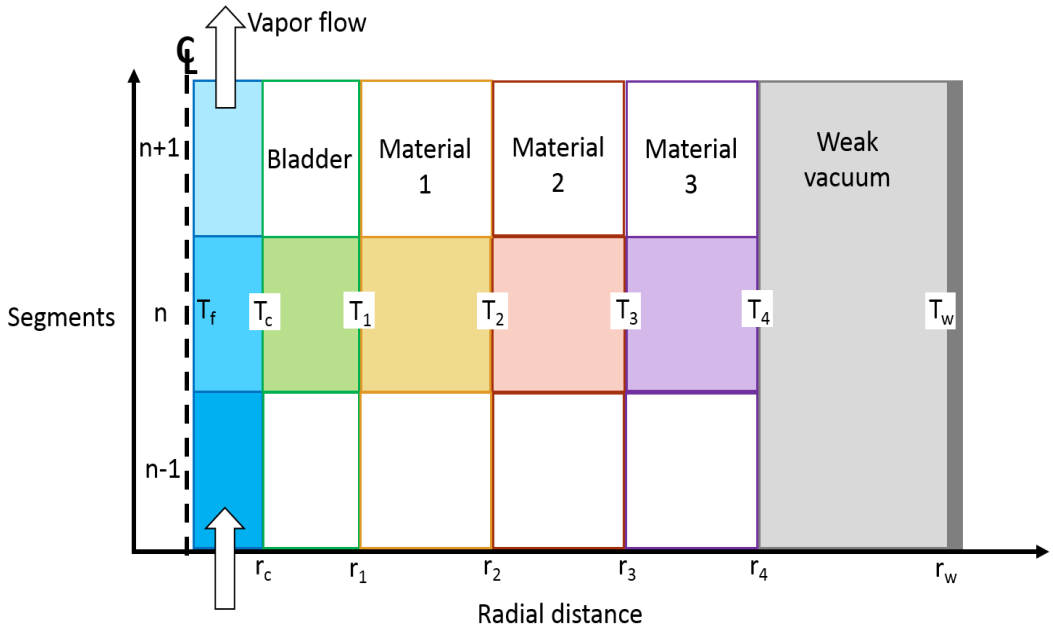

Figure 3.7 Division of material for heat transfer along the flow path (vertical axis) and radial conduction (horizontal axis)

Table 3-1 Designation of material layers

Subscript	Description
w	Chamber wall (and residual gas)
4	Outer surface of insulation
3	Intermittent layer of insulation
2	Intermittent layer of insulation
1	Outside surface of bladder
c	Inside surface of bladder
f	Nitrogen vapor in core

The material blocks and temperature boundaries described by Figure 3.7 can be described using a thermal network as shown in Figure 3.8. The thermal resistances given by Equations (3-2) through (3-7) represent the temperature change between boundary layers due to conduction through the material. The value of the resistances for each material

type is the same for all of the segments. The first subscript of the boundary temperatures is the radial location and the second subscript is the segment number. The temperature of the wall, T_w, is the same for all segments.

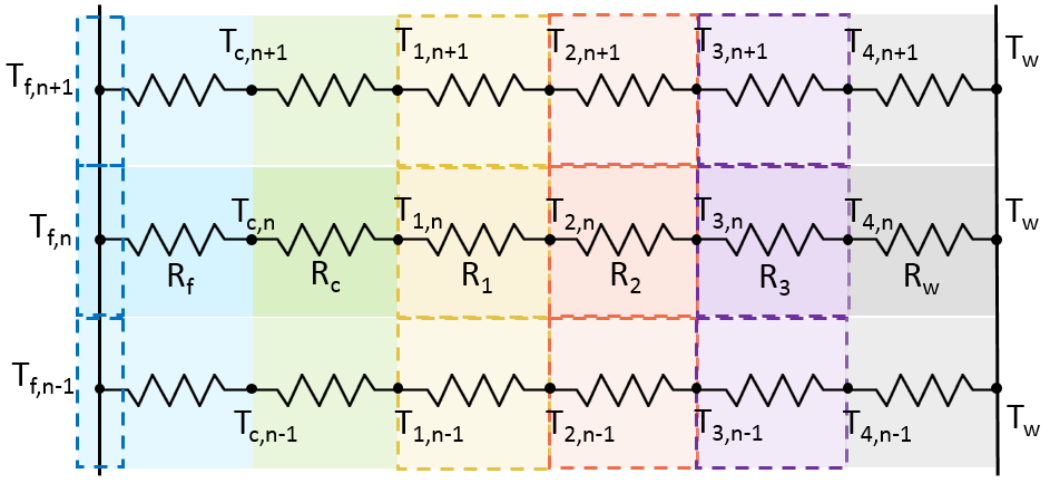

Figure 3.8 Thermal network depicting heat transfer for three adjacent segments and radial material layers

$$R_f = \frac{1}{2\pi r_c (L/N) h} \tag{3-2}$$

$$R_c = \frac{\ln(r_1/r_c)}{2\pi (L/N) k_c} \tag{3-3}$$

$$R_1 = \frac{\ln(r_2/r_1)}{2\pi (L/N) k_1} \tag{3-4}$$

$$R_2 = \frac{\ln(r_3/r_2)}{2\pi (L/N) k_2} \tag{3-5}$$

$$R_3 = \frac{\ln(r_4/r_3)}{2\pi (L/N) k_3} \tag{3-6}$$

$$R_w = \frac{\ln(r_w/r_4)}{2\pi(L/N)k_w} \tag{3-7}$$

The boxes marked with dashed outlines in Figure 3.8 represent material blocks capable of thermal energy storage. Heat entering the flow from the radial direction causes the temperature to rise as it travels downstream. Materials 1, 2, and 3 have mass and thermal capacity that describes the change in temperature of the material layers over time as shown in Figure 3.9a. The difference in heat in and out of the material layer is equal to the thermal energy storage and can be described using the temperatures difference across the adjacent material layers, the thermal resistance of the adjacent materials, and product of the mass and solid specific heat for the material in question as shown by Equation (3-8). The thermal energy storage capacity is lumped as a single variable representing the product of the solid material specific heat and mass of the layer since both properties are unknown.

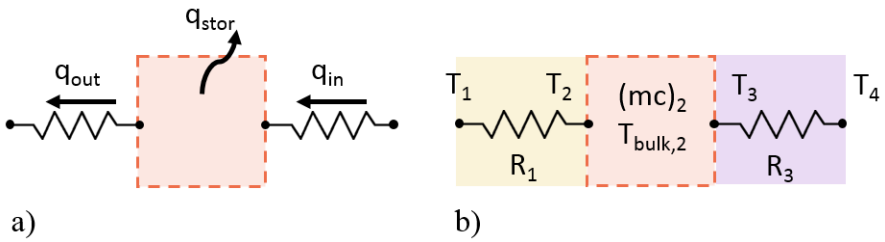

Figure 3.9 Energy balance for material layer for a single segment showing a) direction of heat transfer and storage, b) example using subscripts for Material 2

An example for Material 2 is shown in Figure 3.9b. The heat flow into Material 2 is the heat conducted through Material 3 and is given by (3-9). The heat flow out of Material 2 is the heat conducted through Material 1, similarly given by (3-10). Lastly, the thermal

energy stored in Material 2 is given by (3-11). The bulk temperature of the examined material layer is estimated as the average of the two temperature boundaries. In the case of Material 2, the bulk temperature $T_{bulk,2}$ is the average of T_2 and T_3. The thermal resistance of Material 2 is not considered when looking at the thermal energy balance for Material 2, but does appear in the examination of Materials 1 and 3. When combined, the energy balance for Material becomes Equation (3-13).

$$q_{in} - q_{out} = q_{stor} \tag{3-8}$$

$$q_{in,2} = q_{thru,3} = \frac{T_4 - T_3}{R_3} = \frac{2\pi(L/N)k_3(T_4 - T_3)}{\ln(r_4/r_3)} \tag{3-9}$$

$$q_{out,2} = q_{thru,1} = \frac{T_2 - T_1}{R_1} = \frac{2\pi(L/N)k_1(T_2 - T_1)}{\ln(r_2/r_1)} \tag{3-10}$$

$$q_{stor,2} = (mc)_2 \frac{dT_{bulk,2}}{dt} = (mc)_2 \left[\frac{1}{2}\left(\frac{dT_2}{dt} + \frac{dT_3}{dt}\right)\right] \tag{3-11}$$

The same method can be applied to Material 1 and 3 which yields Equations (3-12) and (3-14).

$$\frac{2\pi(L/N)k_w(T_w - T_4)}{\ln(r_w/r_4)} - \frac{2\pi(L/N)k_2(T_3 - T_2)}{\ln(r_3/r_2)} = (mc)_3 \left[\frac{1}{2}\left(\frac{dT_3}{dt} + \frac{dT_4}{dt}\right)\right] \tag{3-12}$$

$$\frac{2\pi(L/N)k_3(T_4 - T_3)}{\ln(r_4/r_3)} - \frac{2\pi(L/N)k_1(T_2 - T_1)}{\ln(r_2/r_1)} = (mc)_2 \left[\frac{1}{2}\left(\frac{dT_2}{dt} + \frac{dT_3}{dt}\right)\right] \tag{3-13}$$

$$\frac{2\pi(L/N)k_2(T_3 - T_2)}{\ln(r_3/r_2)} - \frac{2\pi(L/N)k_c(T_1 - T_c)}{\ln(r_1/r_c)} = (mc)_1 \left[\frac{1}{2}\left(\frac{dT_1}{dt} + \frac{dT_2}{dt}\right)\right] \tag{3-14}$$

The heat through the bladder equals the heat passed into the flow since the bladder is not considered to have significant thermal mass. The bladder thermal conductivity is

assumed to be 0.33 W/m-K, a typical value for polyethylene. The flow enters the enclosure close to the boiling temperature of nitrogen at 77 K and progressively rises in temperature as heat radially enters the flow. Thus, for a set of temperatures [T_c, T_1, T_2, T_3, T_4, and T_w] at segment *n* the heat transfer into the nitrogen gas is given by

$$\frac{2\pi(L/N)k_c(T_1 - T_c)}{ln(r_1/r_c)} = 2\pi r_c(L/N)h\left(T_c - T_f\right) \tag{3-15}$$

$$mc_{v,N2}\dot{T}_{f,n} - \dot{m}c_{p,N2}\left(T_{f,n+1} - T_{f,n}\right) \tag{3-16}$$

The convection coefficient for the heat transfer from the inner surface of the bladder to the flow is estimated as 0.8 W/m^2-K using the Nusselt number relationship for fully developed, laminar flow [47].

3.2.2 Thermal properties of test article

For each qualified data set, the material properties of the test article are calculated according to the temperature measurements and testing conditions. Equations (3-12), (3-13), and (3-14) are re-arranged so the unknowns are grouped as the thermal conductivities over the thermal mass products: $\frac{k_W}{(mc)_3}$, $\frac{k_2}{(mc)_3}$, $\frac{k_3}{(mc)_2}$, and $\frac{k_1}{(mc)_2}$. At regular intervals across the testing time, the unknowns are found using the temperatures at a particular time and the temperatures at the next time interval. This produces a running result of the material properties calculated at various points in time. This repetitive process of finding the material property ratios at adjacent time intervals is repeated over a time range where the temperature data at all x = L/2 locations is steadily decreasing. The averages of the material ratios for each test across the selected time range are shown in Table 3-2.

Table 3-2 Summary material property ratios and standard deviation, x10^4 (m-s)$^{-1}$

Test No.	$\frac{k_w}{(mc)_3}$	σ	$\frac{k_2}{(mc)_3}$	σ	$\frac{k_3}{(mc)_2}$	σ	$\frac{k_1}{(mc)_2}$	σ
15	10.5	5.7	1.1	1.3	0.1	1.6	0.1	1.1
17	10.6	0.9	2.1	0.5	0.1	2.3	0.2	2.0
18	1.2	1.5	0.0	0.7	0.8	0.5	0.7	0.3
19	1.3	1.8	0.1	0.0	2.6	0.7	0.8	0.1
20	8.1	44.7	1.3	6.0	1.6	4.6	1.7	4.3

A delineation out of the individual properties is then found using the material property ratios and two assumptions about the thermal conductivities of the system. The assumed values of k_w (0.24 W/m-K multiplied by the ratio of the chamber pressure to standard atmosphere) and k_c (0.33 W/m-K) are applied. Looking at the quantity of insulation designated to Materials 1, 2, and 3, and assuming that the solid specific heat is the same, it is assumed that the products of the mass and specific heat for the three layers were related according to the mass of insulation only. Given that there are twice the number of insulation panels designated to Material 3, the thermal mass products are related by

$$(mc)_1 = (mc)_2 = \frac{1}{2}(mc)_3 \tag{3-17}$$

This ignores the contribution due to the restraint layer and cuff pieces. The results for the thermal conductivities and the product of the mass and thermal capacity are summarized in

Table 3-3 along with the average and standard deviation overall of the tests.

Table 3-3 Thermal material properties

	Thermal conductivity (mW/m-K)				Mass*(thermal capacity) (J/K)	
Test	Chamber gas	Mat. 3	Mat. 2	Mat. 1	Mat. 3	Mat. 1 & 2
15	11.5	0.1	1.2	0.2	10.9	5.4
17	10.0	0.1	1.9	0.2	9.5	4.7
18	14.4	5.0	0.5	8.5	122	60.8
19	14.1	14.5	0.6	8.9	112	56.1
20	10.2	1.0	1.6	2.2	12.6	6.3
Average	12.0	4.1	1.2	4.0	53.3	26.7
σ	1.9	5.5	0.6	3.9	52.0	26.0

Taking the material properties in

Table 3-3, the temperature profile at the midway longitudinal location (x = L/2) is recreated using Equations (3-12), (3-13), and (3-14) and the data for only T_1 and T_w. The temperature on the inside of the bladder and the flow temperature are also modeled using Equations (3-15) and (3-16). An example of the recreation is shown in Figure 3.10. The solid lines indicate the data collected while the dashed lines represent the temperature profiles created given the material properties calculated for Test 19 and the T_1 and T_w data.

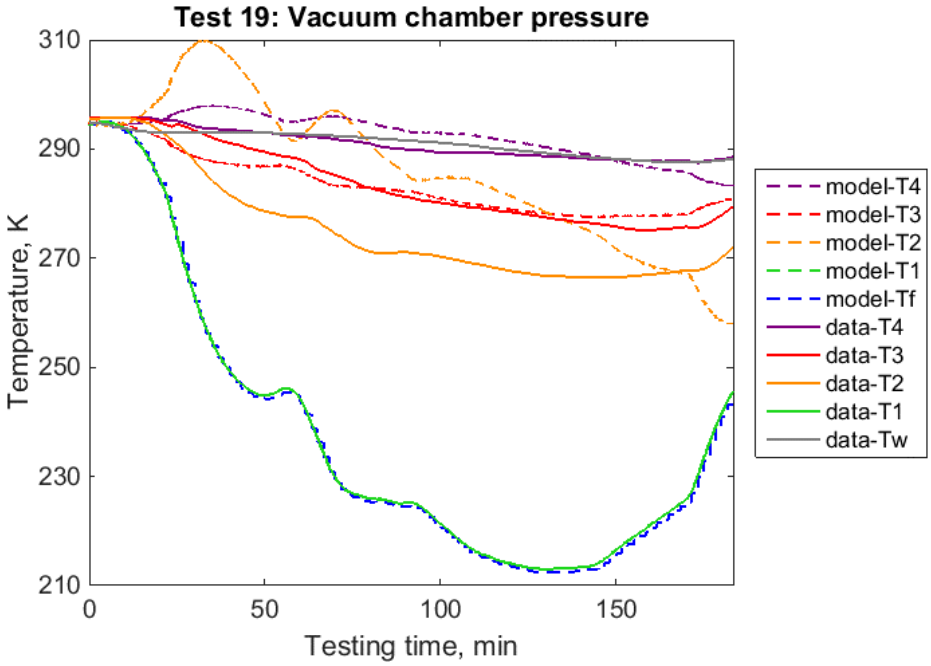

Figure 3.10 Temperature data and recreation of temperature profile for Test No 19 using model

The recreation shows close correlation to the data for the T_3 and T_4. The model predicts T_2 to be closer in value to T_3 than the data for that thermocouple location. This is due to the chamber wall temperature measurement sometimes being very close or lower in value than the temperature of the outer most MLI surface. However, the chamber wall

temperature was measured near the x = 3L/4 location rather than x = L/2 (where T_4 is measured). Due to thermal conduction at the nitrogen feedthrough port, there could be a slight difference in the wall temperature at x = 3L/4 and x = L/2 that would cause result in the true chamber wall temperature at x = L/2 to be higher than the recorded data.

3.2.3 Description of thermal space environment

To approximate the heat rate into the vapor core due to thermal loads in a space environment, it is assumed that the mission under consideration is in low-Earth orbit (LEO) at an altitude of 400 km. The energy inputs to the system are the incident radiation from the Sun, Earth, and the background radiation of space. A worst-case scenario would place the spacecraft orbiting around Earth when the Earth is at the perihelion location, resulting in the highest solar radiation. Assuming the spacecraft is in LEO also agrees with the conditions for a worst-case scenario since the spacecraft will be close to Earth for higher albedo and Earth emitted radiation. By examining the torus-shaped thermal enclosure with the major axis aligned with the radial path from the Sun to Earth as shown in Figure 3.11, the plane of the torus is normal to major incident radiation components which results in higher heat flow into the system than other orientations.

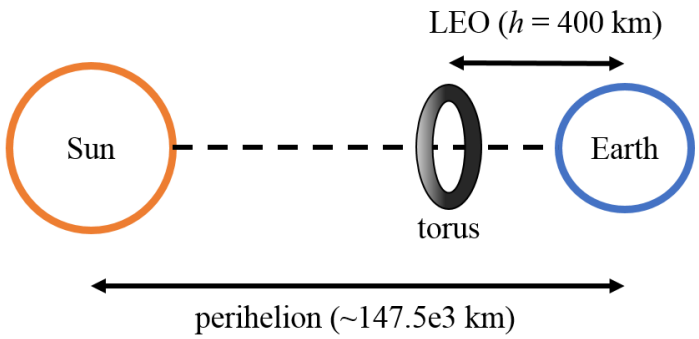

Figure 3.11 Orientation of torus in orbit around Earth and Sun (not to

The solar flux, G_s, at perihelion is approximately 1422 W/m^2. The Earth albedo at winter solstice which accounts for the amount of solar radiation that is reflected off the Earth's surface is 0.35 [48]. While winter solstice and the position of Earth at perihelion are not aligned on the same day, they are close to each other for approximating worst-case incident thermal loads. The albedo heat flux incident on the torus is given by Equation (3-18) where F_{21} is the radiation view factor from the torus enclosure (surface 2) to Earth (surface 1) as indicated in Figure 3.11.

$$q_a = G_s a F_{21} \tag{3-18}$$

Since the torus is far from the surface of the Earth and small in comparison, the torus can be approximated as a 2D projection normal to the incident energy. The view factor of the flat ring with a radial thickness that matches the minor diameter of the torus to Earth (Figure 3.12) is calculated using the summation condition and then the reciprocity relation.

$$F_{12} = F_{1\to2,3} - F_{13}$$
$$F_{21} = F_{12}\frac{A_1}{A_2} \tag{3-19}$$

Recalling that Surface 2 is only the flat disc with Surface 3 (center circle) removed.

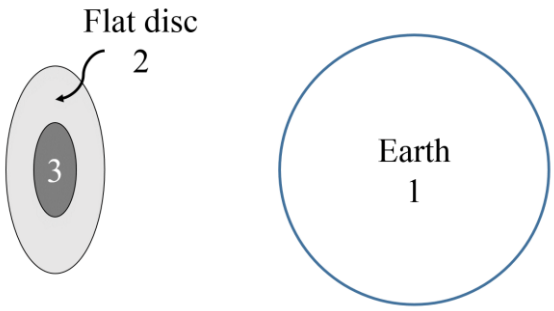

Figure 3.12 View factor numbering designation for flat disc and

The view factors $F_{1\to2,3}$ and F_{13} can be found using a common view factor relation for a flat disc and a sphere [49], and are given by Equations (3-21) and (3-22) where R_c is the major radius and r_h is the minor radius of the torus enclosure (including the thickness of radiation shielding material), R_E is the radius of the Earth, and h is the altitude.

$$F_{1\to2,3} = \frac{1}{2}\left(1 - \frac{1}{\sqrt{1 + \left(\frac{R_c + r_h}{R_E + h}\right)^2}}\right) \tag{3-20}$$

$$F_{1\to 2,3} = \frac{1}{2}\left(1 - \frac{1}{\sqrt{1 + \left(\frac{R_c - r_h}{R_E + h}\right)^2}}\right) \tag{3-21}$$

The areas A_1 and A_2 in Equation (3-19) are the surface of Earth and the 2D projected area of the torus, respectively. The emitted infrared radiation flux from the Earth is given by Equation (3-22) where the average temperature of Earth as 262 K.

$$q_a = \sigma {T_E}^4 F_{21} \tag{3-22}$$

The background space radiation is assumed to behave under blackbody radiation conditions, and, therefore, is given by Equation (3-23).

$$q_b = \sigma {T_b}^4 \tag{3-23}$$

The heat absorbed at the outer surface of the thermal enclosure must either be conducted to the vapor core where heat is extracted using the cooling management system or emitted as radiation into space by the enclosure surface. The heat flowing into the vapor core can be represented using solid conduction and further simplified by treating the concentric tori as concentric cylinders of length L.

$$L = 2\pi R_c \tag{3-24}$$

$$Q_{cond} = 2\pi k L \frac{T_h - T_c}{\ln(r_h/r_c)} \tag{3-25}$$

$$Q_{emit} = \sigma \varepsilon {T_h}^4 \tag{3-26}$$

The conduction depends on the outer enclosure wall radius and the inner vapor core radius, as well as the surface temperatures at those radii locations. Similarly, the heat leaving the surface as emitted radiation depends on the surface temperature of the enclosure, and also depends on the surface properties of the outer enclosure. To solve the governing equations, a model connecting the relationship between all of the contributing heat sources and sinks must be established.

3.2.4 Predicted performance in space environment

The heat loading on the vapor inside the torus can be determined using an energy balance at the outer surface of the torus and conduction from the surface to the vapor core. Using the material property values found in the laboratory testing, the surface energy balance at the outer surface differs between the Sun-facing and Earth-facing sides of the HTS coil enclosure.

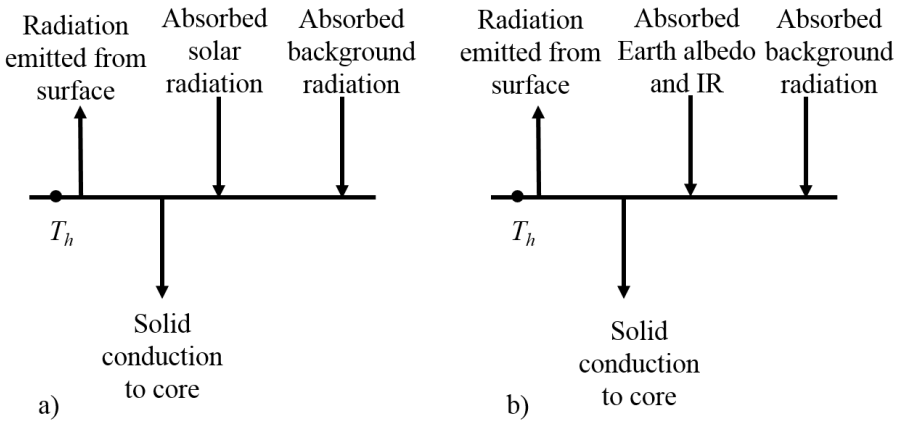

Figure 3.13 Energy balance at outer surface of thermal enclosure where a) is the Sun-facing surface and b) is the Earth-facing surface

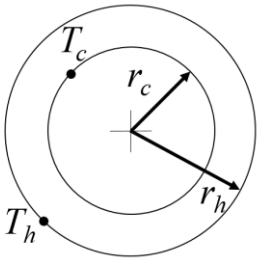

Figure 3.14 Cross-section of enclosure minor diameter

The energy balance at the surface for the two cases shown in Figure 3.13 for temperatures and enclosure dimension shown in Figure 3.14 is given by

$$0 = \sigma\varepsilon {T_h}^4 A_h + 2\pi kL \frac{T_h - T_c}{\ln(r_h/r_c)} - \alpha A_h G_s - \alpha A_h q_b \tag{3-27}$$

$$0 = \sigma\varepsilon {T_h}^4 A_h + 2\pi kL \frac{T_h - T_c}{\ln(r_h/r_c)} - \alpha A_h (q_a + q_E) - \alpha A_h q_b \tag{3-28}$$

The equations can be separately solved to find the outer surface temperature of the torus and the heat conducted to the core is given by the second term. This assumes the heat loading for each equation is symmetrical about the plane of the torus and the temperature of the vapor core is fixed at T_c. The total heat flow into the vapor core is found by taking half of the value for the heat flow contribution from each equation and adding them together. Equation (3-27) accounts for the heat flow from the Sun-facing side of the torus while Equation (3-28) accounts for the Earth facing side.

Table 3-4 Summary of thermal loading variables

Quantity	Symbol	Value
Stefan-Boltzmann constant	σ	5.67e-8 W(m^2-K^4)
Major radius of HTS coil	R_c	92.5 cm
Minor radius of enclosure	r_h	8.3 cm

Surface area of enclosure	A_h	1.03 m^2
Vapor core radius	r_c	6.3 cm
Radius of Earth	R_E	6378 km
Torus altitude	h	400 km
Solar flux	G_s	1422 W/m^2
Earth albedo [48]	a	0.35
Background space temperature	T_b	4 K
MLI effective thermal conductivity	k	1.6 mW/(m-K)
MLI absorptivity [20]	α	0.10
MLI emissivity [20]	ε	0.85
Vapor core temperature	T_c	77 K

Using the material properties and dimensions of the test article, the thermal load when exposed to the space environment is calculated. First, the initial temperature of the structure before cooling begins is found by performing an energy balance at the surface on the outer surface of the insulation. The emissivity (and assumed absorptivity) of the aluminized Mylar is 0.03, resulting in a temperature of 398 K on the Sun-facing side of the torus. This result is compared to adding FEP Teflon with silver backing as the outermost layer of the structure, a material indicated as a common outer layer for MLI blankets by the "NASA Multilayer Insulation Material Guidelines" [20]. The guidelines state that the outermost material helps protect the inner layers from "shedding, flaking, and other forms of particulate generation" on the aluminized surface of the shield layers due to exposure to the harsh space environment [20]. The emissivity and absorptivity were specified as 0.85 and 0.10, respectively. This much higher emissivity despite slightly higher absorptivity results in the sun-facing initial temperature of 233 K.

Assuming the same thermal conductivities and dimensions, the steady-state temperature profile is found comparing Mylar and FEP Teflon as the outer surfaces. In steady-state, the core temperature near the inlet would be 77 K and the changes in temperature for a particular material layer would not change in time. Table 3-5 shows a comparison of the two conditions. Figure 3.15a shows how the thermal load into the vapor core of the enclosure changes with MLI thermal conductivity. It also compares using the aluminized Mylar from the MLI as the outer surface material of the enclosure to using FEP Teflon with a silver backing as the outer surface material, but keeping MLI blankets as the interior insulation. The blue and red markers indicate the average and minimum values of the thermal conductivity found for the test article. Similarly, Figure 3.15b shows the thermal load into the vapor core as the total thermal resistance of all the material layers changes due to changes in the insulation properties. The comparison between the outer surface material and the markers for the test article performance are also indicated. Based on these results, FEP Teflon with a silver backing is desirable over aluminized Mylar as the outer surface material.

Table 3-5 Outer surface temperature under conduction-only conditions

		Aluminized Mylar	FEP Teflon with silver backing
Initial temperature	Earth-facing side	240 K	141 K
	Sun-facing side	398 K	233 K
Final temperature	Earth-facing side	117 K	126 K
	Sun-facing side	298 K	225 K

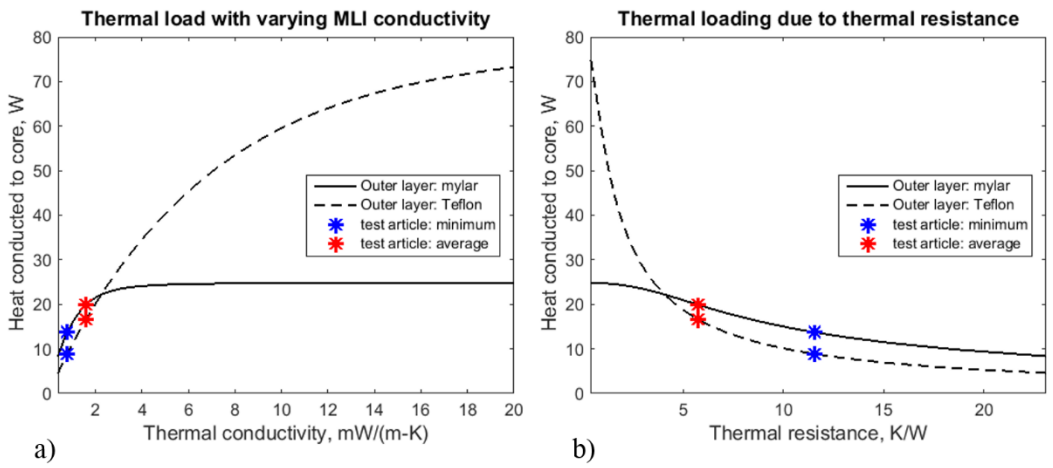

Figure 3.15 Comparing outer surface material for changing values of a) insulation conductivity b) total thermal resistance

A typical transition temperature for high-temperature superconductors (similar to the material that SuperPower used to manufacture the thin profile tape) is 130 K. This means the desired outlet temperature needs to be below the critical temperature. The temperature downstream of the inlet section is found using Equation (3-16). For a fixed set of material values and convection coefficient, the longitudinal flow temperature profile is varied by examining different mass flow rates. The average mass flow rate during testing is limited to approximately 1.0e-3 kg/s (50 LPM at standard conditions). A comparison between a slightly higher volumetric flow rate and a flow rate of an order of magnitude higher is shown in Figure 3.16. The bright red line at the bottom of the grouping for each graph is the trend of the flow temperature over time at the segment closest to the inlet. Each subsequent segment downstream is shown in a slightly darker color and shows the trend of settling to a successively high temperature once a steady state is reached.

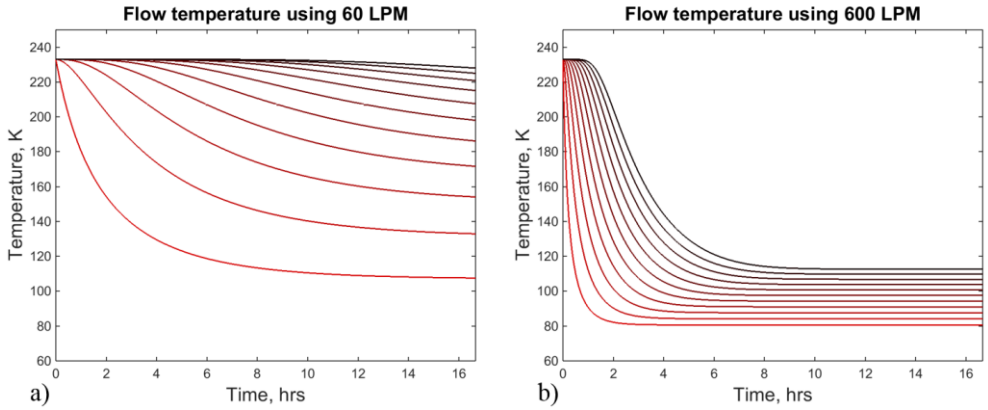

Figure 3.16 Flow temperature at progressively downstream segments at a flow rate of a) 60 LPM and b) 600 LPM

At the lower flow rate (Figure 3.16a), the vapor core temperature rapidly increases for downstream segments. At near steady state, the inlet side is below the 130 K threshold, but all remaining segments are not. In contrast, the higher flow rate not only achieves a lower steady state temperature for the first segment, but all downstream segments are able to reach a temperature below the threshold.

In examining possible off-nominal testing conditions, two cases look at the effect of alternating the flow direction to change the warm end of the flow path to the cold end (Figure 3.17). The first case (a) uses a constant interval of 3.5 hours to switch flow directions. The second case (b) waited 8 hours for a steady state to be reached before alternating the flow direction at an interval of 2 hours.

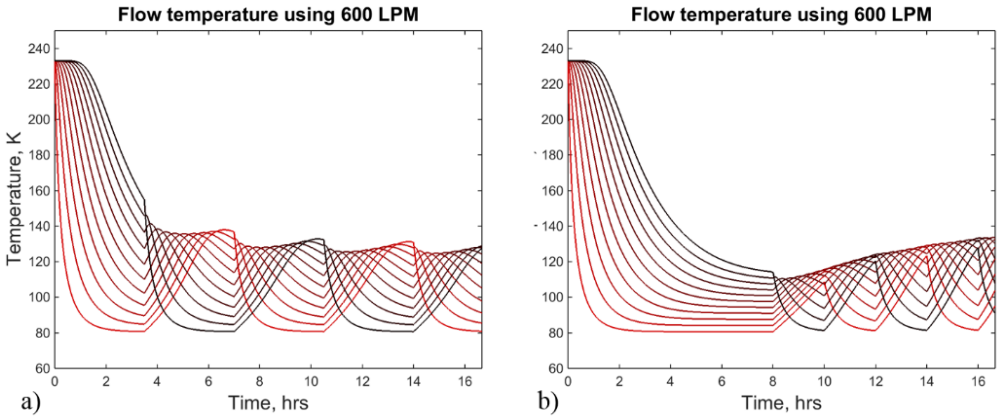

Figure 3.17 Flow temperature at all segment locations with direction of flow alternating a) every 3.5 hours, b) 2 hours after the first 8 hours

For case (a), alternating the flow stops pulling down the overall flow temperature for all the segments after two intervals. The temperature difference between the cold end and warm end increases compared to the same flow rate with no switching. For case (b), alternating the flow causes the temperature to increase for segments downstream of the cold end, slowly bringing up the temperature distribution. In conclusion, the switching of the warm and cold ends fails to bring down the overall flow temperature distribution along all the segments and would not be a useful technique in situations where the enclosure may be operating close to the HTS critical temperature.

3.3 Thermal investigation conclusions

An enclosure capable of housing a 1.85-meter coil was fabricated using off-the-shelf materials. Despite a limited number of thermocouple locations and varying test conditions (such as vacuum pressure and flow rate), the material properties of the test

article were found by modeling the heat transfer through the material layers as dominantly conductive. Given the material properties, the performance of the test article was examined in an expected space environment.

The results of this thermal investigation contribute to the examination of a point design case detailed in Section 5.1.

Chapter 4: Deployment Investigation

4.1 Deployment of a straight thermal enclosure

Axial force testing was conducted on a single section of the enclosure to measure the static deployment force. The section is composed of one spring identical to the springs that make up the internal structure of the full toroidal test article. The spring was custom manufactured by Murphy & Read Spring Mfg. with the following specifications listed in Table 4-1.

Table 4-1 Summary of spring specifications

Wire material	Carbon steel (music wire)
Wire diameter	2.997 mm (0.1180 in.)
Outer coil diameter	10.46 cm (4.120 in.)
Length	75.52 cm (2.478 ft.)
Total coil turns	20
Active coil turns	18
Mass (Weight)	0.3542 kg (0.780961 lbs.)
Spring constant	0.35 N/cm (0.2 lbs./in.)

The material layers added over the spring also matched the materials used to fabricate the full toroidal lab prototype.

4.1.1 Test setup

The axial force was measured using a Tinius Olsen H25KT Universal Testing Machine. The force was measured by a load cell that moved at a constant rate during the course of the test. The test article was fixed to 1-inch thick aluminum base plates at the ends using L-brackets attached to the outer surface of the PVC cuffs. The plates were

attached to the testing machine base and load cell using large machine screws. The testing configuration is shown in Figure 4.1.

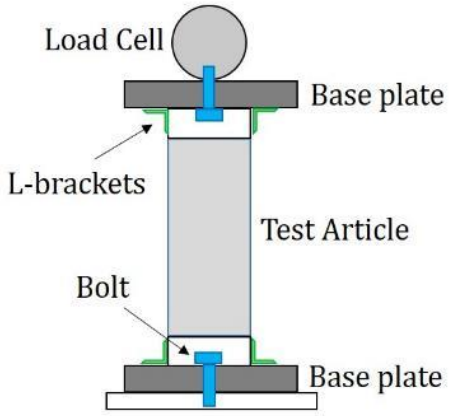

Figure 4.1 Axial spring force testing configuration

Three rates of motion were observed: 100 mm/minute, 150 mm/minute, and 200 mm/minute. The initial position of the load cell held the assembly close to the deployed, zero-force state before compressing the spring to the minimum allowable length. The position of maximum compression was held for 10 seconds before the load cell retracted and measured the deployment force while moving at the same rate as the compression.

4.1.2 Results from testing and discussion

The test results are shown in Figure 4.2. The force is negative when the load cell moved beyond the zero-force point of the spring deformation. The stair-stepping of the data is due to the resolution of the universal testing machine.

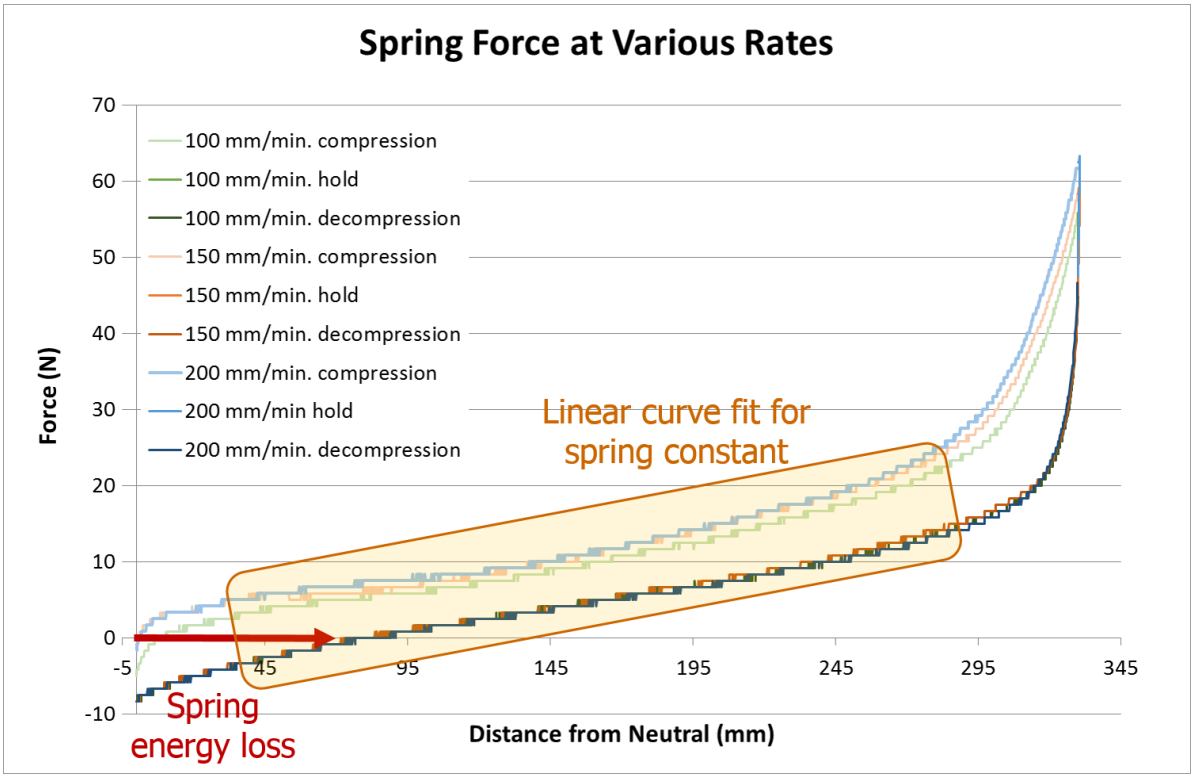

Figure 4.2 Enclosure deployment force at different rates of axial motion

The compression distance is relative to the initial position of the spring in a near fully deployed state with the force close to zero. Positive compressive motion correlates to the load cell moving downward at a constant speed as shown in Figure 4.3, reducing the axial distance between the base plates. The difference in the zero force crossing compared to compression distance between the compression and deployment motion is due to an imperfect recovery of the spring potential energy.

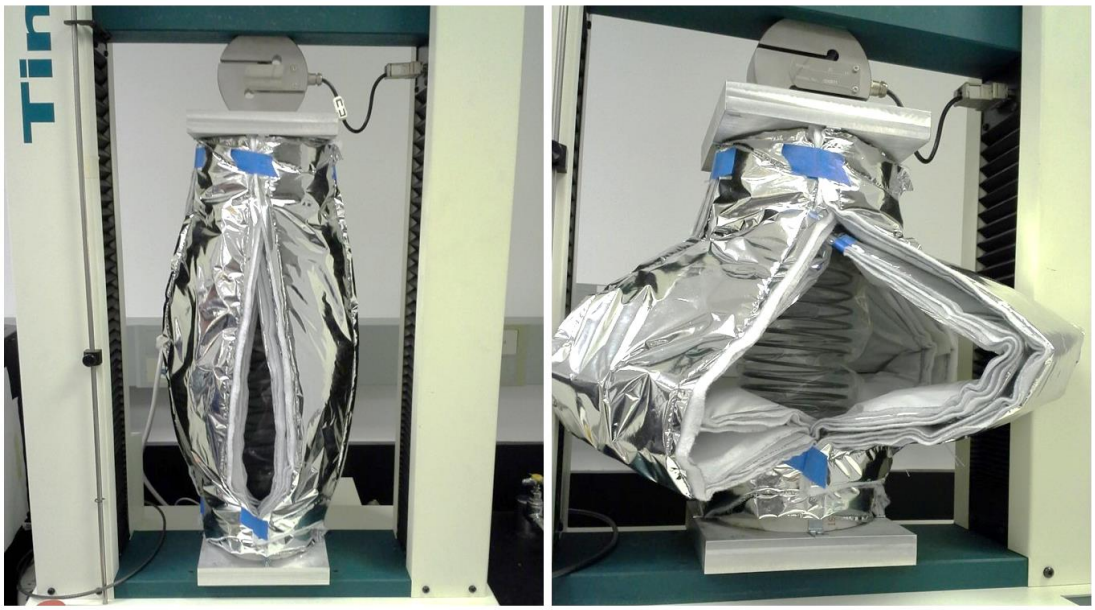

a) b)

Figure 4.3 Deployment force test a) at the start of compression, b) near full compression

The data from a compression distance of 38 mm to 293 mm is selected for a linear fit due to the region of active turns for the spring. The non-linear behavior outside of the lower bound is due to the spring not having uniform turns at the ends. The non-linear behavior outside of the upper bound is due to the spring reaching the fully compressed state such that there was no more space between turns of the spring. An effective spring constant is used to describe the linear force contribution on the assembly. The spring constant is extracted using a linear fit. The calculated effective spring constant for each compression rate is given in Table 4-2, and the average spring constant is 0.662 N/cm when compressing the spring and 0.780 N/cm during expansion. This value is approximately double the manufactured specification of 0.35 N/cm listed in Table 4-1. The difference can possibly

be due to the resistance of the plastic and thermal blankets folding during compression and expansion of the test article.

Table 4-2 Summary of deployment force for straight enclosure segment

	Effective spring constant (N/cm, lbs./in.)	
Rate of motion (mm/min.)	Compression	Expansion
100	0.660 (0.377)	0.761 (0.435)
150	0.678 (0.387)	0.791 (0.451)
200	0.648 (0.370)	0.787 (0.450)
Average	**0.662 (0.378)**	**0.780 (0.445)**

4.2 Deployment of lab-scale toroidal thermal enclosure

The static testing of the single spring segment determined the axial deployment force, represented by an effective spring constant. However, the dynamic motion of a torus like the full test article is much more complex. For this reason, deployment tests using the same test article from the thermal testing were conducted to measure the motion of the structure from a representative stowed configuration to the neutral, fully-deployed size. The results are compared to the static testing and used to draw predictions for an enclosure of the same dimensions deployed in space.

4.2.1 Test setup for lab-scale deployment

The deployment motion of the test article was measured using a motion capture system operated by the Collective Dynamics and Control Laboratory under Dr. Derek Paley at the University of Maryland. Infrared cameras were mounted along the top perimeter of a large frame that defined the allowable testing space. The cameras detect the

reflected infrared light of a marker and record the position of the marker in the testing space.

For optimal visibility by the cameras, the test article was positioned close to the floor while still allowing clearance for the insulation blankets to bow outward when pulled into its stowed configuration. The test article was suspended above the floor using ropes threaded through eyebolts attached to each collar. This allowed for less restricted motion along the plane parallel to the floor by replacing drag on the floor as the test article deploys with tension in the ropes. To minimize translational motion and vibration the ropes were attached to a disc held up by a pole through the major axis of the enclosure as shown in Figure 4.4.

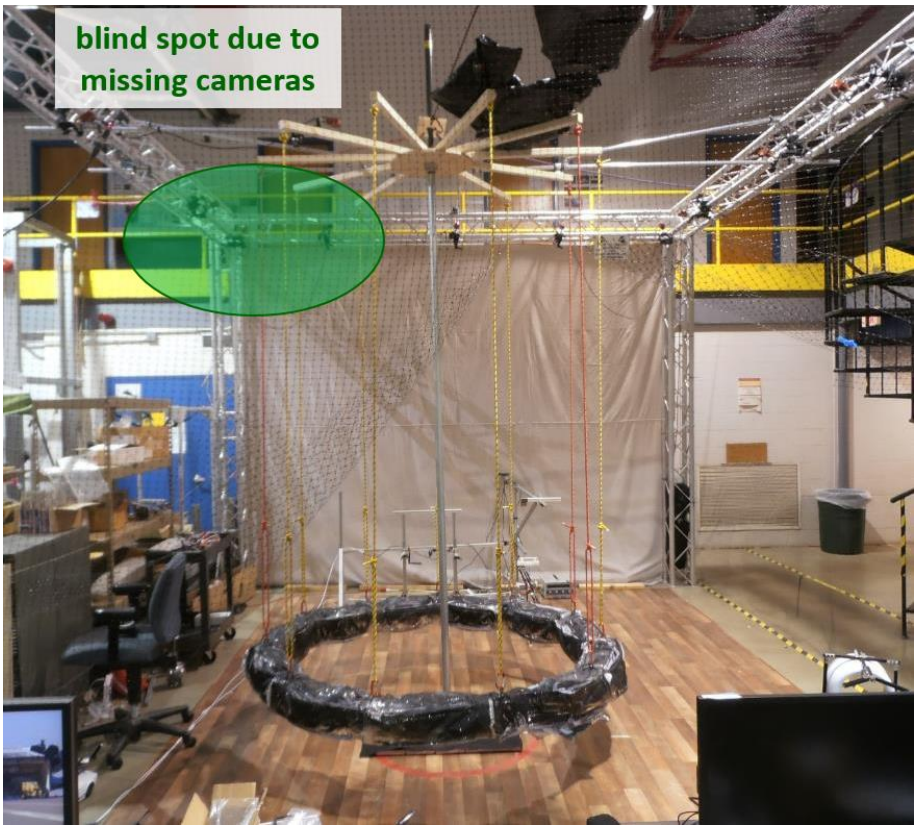

Figure 4.4 Test article suspended from the top of a pole through its major axis inside the motion capture facility

The deployment motion tests were conducted after the laboratory thermal testing concluded. To reduce noise and erroneous reflections, the outside surface of the reflective shield layer was painted a matte black. For the markers, small pieces of highly reflective tape were placed on the top-outside corner of each collar. Due to unavoidable equipment allocation during the available testing window, the absence of several cameras created a significant blind spot (indicated by the green shaded region) in the testing volume. Markers facing that corner of the camera perimeter were often lost during the deployment motion.

To bring the enclosure into a stowed configuration, a thin rope threaded through the eyebolts on the test article was used to compress the springs and pull the collars close together as shown in Figure 4.5. Once the test article was pulled into the stowed configuration, the data acquisition started and the rope holding the collars together was released.

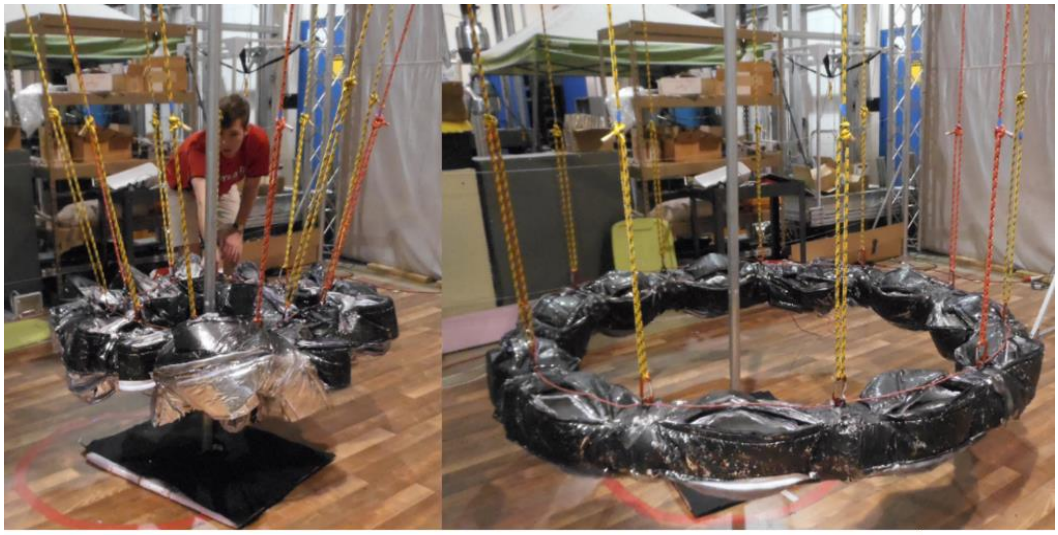

a) b)

Figure 4.5 a) Test article prior to deployment and b) after deployment

4.2.2 Tracking of deployment motion

The data was recorded by the same software that also controlled the system of infrared cameras. For each sample time, a frame of data was collected as a set of coordinates of each marker (real or erroneous). The coordinate system was configured so that the x-y plane lay on the floor of the facility and the positive z axis pointed up towards the ceiling. The origin was located on the center of the floor. It should be noted that the

major axis of the enclosure was not located at the coordinate origin and varied between testing sessions. As markers moved position from frame to frame, in which the order of the marker coordinates recorded was not necessarily the same across frames. For this reason, an acceptance path of each collar is defined using a parametric fit by selecting markers that obviously belonged to the same collar as it moved in time as shown in Figure 4.6. Some tests were conducted with clouds of markers at each collar, but having a single marker at each collar is easier to track even though the marker may be lost for a few frames during the deployment motion.

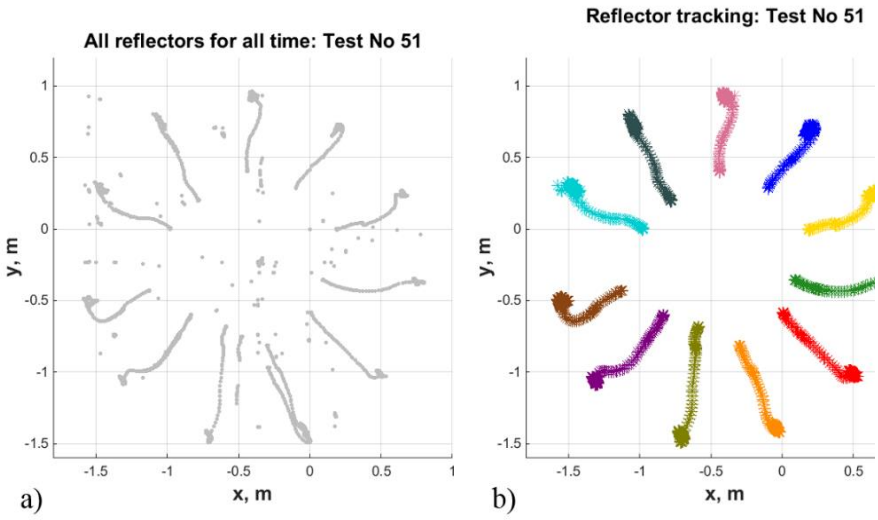

Figure 4.6 Top view of a) all recorded markers for all time, b) marker correlation to produce tracked collar motion over time

After correlating the marker positions for all time frames to particular collars, the relative distances between collars and the collar velocity and acceleration are found. This information is used to find the dynamic structural properties of the test article.

4.3 Deployment model

Similar to the thermal investigation, a model is used to find mechanical properties of the test article given the data collected from the deployment testing. Once the mechanical properties are found, the deployment motion is recreated using the test initial conditions. The model is also used to predict the deployment motion of the test article in the space environment, absent of the rope tension and gravity that acted on the structure during laboratory testing.

4.3.1 Model of laboratory deployment

The test article is modeled with the total mass of the structure evenly divided into point masses located at the center of the collars. In addition to the rope tension and weight acting on each collar, the deployment forces and connections between point masses are represented as ideal spring and damper elements. The spring and damper elements are connected in parallel. The model uses the data collected from the deployment demonstrations to determine the values of the spring constant and damping coefficient between each of the point masses.

Based on observations of the deployment motion, the point masses are assumed to move in straight, radial paths in the plane of the enclosure with the angle between each path (γ) to be equal and constant over time. However, at any given time step, the radial position (r_n) of the point masses can vary as shown in Figure 4.7. Looking at a general point mass (m_n) in time, the separation distance to the neighboring point masses are d_n for the span connecting to the n+1 mass and $d_{n\text{-}1}$ for the span connecting to the n-1 mass as

depicted in Figure 4.8. Taking a reference line perpendicular to the radial path for the point mass, the angles created between that reference line and the neighboring point masses are $\theta_{n,1}$ and $\theta_{n,2}$. The distances and angles defining the relative position of the point masses are allowed to change with time. The point masses m_1 and m_{11} neighbor each other so when n = 1, n-1 = 11 and when n = 11, n+1 = 1.

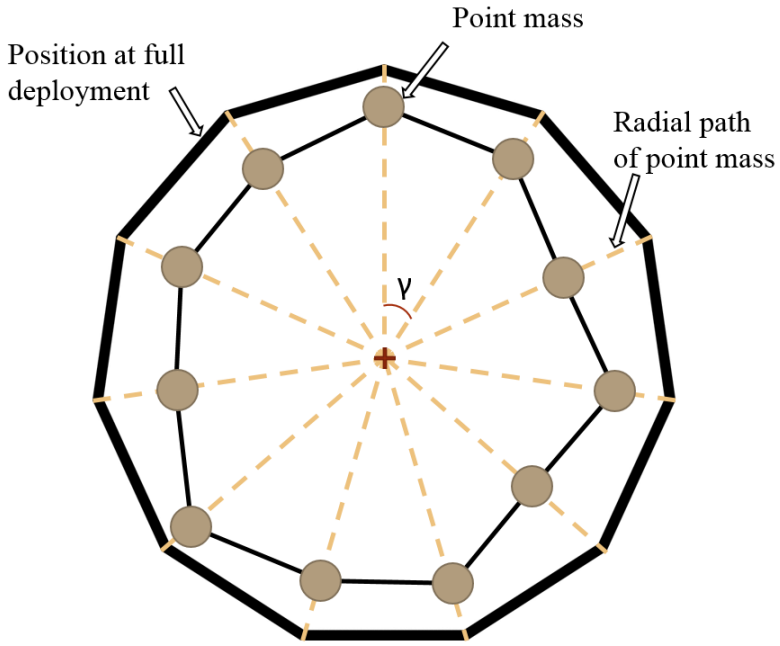

Figure 4.7 Point masses at example time step during deployment

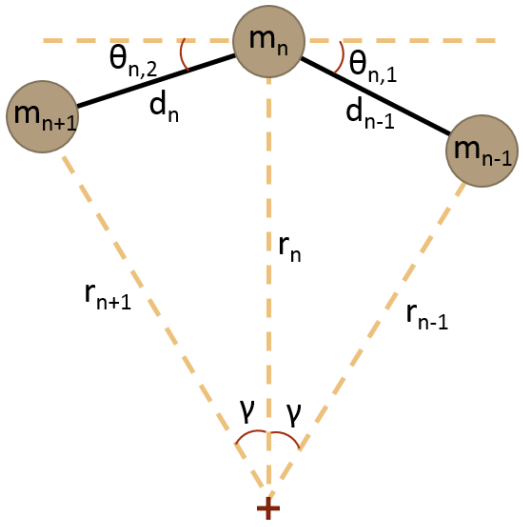

Figure 4.8 Naming convention and dimensions
for dynamic deployment model

For each point mass, there are two spring forces and two damper forces due to the connections to the neighboring point masses. Additionally, the tension (*T*) in the rope acts on the collar at angle φ from the positive z-direction with the force from gravity acting in the negative z-direction as shown in Figure 4.9b. In the free-body diagrams shown in Figure 4.9a, the x-y plane lies on the plane of the test article where the y-direction aligns with the radial path of the point mass under consideration and the x-direction aligns with the reference line perpendicular to the path. This means the direction of x and y changes for each mass relative to the absolute coordinate system of data collected in the test space. The angles shown in the free-body diagrams represent the positive sign convention.

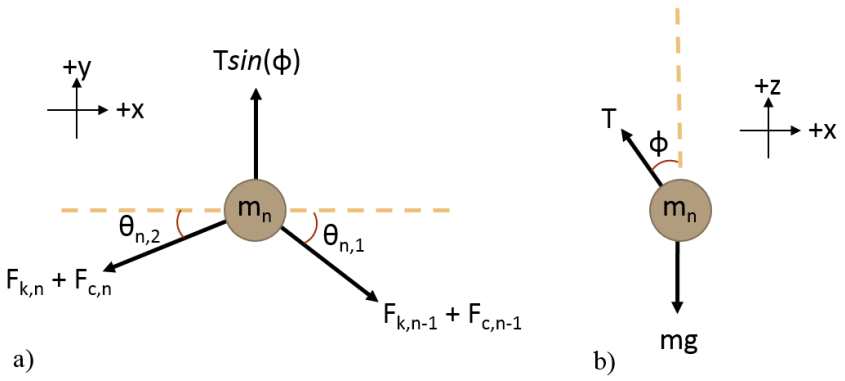

Figure 4.9 Free-body diagram of point mass a) top view, b) side view

Using the free-body diagrams, each point mass is described using Newton's second law of motion, where the radial acceleration is the second rate of change of the radial position y_n.

$$\Sigma F_y = m_n \ddot{y}_n = T_n \sin \varphi_n - k_n(d_n - d_o) - k_{n-1}(d_{n-1} - d_o) \cos \theta_{n,1} \qquad (4\text{-}1)$$
$$- c_n \frac{d(d_n - d_o)}{dt} \cos \theta_{n,2} - c_{n-1} \frac{d(d_{n-1} - d_o)}{dt} \cos \theta_{n,1}$$

The spring connecting m_n to m_{n+1} is assigned a spring constant k_n with the force dictated by d_n relative to the neutral force length of the spring. Similarly, the spring connecting m_n to m_{n-1} is associated with d_{n-1} and a spring constant value of k_{n-1}. The damping force directed toward m_{n+1} is dictated by the change in d_n over time and described using the damping coefficient c_n. Likewise, the damping force toward m_{n-1} is described using d_{n-1} and a damping coefficient c_{n-1}. Since the point masses are assumed to be moving along the radial paths from the center, acceleration in the x-direction depicted in the free-body diagrams is zero and the motion is described by Equation (4-1). Even though a subscript is used to

clarify the point masses under consideration, recalling that the values of the point masses are equal.

4.3.2 Mechanical properties of the test article

The deployment data collected is converted to radial position, speed, and acceleration data for each point mass. Due to some erroneous marker locations still persistent in the filtered position data, the raw calculation of the change in position over time occasionally produces non-physical spikes. To reduce the impact of these spikes, the speed is smoothed and the acceleration is calculated based on the change in speed over time using a right Riemann sum. Figure 4.10 shows an example of the radial position of the point masses over the duration of a test while Figure 4.11 shows the resultant speed and acceleration after the smoothing is applied for all point masses over the course of the testing time. The zero-time marks the start of data recording. The bulk deployment motion is apparent around the time range of 1.5 to 3 seconds. The angle φ_n is found using the radial position and the rope length from the support to the eyebolt. The tension is then found using the relationship between φ_n and the direction of the gravity force.

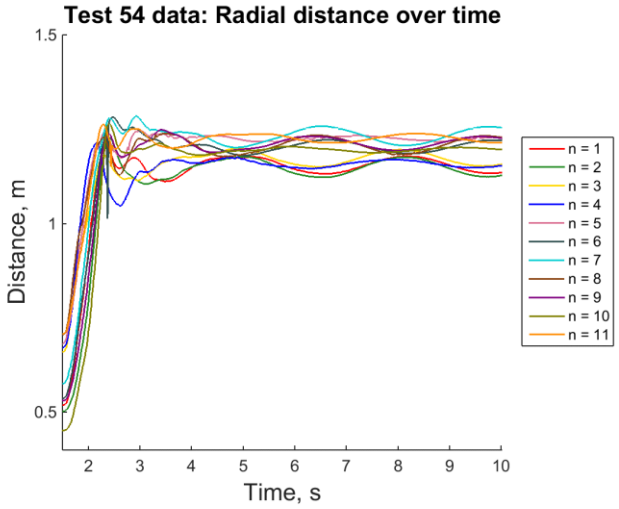

Figure 4.10 Radial position of point masses for Test No. 54

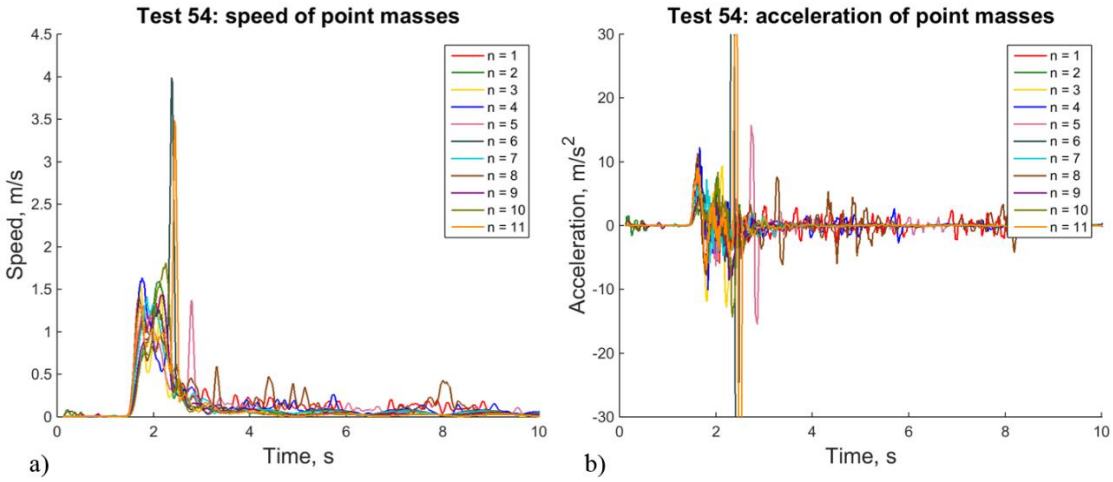

Figure 4.11 Speed after smoothing and resultant acceleration of point masses using data from Test No. 54

For each time step, a set of eleven equations of motion, one for each point mass, is created. Since the motion is known, the spring constants and damping coefficients are assumed to be constant for the time window of interest and described using a system of

linear equations. A large matrix is created from the set of equations of motion over multiple time steps. The height of the matrix is the number of time steps multiplied by the number of point masses. The width of the matrix is the number of unknowns, which is equal to twice the number of point masses (*k* and *c* for each connection). The coefficient matrix is populated with the distance and speed values while the solution vector is populated with the acceleration. The solution yields a least-squared solution for all of the spring constants and damping coefficients. The values found using the entire testing time are compared to values found at specific time windows. One time window of interest is the period of apparent bulk deployment motion. Additionally, a progression of ten time windows, each spanning ten time steps, is also examined to determine if the mechanical properties change depending on the stage of deployment.

For each test, the property values at each window (of ten time steps) are averaged over the ten windows that span the period of bulk motion and across all point masses. The results are listed in Table 4-3. Similar to the thermal material properties, the dynamic motion properties have a standard deviation close to the averages for an individual test. However, the standard deviation of the average across all tests is several factors smaller than the averages themselves. This result is not entirely surprising since the model assumes the springs and dampers are applying forces along the direction of the line that connects the point masses to each other. However, Figure 4.5a shows that pulling the collars close together resulted in some bending in the radial direction despite attempts to axially compress each segment one-by-one. The bending out of axial alignment of the segments is

irregular between collars and also between tests. This variation in the compressed configuration may explain the wide range of mechanical property values. Interestingly, the average value of the spring constant, 32.6 N/m, is close to the manufacturer specifications of the spring along (35 N/m). Recall that the static force testing (Section 4.1.2) of the enclosure assembly resulted in an average spring constant of 78 N/m during expansion.

Table 4-3 Summary of dynamic motion properties

Test No.	Spring constant (N/m)	σ (N/m)	Damping coefficient (N-s/m)	σ (N-s/m)
49	27.3	29.7	6.5	7.4
51	34.4	39.3	6.6	6.7
52	39.8	45.8	8.8	9.1
53	36.9	40.9	11.7	16.5
54	23.4	23.0	8.1	10.3
55	33.8	34.2	8.8	10.4
Average	**32.6**	**5.6**	**8.4**	**1.8**

Given the property values and initial conditions for Test No. 54, recreations of the deployment are created in Figure 4.12. Surprisingly, the values for k_1 (6.9 N/m) and c_1 (14 N-s/m) for the first time window recreate the radial distance profile better than the average for all point masses and windows (k = 23 N/m, c = 8.1 N-s/m). As expected, a large spring constant affects the steepness of the radial distance profile due to a higher force being applied to the point masses at the initial position. A large damping coefficient lessens the overshoot of the radius that corresponds to the neutral spring force separation. However, an overshoot of the markers appears absent from the data. This could be from the restriction of the blankets unfolding completely, but there is no discontinuity in velocity or

acceleration at the peaks of the radial distance data that would suggest an abrupt boundary was reached during deployment.

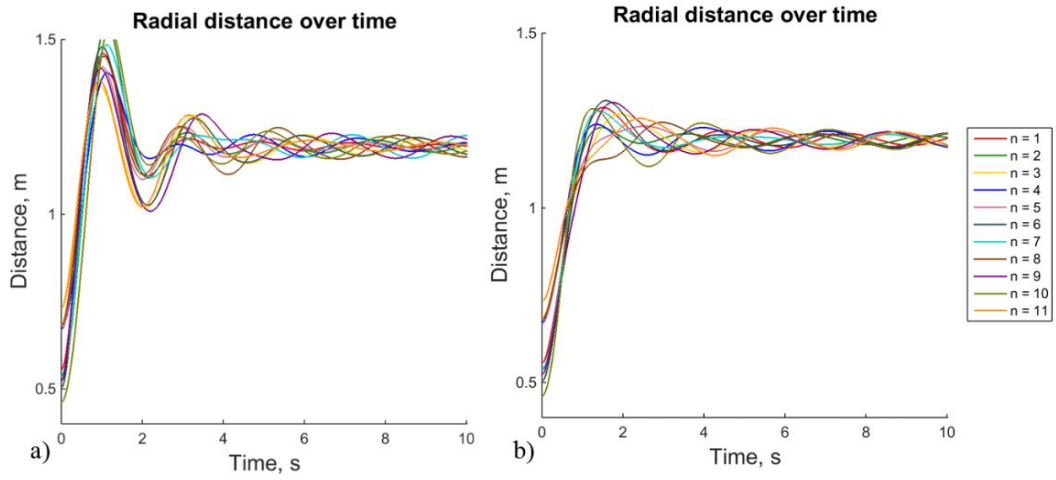

Figure 4.12 Model predicted motion using Test No. 54 initial conditions with a) test average values for properties, b) values for $n = 1$ at first time window

For both recreations in Figure 4.12, the point masses do not settle completely to the radius of neutral force, but it should be noted that the data shown in Figure 4.10 shows that the markers did not settle within the period of testing time either. To further explore this observation, a deployment prediction is shown where initial conditions are modified such that the point masses all start at the same radial distance.

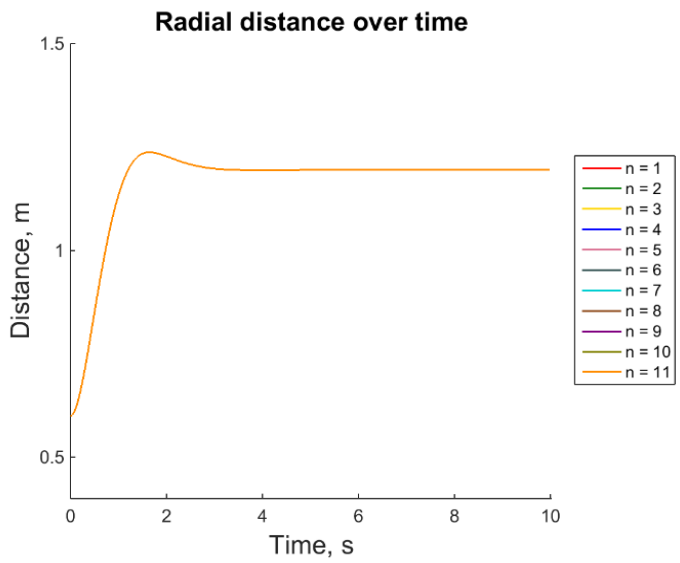

Figure 4.13 Model prediction with all point masses starting at same radial distance

The *k* and *c* is the same as Figure 4.12b and the starting radius for all point masses is 0.6 meters. As expected, the point masses progress in the exact same manner. Unlike the data (Figure 4.10) and recreations (Figure 4.12), the point masses settle to the radius that corresponds to the neutral separation distance in less than one oscillation with less overshoot. This suggests that the initial conditions of the point masses are influential on the final state of the deployment over a finite time.

4.3.3 Prediction of test article deployment in space

In order to investigate expected deployment of the test article in space, the model is modified to remove the force contribution due to rope tension and effectively the force due to gravity. Figure 4.14 shows the progression of the point masses using only the forces of the spring and damper elements. Using the same values for k and c and the same initial

conditions, Figure 4.13 shows an even smaller overshoot and quicker settling time compared to recreation of the motion using the laboratory conditions.

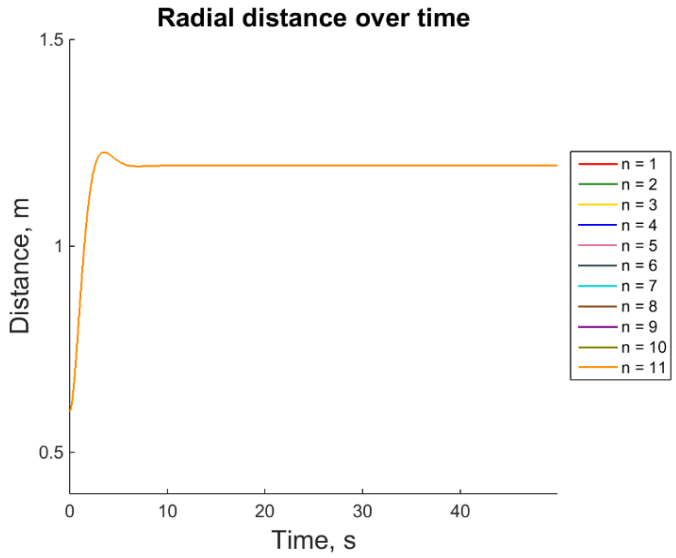

Figure 4.14 Predicted deployment of test article in space environment

The model showed that for initial conditions where the point masses were not at equal radial distances, the oscillations progressed in an unstable manner where the oscillations would not dampen out and some of the point masses were driven to final positions that were not intended final radius. This further indicates that initial conditions is important to a system of this kind.

4.4 Deployment investigation conclusions

The deployment motion of the thermal enclosure test article is described using the equations of motion for a simple mass-spring-damper system. The variations in the effective spring constant and damping coefficient may be due to the irregularity of the test

article compression at the start of the deployment test. The model was validated by recreating the deployment motion of a particular data set using only the initial position of the markers and a representative mechanical properties. The model was modified for conditions where the rope tension and force due to gravity are absent to predict the deployment of the test article in space. The results from this investigation will be used in examination of the selected point design of a full thermal enclosure.

Chapter 5: System Design

5.1 Point design

To summarize the results and conclusions from the thermal and deployment testing and analysis, a particular point design is examined. The material properties applied to the point design match the properties of the test article with the exception of using FEP Teflon as the outermost layer, which affects only the outer surface properties. The thermal conductivity and specific heat of the insulation remain the same as the test article. The thickness of insulation was traded with the number of equally spaced cryocoolers that also require additional mass allocation for the power system.

5.1.1 Selection of application of interest

The application selected for the point design is the shielding of a spacecraft from of high energy particles. More specifically, a single coil with a major radius of 10 meters from the configuration presented by Shepard [10] shown previously in Figure 1.3a is selected. The proposed total current of the assembly was 107 MA divided amongst 16 concentrically-stacked coils of varying radii that create the donut-shaped spacecraft, not including the coils nested inside to generate a null region in the spacecraft volume. Therefore, the current running through the single coil is approximately 6.7 MA.

Using a high current density of 459 A/mm^2 demonstrated by the SuperPower second-generation HTS material, a minimum square cross-section of length 120 mm (d) per side was required. The HTS coil is depicted as a thick band in Figure 5.1. The enclosure must allow for the coil to fold in the S-curve pattern for compact stowage. If the major

diameter of the coil expands from 5 m to 20 m, the enclosure circumference must also elongate by a factor of 4. The minimum bend radius (r_{bend}) is depicted in Figure 5.2 by the small circles. As alternating circles are brought together, the sides of the coil get closer. The minimum distance (L_1) between two bends of the S-curve is reached when the sides of the coil touch. The points marked by the stars (*) elongate to a separation distance of L_3 in the fully deploy state. To achieve a deployment ratio of 4, the ratio of L_3 over L_1 must also be 4. The minimum enclosure diameter is labeled L_2. Equations (5-1), (5-2), and (5-3) describes the relationship between L_1, L_2, L_3, the size of the coil stack, and the horizontal separation between the S-curve centers of curvature (h).

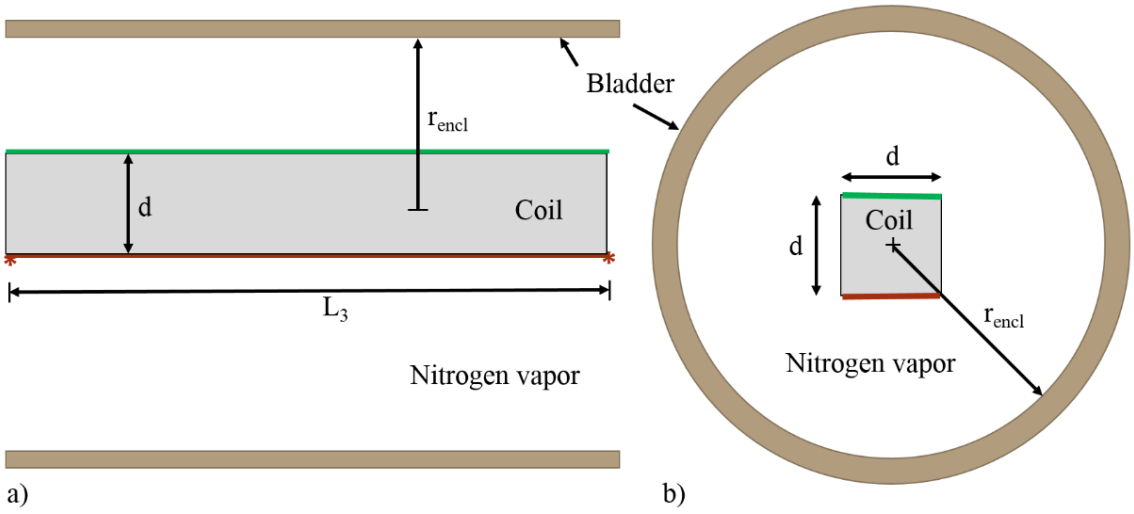

Figure 5.1 HTS coil inside enclosure when elongated for full deployment a) side view, b) cross-section of minor diameter

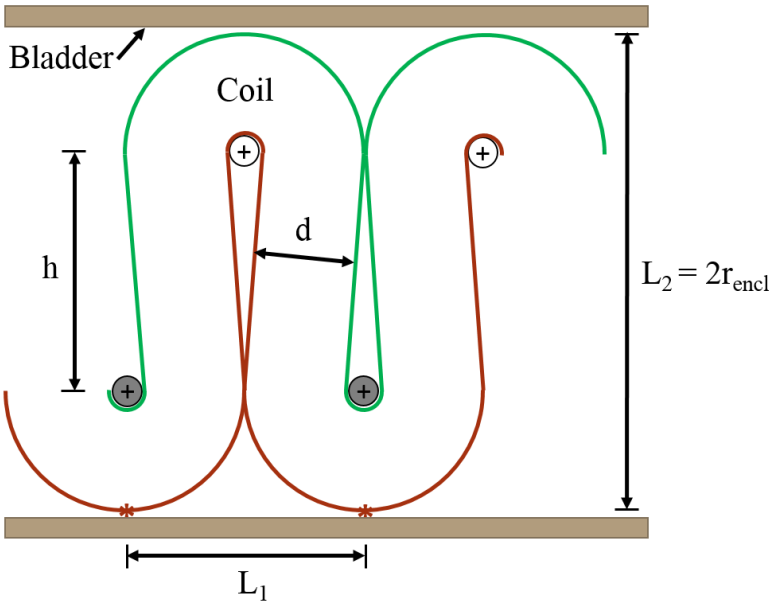

Figure 5.2 HTS coil curved in stowed configuration

$$L_1 = 2d + 2r_{bend} \tag{5-1}$$

$$L_2 = h + 2d + 2r_{bend} = h + L_1 = 2r_{encl} \tag{5-2}$$

$$L_3 = 2h + \pi r_{bend} + \pi(r_{bend} + d) \tag{5-3}$$

Given the known major diameter before and after deployment, the minimum diameter of the vapor core (L_2) of the enclosure is 31.5 cm.

5.1.2 Component sizing for point design

A major component of the system design for a particular point of interest is the cryocooler that extracts heat from the vapor in the enclosure core. Given the expected range of the thermal load based on the size of the enclosure, the cryocooler selected for trading with insulation thickness is the Stirling-type CryoTel GT made by SunPower for its 15.0

W of cooling power at an input power of 240 W and mass of 3.1 kg [28]. The mass associated with the solar arrays and power management system required to deliver the input power used an assumed value of 25 W/kg [50]. The test article insulation had a density of 87.7 kg/m^3. The system mass also includes the bladder and restraint layers of the enclosure, and the springs and collars for aiding in deployment and structural support.

The thermal design is strongly dependent on the outer surface area of the enclosure since the majority of incoming heat is due to incident solar radiation. Changes in the outer surface area are related to the surface area of the vapor core. The vapor core surface area varies with the number of segments used to enclose the HTS coil. As the number of segments increases, the diameter of the core decreases since it more closely follows the circular path of the coil. Figure 5.3 shows the vapor core surface area decreases as the number of segments increases from 10 to 100. Note that 119 segments corresponds to the number of segments comprising the enclosure if the springs are the same length as the test article.

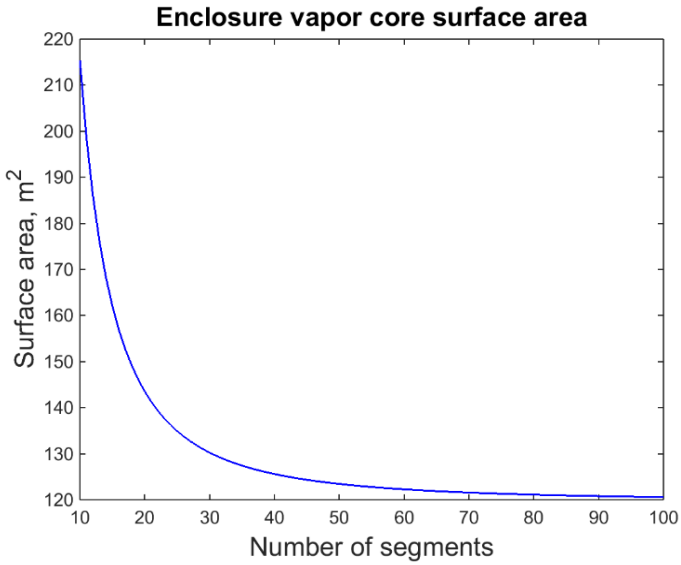

Figure 5.3 Change in vapor core surface area by varying number of segments

The enclosure dimensions change due to the number of segments, influencing the mass of the system. The mass of the material layers (bladder, restraint, and insulation) and structural components (springs and collars) changes as the number of segments increase, as shown in Figure 5.4. The thickness of insulation assumed for this calculation is 2 mm. The material layers use the same material densities as the test article. The collars are based on the standard sizes of schedule-40 PVC to maintain the same material as the test article. The suitable pipe diameters range from 8 inches to 24 inches at increments of 2 inches for this range of vapor core diameters. The mass of the collars uses the standard mass per length of pipes at the appropriate diameter, which results in some discontinuities in the progression of mass (more apparent in Figure 5.4b). The minimum mass for the material layers and structure occurs at 17 segments. This point of minimum mass is primarily a

result of trading wider diameter pipe for the collars for a fewer number of collars. With 17 segments, the vapor core diameter is 39 cm (15.2 inches) and the spring length is 3.56 m.

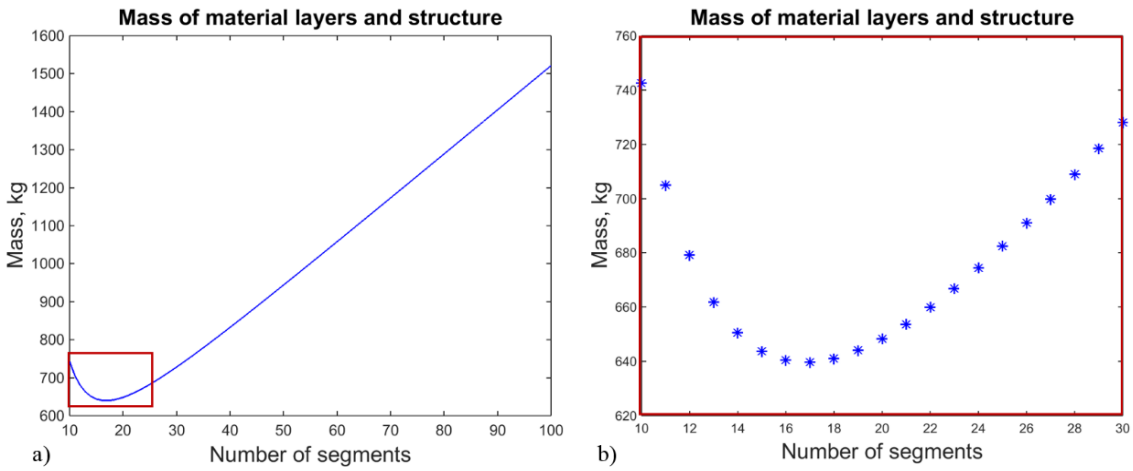

Figure 5.4 Mass of material layers and structure as number of segments vary from a) 10 to 100, b) 10 to 30

After establishing the number of segments that make up the enclosure, the number of cryocoolers and a fine tuning of the insulation thickness can be found. The cryocoolers are assumed to be evenly spaced around the major circumference of the enclosure. By adding cryocoolers, the distance between cryocoolers is shortened, which means a reduction in the flow path for heat to enter before reaching the next point of heat extraction. With the flow path shortened between cold points (location of cryocooler) and warm points (just before the next cryocooler), the amount of insulation necessary to keep the warm points below the 130 K threshold decreases, which in turn decreases the total insulation mass. However, adding a cryocooler adds the mass of the cryocooler plus the power system mass associated with supporting it.

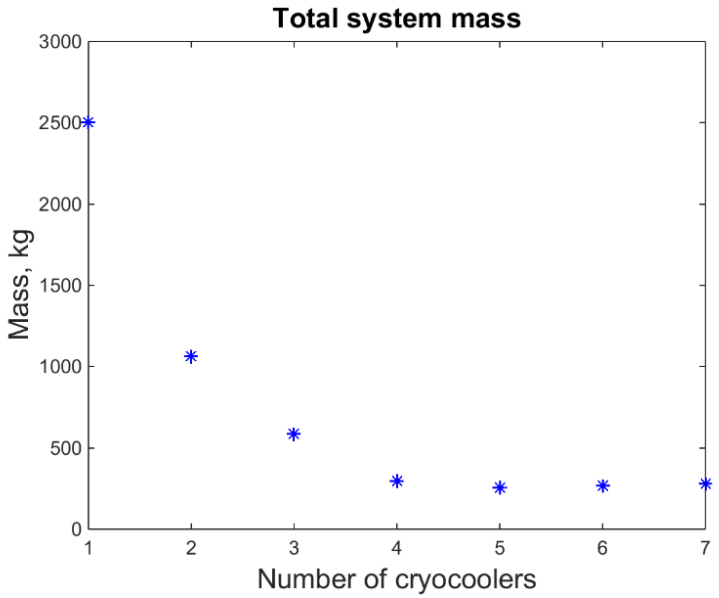

Figure 5.5 Total system mass vs number of cryocoolers

The change in total system mass as the number of cryocoolers increases is shown in Figure 5.5. For each evaluation, the minimum insulation thickness is used, however, there is a practical fabrication minimum of 1.5 mm so that the combined insulation and outer surface (FEP Teflon) remain opaque. The insulation also performs better when multiple shield and spacer layers are included so that the insulation has a radiative heat transfer through the layers, rather than conductive. Figure 5.5 shows that for a fixed number of segments, the system mass is minimized when using five cryocoolers. A summary of this selection for the system design is shown in

Table 5-1.

Table 5-1 System summary of point design

	Quantity	Mass
Number of segments	17	
No. of cryocoolers	5	15.5 kg
Cryocooler power	1200 W input	48.0 kg
Insulation	1.5 mm thickness	26.7 kg
Springs		17.3 kg
Bladder		41.6 kg
Restraint sleeve		53.4 kg
Collars		53.3 kg
	Total mass	**256 kg**

Assuming a mass flow rate of 1.3 g/s (60 LPM of nitrogen at standard conditions), the insulation thickness necessary to maintain the warm points below the critical temperature is the minimum allowable at 1.5 mm. The convective heat transfer rate from the inside surface of the bladder to the flow and from the flow to the coil is the same as the estimated convective heat transfer rate found during laboratory testing. However, if the pressure in the bladder is varied, the mass flow rate would also need to change to maintain the same rate of heat transfer. Recall that the convection coefficient can be estimated using the Nusselt number relationship for laminar, fully developed flow, which shows that the convection coefficient is proportional to the conduction coefficient. The conduction coefficient can also be approximated as proportional to the pressure inside the bladder for a constant temperature, therefore, the convection coefficient is proportional to the nitrogen vapor pressure in the bladder. The means that a decrease in bladder pressure results in a proportional decrease in the heat that enters the flow from the bladder surface, however, it also means a proportional decrease in the thermal energy that can be extracted from the

HTS coil in the center of the flow. The heat transfer rate is primarily dictated by the selected mass flow and flow pressure. If the pressure is decreased, the mass flow rate must proportionally increase to maintain the same heat transfer rate.

For 17 segments (N) and 5 cryocoolers (N_{cryo}), the allowable temperature rise is 3.4 K per segment if the cold points are at 77 K (T_{cold}) and the maximum allowable warm point is 130 K (T_{warm}). Given these bounds, the heat transfer rate for a mass flow rate ($\dot{m}$) of 1.3 g/s is 21.1 W as shown by the relationship in Equation (5-4).

$$q = \dot{m} c_p \frac{T_{warm} - T_{cold}}{N / N_{cryo}} \tag{5-4}$$

An increase or decrease in the pressure of the enclosure would result in an opposing decrease or increase, respectively, of the mass flow rate. The bounds of the mass flow rate are dependent on details of the fluid system used for circulating the nitrogen vapor, which is considered out of the scope of this investigation.

From a deployment standpoint, the pressure inside the bladder is compared with the deployment force exerted by the springs. The average pressure inside the bladder during laboratory testing is approximately equal to standard atmospheric pressure. Since the pressure inside the bladder is uniform, the force due to inflation pressure, P, can be found by first finding the surface area difference between the radially pointing outward half (red surface) and the radially pointing inward half (blue surface) of the enclosure shown in Figure 5.6.

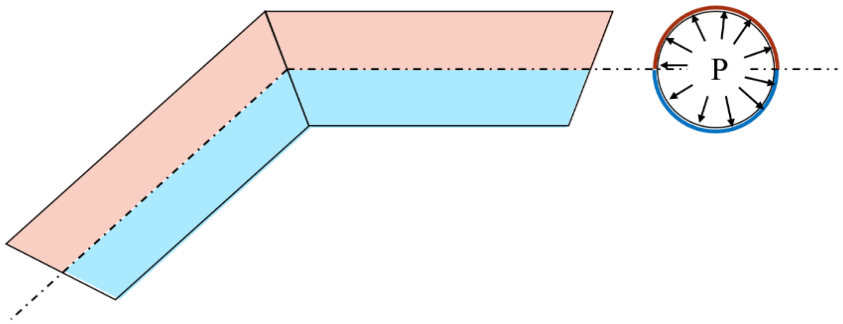

Figure 5.6 Inflation pressure on the inside of bladder for two adjacent segments

The two surface areas can be found using the major and minor radii (R_c and r_e, respectively) of the enclosure and the total number of segments, N, as depicted in Figure 5.7. The length of the middle chord that marks the major radius of the coil is labeled c. The inward and outward sides of one segment are labeled a and b, respectively, located at radial distances R_a and R_b. Equations (5-5) through (5-10)(2-1) give the relationship between the dimensions of the enclosure and the surface areas. The force resulting from the difference in surface areas for a constant pressure is given by Equation (5-11) .

$$2r_e = R_b - R_b \tag{5-5}$$

$$a = 2R_a \tan\left(\frac{\pi}{N}\right) \tag{5-6}$$

$$b = 2R_b \tan\left(\frac{\pi}{N}\right) \tag{5-7}$$

$$c = 2R_c \tan\left(\frac{\pi}{N}\right) \tag{5-8}$$

$$A_{in} = \pi r_e \left(a + \frac{c-a}{2}\right) \tag{5-9}$$

$$A_{out} = \pi r_e \left(c + \frac{b - c}{2} \right) \tag{5-10}$$

$$\Delta F = P(A_{out} - A_{in}) = P\pi r_e \left(\frac{b + 3a}{2} \right) \tag{5-11}$$

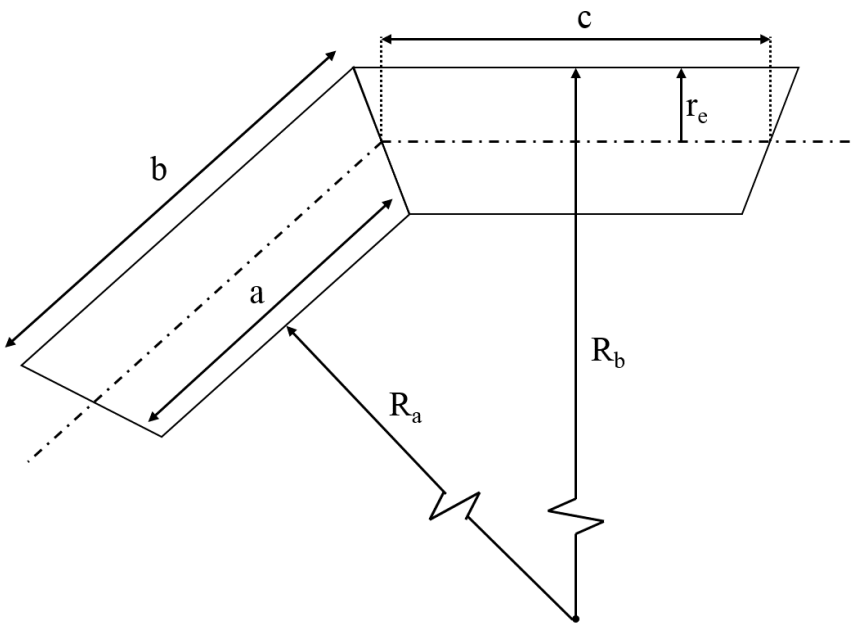

Figure 5.7 Dimensions for finding surface areas for pressure force

The same force is also being applied from the adjacent segment on the other side, so the net force is twice the value of only the radially outward component as shown in Figure 5.8. For the test article, operating at near standard atmospheric pressure results in a net radially outward force of approximately 9 kN. For the point design, the larger dimensions would result in a force of 202 kN. These forces are quite large so it may be beneficial to decrease the operational pressure inside the bladder to proportionally decrease the force. This benefit of decreasing the force exerted by the pressure inside the bladder must be balanced with the details of the vapor supply system, which would limit the mass

flow rate. As previously mentioned, a decreased bladder pressure would require a proportionate increase in the mass flow rate to maintain the same amount of heat extraction from the system.

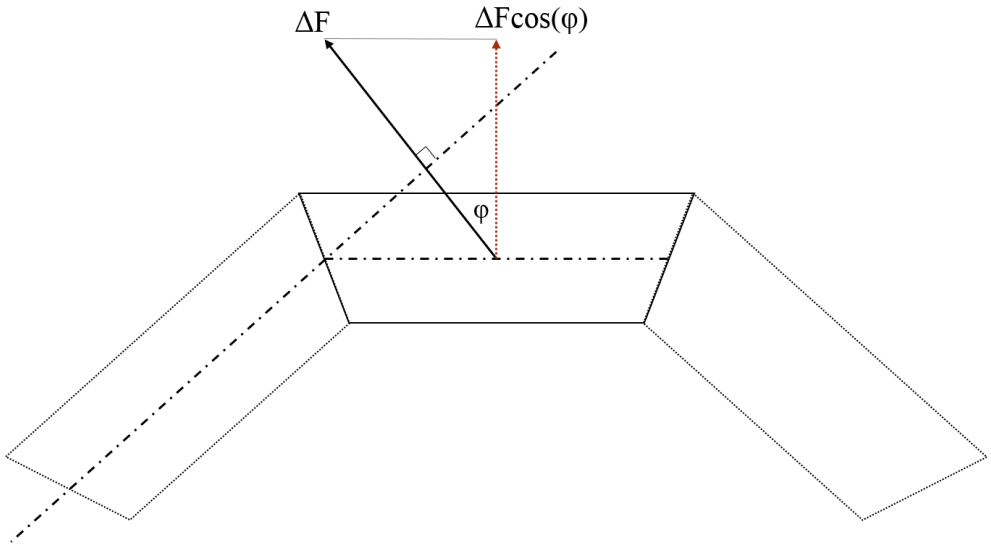

Figure 5.8 Force acting the center segment due to the segment on the left side

The mass of the bladder and restraint layers along with the springs and collars listed in

Table 5-1 do not change with the number of cryocoolers. The total mass refers to the total mass of the enclosure and only the solar arrays necessary to power the cryocoolers. It does not include the mass of the HTS coil. There is no reliable mass density information found for the superconducting material used in the 2G Superpower tape. Based on the density of other HTS ceramics, the coil could have a mass around 4500 kg (assuming 5 g/cm^3), which would make the enclosure, cryocoolers, and power system mass less than 6% of the total mass.

Up to this point the material properties used for the design have been the properties of the test article. However, the current standard for flight missions and the state-of-the-art for these materials is far better performing. More specifically, the insulation used for the test article is expected to under-perform. To understand the design space in terms of realistic flight conditions, the thermal conductivity of the insulation is allowed to vary along with the number of cryocoolers while the density of the insulation is examined at three discrete values. Johnson and Fesmire of NASA tested MLI with densities ranging from 45 to 95 kg/m^3 [51].

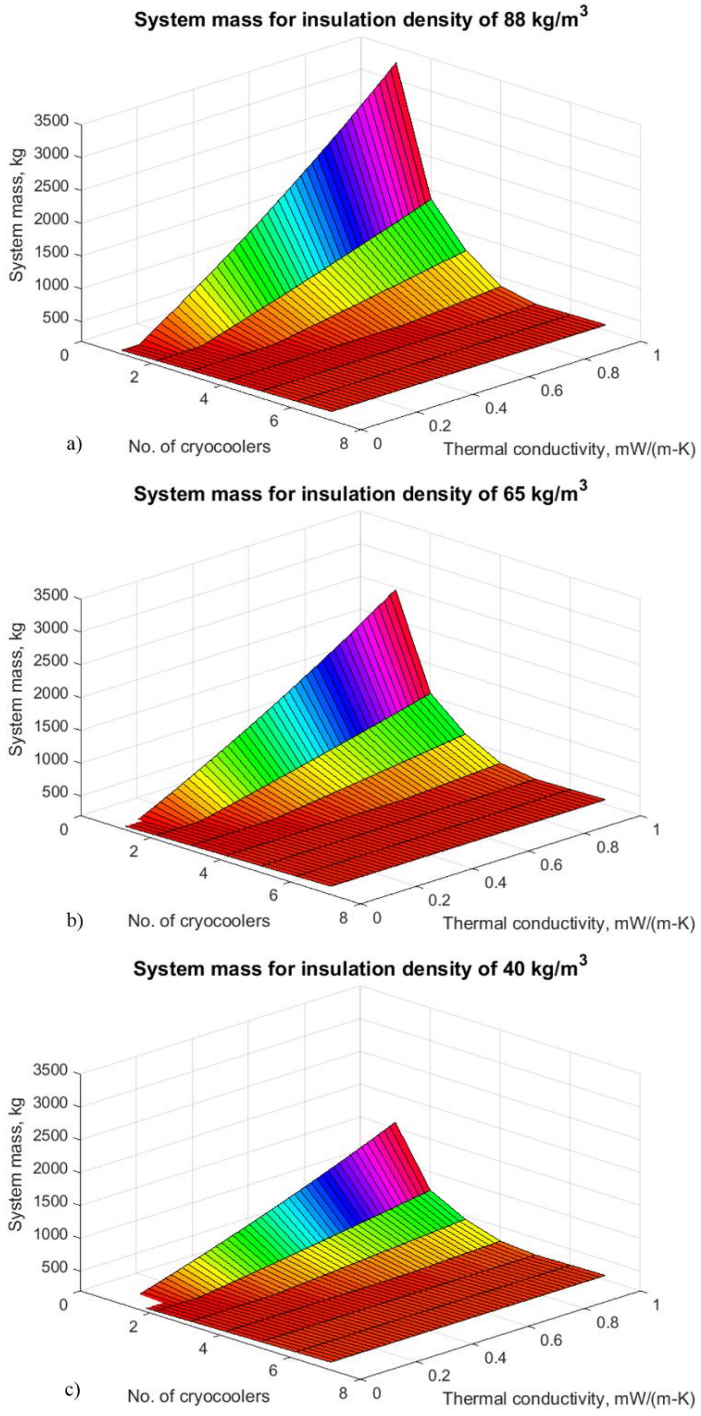

Figure 5.9 System mass as number of cryocoolers and insulation thermal conductivity vary for a) 88 kg/m^3, b) 65 kg/m^3, and c) 40 kg/m^3

The mapping of the insulation thickness (Figure 5.10) is the same for all three cases shown in Figure 5.9. As previously noted, small variations in the insulation thickness result in large increases in system mass. For most points on Figure 5.10, the thickness of insulation is at the minimum allowable value of 1.5 mm. The insulation increases to other values only when the number of cryocoolers is small and thermal conductivity is high.

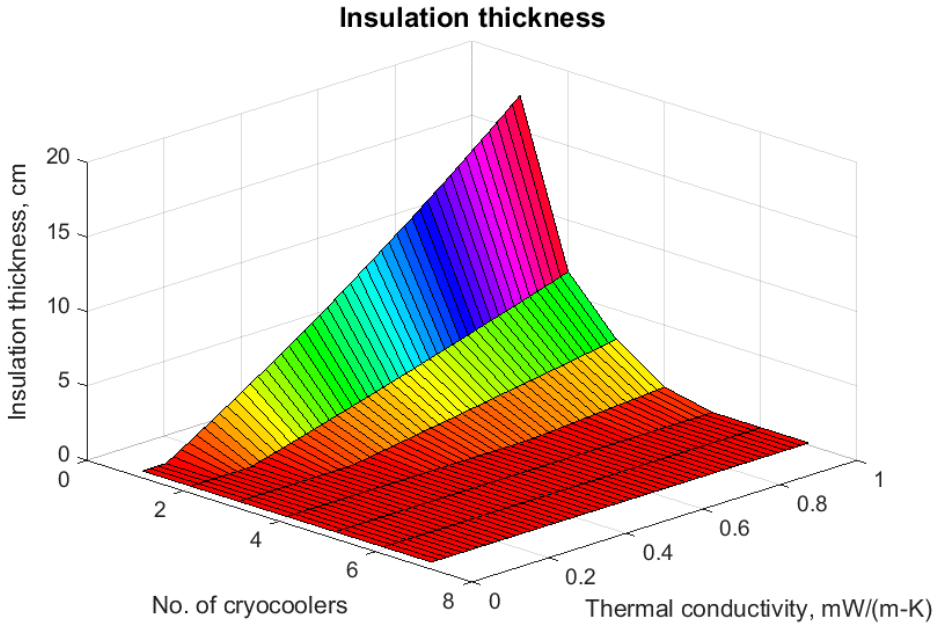

Figure 5.10 Insulation thickness with changes in number of cryocoolers and thermal conductivity

The springs need to supply very little force since there is no force preventing the enclosure from reaching its fully deployed size. Figure 5.11a shows the deployment motion for the point design enclosure using 17 segments with the test article values for the spring constant and damping coefficient. As previously mentioned, overextending the enclosure beyond the size associated with the neutral spring force may be undesirable and unrealistic.

The insulation layers are meant to be pulled taut so the panels properly overlap each other and close gaps in the insulation layers. The material is not capable of stretching, so if the deployment motion tries to extend the separation of the collars beyond the neutral distance, it could damage the insulation panels. Choosing the spring design for a lower spring constant would decrease overshoot. Figure 5.11b shows the deployment motion for springs with k = 5 N/m and compares deployment for different values of the damping coefficient. A large c greatly reduces overshoot in the first oscillation, where values greater than 20 N-s/m display hardly any overshoot.

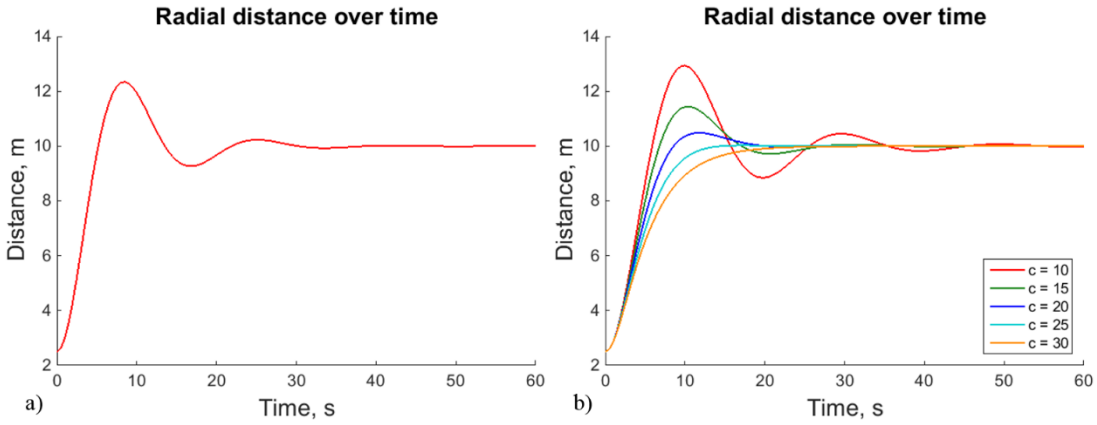

Figure 5.11 Deployment prediction using a) k = 6.9 N/m and c = 14 N-s/m, b) k = 5 N/m and varying c with units of N-s/m

The spring constant is related to the spring material and dimensions by Equation (5-12). The spring wire material is assumed to be music wire (ASTM A228), the same material as the test article springs with a shear elastic modulus of 80 GPa (G). A wire diameter (d_w) of 5 mm is chosen and the spring radius (r_c) is 17 cm to match the vapor core

radius associated with 17 segments. From these values, the number of turns for the spring is 32.

$$k = \frac{G{d_w}^4}{64n{r_c}^3} \tag{5-12}$$

$$c_s = \frac{2r_c}{d_w} \tag{5-13}$$

The spring index (c_s) found using Equation (5-13) is 34, which is larger than the recommended upper bound of 15. This may make the spring difficult to manufacture. The ratio of the length to diameter of the spring is also large which may make the spring susceptible to buckling. This could be addressed by using additional support structure to help guide the springs during compression and perhaps also help increase the effective damping coefficient.

5.2 Literature review of debris and puncture mitigation

The design of the thermal enclosure relies on the working fluid as a vapor in a pressurized container. This inherently makes the design sensitive to punctures or leaks that could cause loss of the working fluid, which should be considered irreplaceable for a system operated in space. The purpose of this trade study is to identify enabling technologies related to this concern.

Three primary topics are identified when reviewing previous research related to the mitigation of damage due to debris impact: detecting a puncture using sensors, materials that prevent damage from occurring, and materials that can repair inflicted damage.

Puncture detection alone is not considered to be sufficient given the severity of the impact it would have on the operation of an enclosure; however, detection could aid repair efforts. For an enclosure that may be part of a structure large enough to occupy humans, detection may be helpful in identifying areas needing repair or maintenance [52].

A summary of expected damage for gas retention structures and space suits presented by Ferl et al. is applicable to the concept of a thin-walled vapor enclosure [57]. Among the damage threats identified, micrometeoroid and orbital debris (MMOD) have the highest impact velocity and can vary in size. The distribution and probability of MMOD would depend heavily on the mission. This summary is especially applicable regarding threats due to the compact stowage process, vibration loads during launch, and then deployment. The assessment of damage mitigation methods must take into account the type of anticipated damages and the associated risk of incurring them.

Table 5-2 Applicable threat mechanisms gas retention structures [57]

Threat	**Risk**	**Damage anticipated**
MMOD (6-15 km/s)	Based on size	1 mm-100 mm holes (jagged, possibly elongated)
Impact from outside ≤ 10 m/s	Low	1 mm-100 mm long cuts (jagged or smooth edges, some strain effects
Packing ≤ 0.5 m/s contact within material	Low	Pinholes or micro-cracks
Deployment ≤ 0.5 m/s contact within material	Low	Pinholes or micro-cracks
Seam opening	Low	Lift at ends of bladder layer
Material degradation	Based on age	Tensile, tear strength, modulus change (radiation, hydrolysis, microbial growth, abrasion from dust)

Vibration damage (launch)	Low	Abrasion

5.2.1.1 Damage protection

Preventing damage would be preferred over withstanding and then repairing damage since the repair process would still involve loss of some working fluid. However, some technologies could be applied along with repair methods.

Damage protection can also be viewed as protecting only against punctures that result in working fluid loss. One method to achieve this would be to fabricate the enclosure with redundant bladder layers. In this way, the outer bladder layers could experience debris impacts, but at least one bladder layer would remain intact. Other methods would be selecting restraint layer materials that have long, reinforced fibers for load-bearing forces [55] or impregnating a fabric with an epoxy that hardens upon exposure to certain environmental stimulus. This could include hardening of the outer surface layer with ultra-violet radiation or the inner restraint layer by exposure to vacuum.

5.2.1.2 Repair methods

In the event that damage causing a leak in the bladder is sustained, a repair is needed to prevent irreplaceable loss of the cooling gas. While repairs to a large structure could be done by robots or humans on an extravehicular activity, the response time would be long and the repair would require additional equipment or personnel allocation with substantial risk. In contrast, self-healing materials are favorable because they do not inherently need

any external resources. The self-healing material would be integrated into the design of the enclosure.

Hager identified four terms useful for classifying materials capable of self-repair: automatic, non-automatic, intrinsic, and extrinsic [53]. Non-automatic meant the repair process required an external trigger. This typically involved addition of energy or exposure from an outside source such as ultra-violet light, vacuum, heat, or oscillating magnetic field [53,54]. Automatic materials did not require a trigger for the self-repair process to begin. This should not be confused with autonomous versus non-autonomous since all of the self-repair technologies identified were autonomous in that they do not require intervention from a human or robot. Separately, materials were classified as intrinsic if the material being healed inherently had self-repair properties versus an extrinsic classification that meant a substance had to be added to the material to make it capable of self-repair. An example of an intrinsic, automatic material was a polymer that seals from surface adhesion [53], but it has been found that adding reinforcing fibers (making it extrinsic) helped recover stiffness of the material [55].

Many approaches to self-healing involve chemical reactions. An approach of interest was the addition of microcapsules to a material that, when punctured, fill the void created by the crack [56] as shown in Figure 5.12a. Other approaches involve a foaming reaction. The foaming can be triggered by a catalyst seeded in the nitrogen gas that reacts when exposed to microcapsules embedded in a layer on the outside of the bladder or exposure of two reactants normally separated by one of the bladder layers [57].

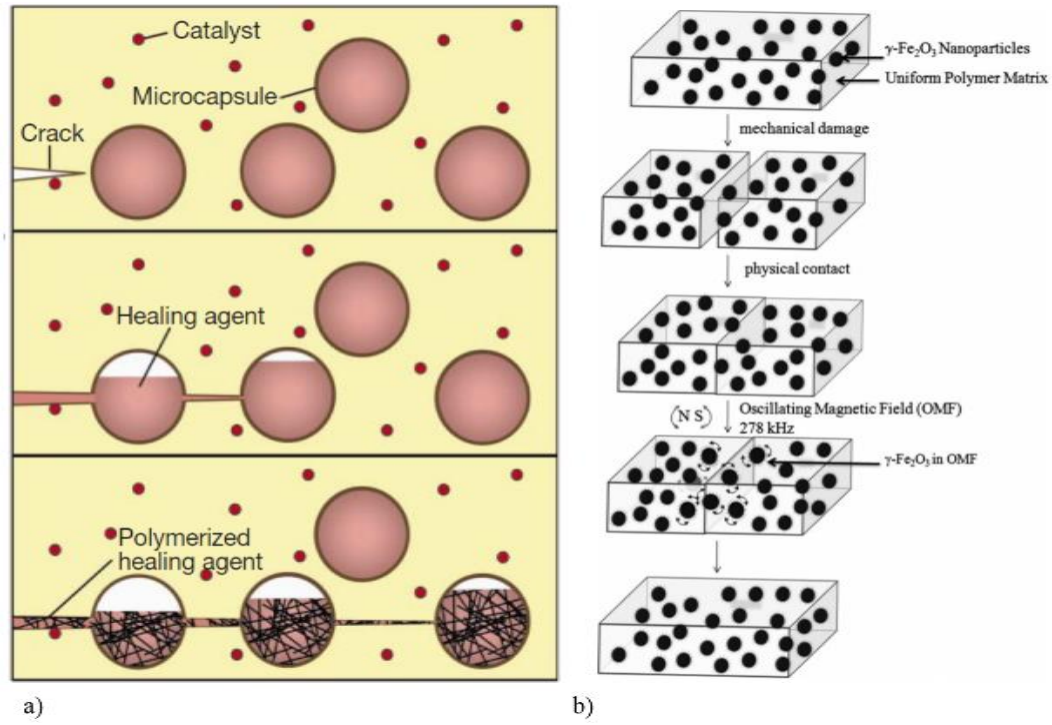

Figure 5.12 Self-healing method a) embedded microcapsules [56], b) triggered by oscillating magnetic field [54]

Mechanical methods for self-healing have also been researched. Experiments have shown that pushing fibers through a hole is an effective method of blocking a void [57]. One method (Figure 5.13a) suggests a woven fabric with long fibers extending out. The escaping gas provides the pressure force that pushes the fibers into the void. Another mechanical technique uses a dense, closed-cell polyurethane coating under strain by the restraint layer when inflated (Figure 5.13b) [58]. When damage is inflicted, the strain on the coating pulls the surfaces of the crack together to create a seal.

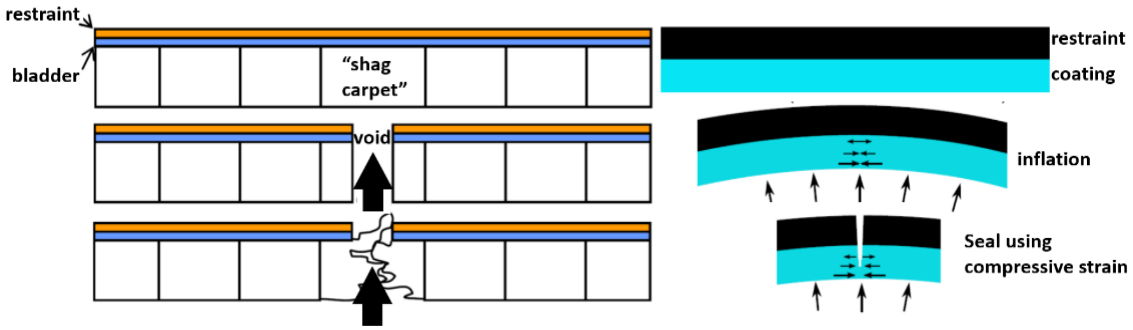

Figure 5.13 Examples of mechanical self-healing method using a) fibers to block void [57], b) strain on polyurethane coating to close void [58]

None of these approaches have been tested under cryogenic conditions. Some methods such as the long fibers meant to block a void may work effectively in extremely cold temperatures while methods such as the flowing of viscoelastic gels would probably not. The restraint layer is subjected to substantial forces due to the pressure of the nitrogen gas inside the bladder. For this reason, the repair method must also be capable of sufficient strength recovery to prevent crack propagation or catastrophic rupture. Methods of self-healing with low technology readiness levels (TRL) have not been characterized for conditions expected in a space mission such as outgassing, radiation, ultra-violet light exposure, and vibrational loads. The additional mass to the system required to integrate a self-healing method and the ability to fold and deploy with the other material layers without reducing its effectiveness must also be considered.

Chapter 6: Conclusions & future work

The work presented in this dissertation focused on the concept, evaluation, modeling, and design of a thermal enclosure for a large HTS coil with the capability to deploy in space. A thermal management system maintains the HTS material below its critical temperature, which is required to achieve a superconducting operational state. The ability to deploy is necessary for delivering coils with major diameters much larger than the interior dimensions of a launch vehicle payload fairing. Specifically, this dissertation contributed the following items to the state-of-the-art of superconducting coils in space:

1. Presented a concept for deployable thermal enclosure for an HTS coil
2. Developed a method for experimentally determining thermal properties of a thermal enclosure test article using a limited number of locations for measuring temperature
3. Identified an optimal flight design for a specified requirement set by trading thermal system dimensions and mass with power system mass
4. Used correlated static and dynamic deployment testing to develop a model for predicting deployment motion in space
5. Identified several candidate self-healing technologies to address puncture vulnerability

The following sections discuss the major conclusions related to these contributions and the suggested future work that could further advance this technology.

6.1 HTS coil enclosure concept

The concept was heavily influenced by the decision to use a thin-walled thermal enclosure with forced nitrogen vapor flow for cooling the HTS coil. Using rigid heat pipes would be unsuitable for large coils intended to fit inside current payload fairings. Metal bellows were capable of bending, but were still not flexible enough to house a coil with a stowed size of 5 meters and a final deployed diameter of 20 meters. A thin-walled enclosure similar to the layers of a spacesuit or inflatable habitat satisfied the need for a high ratio of deployed to stowed size. The inner most layer was a bladder layer (or redundant bladder layers) that contains the nitrogen vapor. The minimum minor diameter is defined compression springs connected in series around the major circumference of the enclosure. These springs doubled as a structural element and source for a deployment force. The minor diameter was restricted by a restraint layer that bore the stress of the vapor pressure transferred by the slightly oversized bladder. A multi-layer insulation blanket and outer cover provided thermal insulation.

Progress in manufacturing techniques for HTS materials in the form of thin tapes was a key development that enabled this design concept. Deposition of the HTS material onto substrates rather than laminated extrusions allowed for a much smaller acceptable bend radius. This small bend radius was utilized in the concept for compactly stowing the coil (consisting of many turns of HTS tape) when forming the S-curve pattern inside the bladder.

The test article was fabricated to perform both the thermal and deployment investigations. The quality of construction was limited by the materials available and the in-house manufacturing capabilities. For those reasons, the test article was not able to perform to the full potential of the enclosure design concept. However, the fabrication of the test article helped reveal important concept development, such as the use of overlapping MLI blanket panels. The decision to use overlapping panels was originally driven by the need to simplify the fabrication process. Other methods such as connecting pieces of the MLI together in an accordion-inspired manner proved to be very time-consuming. For a flight system, the accordion-inspired design would still not be preferred over the overlapping panels because the increased number of seam stitches would introduce a source of heat leaking. Additionally, the accordion-inspired design does not lay as flat when deployed, which means more self-reflection and less external emission from the outer surface. The overlapping panels have also demonstrated a high stowage ratio that allowed for complete compression of the springs whereas other concepts caused interference from the material bunching up during compression.

6.2 Experimental approach for finding thermal properties

The thermal vacuum experiments allowed for the thermal properties of the test article to be found using a very limited number of locations for temperature measurements. The values of the thermal properties varied significantly during the course of each test. This was most likely due to the variability in test conditions such as the vacuum chamber pressure and the nitrogen vapor flow rate. The seams in the chamber walls and feedthrough

ports often developed cracks that prevented the chamber pressure from ever reaching below 10 mbar (the threshold for using the turbo-pump in addition to the rough pump). This caused the heat transfer by conduction and convection through the residual gas in the chamber to be significant. For future work, thermal tests could be performed at a much lower chamber pressure so that a prototype enclosure could be evaluated in conditions where radiation to the outer surface and between shield layers of the MLI would dominate over conduction and convection. Fabrication of MLI blankets using higher quality materials would also yield results closer to the expected performance of a flight system.

With the material properties of the test article experimentally determined, a model was used to predict the performance of the same test article in a space environment with heat loading due to solar radiation, Earth albedo and radiation, and the background space radiation. It was found that replacing the outer most surface material with FEP Teflon with a silver backing greatly reduced outer surface temperature and the heat transferred to the vapor core. This was due to the higher emissivity despite lower resistivity compared to the surface properties of aluminized Mylar.

It was difficult to determine the flow temperature with the limited number of thermocouple locations. The thermocouples could not be placed directly in the flow due to risk of creating a leak or rupture in the bladder. The caps that sealed the ends of the bladder and restraint layers only accommodated the tubes for the nitrogen vapor flow in and out of the enclosure. Advanced manufacturing techniques would also allow for the insertion of a thermocouple in the flow. At a minimum, a thermocouple located at the flow inlet and at

the flow outlet (or location of warmest flow) would provide insight into the actual heat rate into the system. A design for joining the two ends of the enclosure similar to the ring cuffs used for attaching the gloves to the arms of spacesuits would greatly reduce the amount of vapor leaking that was experienced during testing due to different rates of material thermal contraction. This would also allow for an HTS coil or representative structure to be installed in the vapor core during thermal testing.

6.3 System design for flight mission

The system design examined Chapter 5 utilized the same material properties as the test article to determine the sizing of the enclosure and components in a realistic application of the enclosure for a space mission. This showed that even with under-performing materials compared to the state-of-the-art (or even standard flight) materials that the concept of using a thin-walled enclosure with forced vapor cooling could be used to deploy and thermally manage an HTS coil as large as 20 meters in major diameter. The enclosure was sized to accommodate the stowing of the coil in an S-curve pattern when the enclosure was in the compressed state. The number of segments was determined using an optimization of structure mass and the heat loading due to the outer surface area. The total system mass was minimized by trading the number of cryocoolers for insulation thickness necessary to maintain the enclosure below the HTS critical temperature of 130 K.

Improvement in the system design can be achieved by selecting alternative materials. As previously mentioned, using higher performing (meaning lower effective thermal conductivity) MLI would decrease the insulation thickness or number of

cryocoolers required to thermally manage the system. Polyvinyl chloride was used as the collar material. However, PVC is not a preferred material for flight missions due to outgassing. Other materials may be more suitable with higher strength to mass ratios that also meet standards for flammability and outgassing. For the system design of the selected flight mission, the collars were about one third of the structure mass. The restraint layer also made up about one third of the structure mass using a commercially available fiberglass bi-weave sleeve. A material substitution for the restraint layer may also result in a mass reduction.

Refinement of the thermal management system design could be achieved after prototype testing using a closed system for circulating the chilled nitrogen vapor. The thermal testing used an open system where the tank supplied the nitrogen vapor and the flow exited to the laboratory at atmospheric pressure. By building a prototype more representative of a flight design, a closed thermal system using cryocoolers to extract heat from the flow can be evaluated and the results could be used to refine the flight design.

6.4 Correlation of deployment testing and model

The static force testing a single segment, which included one spring, showed an effective spring constant of the enclosure assembly approximately doubled compared to the manufacturing specifications of the spring alone. Additionally, a model was developed to describe the motion of the collars as point masses connected by ideal spring and damper elements. Using this model, the effective spring constant and damping coefficient was found during dynamic deployment of the full test article. Surprisingly, the average value

of the spring constant was close to the value of the spring alone, which means it was half the value of the spring constant found during static testing. It was observed that the average spring constant and damping coefficient found during full deployment testing did not recreate the motion well when plugged into the model with the same initial conditions. This suggests that the motion is better described with spring constant and damping coefficient values that can vary over the course of deployment. Also, the deployment motion was heavily influenced by the tension in the ropes used to suspend the test article above the floor. Prototype testing in a more representative environment where the deployment is not affected by the force due to gravity would be helpful in developing a more refined deployment model.

The deployment methods of a flight system should be further investigated. During deployment testing of the full test article, it was observed that the springs tended to bow outward when the collars were brought together instead of compressing solely along the axis of the springs. Implementing a more sophisticated method of holding the collars so that the springs are compressed axially would also allow for more control during deployment. This could increase the effective damping coefficient, which the model showed was necessary for deployment motion with little to no overshoot. The test article enclosure was also deployed using a sudden release from the stowed configuration. However, it may be preferred to have a slow, controlled deployment to reduce harmonic oscillations that could be transferred to the attached spacecraft. This would most likely change the deployment response to more closely match the results from static force testing.

The model also suggests that integrating a way for the initial radial position of all the collars to be equal also helps reduce settling time and possible overshoot.

6.5 Self-healing technology for puncture mitigation

The survey of methods for puncture mitigation focused on self-healing technologies. The technologies varied drastically in their mechanisms of self-healing and evaluation of their performance making direct comparisons of the independent investigations impossible with the limited information available. Future work on the design concept presented in this work should include a rigorous investigation of different self-healing technologies using common tests and evaluation criteria related to the application an inflatable, nitrogen-filled enclosure at temperature below 130 K.

Puncture tests with the same tool could be used to evaluate healing response time and effectiveness of stopping the leak. The technologies need to also be assessed for compatibility in a vacuum environment and ability to fold with the other material layers for compact stowage of the enclosure. Once common measurements across the self-healing technologies are conducted, a selection process can be implemented.

6.6 Final remarks

As recent as 2009, researchers interested in applications of large superconducting coils in space were limited by the inability to deliver a coil with a diameter larger than a typical payload fairing. This dissertation presented a novel a concept for a housing an HTS coil inside a deployable thermal enclosure that uses nitrogen vapor for heat extraction. A

single representative prototype was fabricated for both thermal and deployment testing to prove the feasibility of the concept. The properties of the prototype were used in conjunction with models of the thermal and deployment performance to outline the system for a single coil that could be part of high-energy particle shielding of a spacecraft large enough for human occupancy. With further development, this concept and proposed flight design can be matured to increase the feasibility of delivering HTS coils of at least 20 meters in major diameter for various applications.

Appendix A: Cryocooler survey

Model #	Type	Stages	Cooling Power (W)	Cold Tip (K)	Input Power (W)	Hot Side (K)	Calc'd specific power	Reported specific power	Reported % of COP	Calc'd % of COP	Mass (kg)	Manufacturer	Space Mission	Operational time	Author	Year
LSF9320	linear Stirling		7.3	75	150.0		20.55					THALES Cryogenics			Trollier	2003
	turbo Brayton		7.1	73	375.0	278	52.82		6.3	5.3			NICMOS		Swift	2003, 2004
	pulse tube	1	15.0	85	200.0		13.33				23.00	Lockheed & Northrop			Foster	2003
		2	1.5	35												
HTS-3	pulse tube		300.0	80	4300.0	300	14.33		19.2	19.2		Praxair Inc			Zia	2007, 2004
LC1062	Stirling		1.5	77	50.0	296	33.33			8.5		Carleton Life Support Systems Inc			Squires	2009
MPTC	pulse tube	1	1.6	70	50.0	288	31.06	31.00		10.0	2.80	Air Liquide	GMES	5260 hrs	Trollier	2009
LPTC	pulse tube	1	2.0	50	140.0	283	70.00			6.7	7.00	Air Liquide			Trollier	2009
LSC	pulse tube	1	8.5	75	150.0	290	17.65			16.2	7.00	Air Liquide				
ABI	pulse tube	1	5.1	183								Northrop			Ramsey	2009
		2	2.3	53												
Ricor K508	rotary Stirling		0.7	77	11.5	233	16.43	15.50		12.3	0.45	CheMin and Ricor	Mars Science Lab	2100 hrs	Johnson	2009
	coaxial pulse tube		1.3	77	49.0	298	37.69	37.00		7.6		Northrop			Petach	2009
SF070	linear Stirling		0.4	80	25.0	344	62.50			5.3	0.85	AIM		25,000 hrs	Mai	2009
	Stirling	1	2.5	100									SUZAKU		Sato	2009
	Stirling	1	2.0	80									NEXT		Sato	2009
	Stirling	1	1.5	80									SELENE		Sato	2009
	pulse tube	1	3.4	80								RICOR & NIST			Garaway	2009
LPT 9710	coaxial pulse tube	1	15.0	80	300.0	296	20.00		15.0	13.5	16.00	THALES Cryogenics		9000 hrs	van de Groep	2009
LPT 9310	linear pulse tube		5.1	80	180.0	296	35.29			7.7	7.00	THALES Cryogenics				
LPT 9510	linear pulse tube	1	1.4	80	85.0	296	60.71			4.4	2.10	THALES Cryogenics				
PT-60	pulse tube	1	12.0	80	1000.0	300	83.33			3.3	7.30	Cryomech		12,000 hrs	Kelser	2009
PT-90	pulse tube	1	77.0	70	5000.0	300	64.94			5.1	8.20	Cryomech				
PT-10	pulse tube	1	10.0	70	1500.0	300	150.00			2.2	9.10	Cryomech				
	pulse tube		3.0	70	100.0		33.33					Fuji Electric		50,000 hrs	Matsumoto	2009
TRW	pulse tube		1.5	56	92.0	190	61.33	60.00		3.9		Northrop	AIRS	5.5 yrs	Ross	2009
	pulse tube	2	3.0	80											Yuan	2009

Model #	Type	Stages	Cooling Power (W)	Cold Tip (K)	Input Power (W)	Hot Side (K)	Calc'd specific power	Reported specific power	Reported % of COP	Calc'd % of COP	Mass (kg)	Manufacturer	Space Mission	Operational time	Author	Year
10K EM	pulse tube	1	1.0	50	200.0	300	200.00			2.5		Northrop	space qual		Jaco	2009
		2		40												
		3	0.1	10	200.0		1600.00									
SB160			1.6	60		298		1.82			10.50	Ball	HIDRLS		Kirkconnell	2007
RS1	Stirling		3.3	58	108.0	300	32.73	38.00		12.7	14.00	Raytheon			Barr	2004
HEC-1				45		300		1.11			4.30	Northrop			Kirkconnell	2007
HEC-2				45		300		0.87			4.30	Northrop			Kirkconnell	2007
65K SSRB				45		300		0.67			18.50	Creare			Kirkconnell	2007
CPT60	pulse tube		2.0	60	100.0	310	50.00			8.3		Sunpower			Wilson	2007
AL330	GM		150.0	50	6700.0	300	44.67			11.2	176.00	Cryomech		10,000 hrs	Tanchon	2007
AL325	GM		100.0	25	11200.0	300	112.00			9.8	22.00	Cryomech		8,000 hrs		
AL300	GM		285.0	70	7600.0	300	26.67			12.3	18.60	Cryomech		8,000 hrs	Tanchon	2007
AL600	GM		510.0	70	11500.0	300	22.55			14.6	41.80	Cryomech		8,000 hrs	Tanchon	2007
AL10	GM		13.0	70	1300.0	300	100.00			3.3	2.70	Cryomech		8,000 hrs		
2S241K	pulse tube		80.0	65	4200.0		52.50					Qdrive/Praxair			Tanchon	2007
	pulse tube		170.0	65	7800.0		45.88					Giessen Univ			Tanchon	2007
VLPTC	pulse tube		175.0	65	5500.0		31.43					Air Liquide			Tanchon	2007
	pulse tube		200.0	70	8600.0	300	43.00		7.6	7.6					Dietrich	2007
M87N	Stirling		7.5	77	150.0	273	20.00			12.7		Sunpower	AMS-02	40,000 hrs	Shirey	2003
CryoTel GT	Stirling		15.0	77	240.0	296	16.00		19.5	17.8	3.10	Sunpower				
CryoTel CT	Stirling		11.0	77	160.0	296	14.55		19.0	19.6	3.10	Sunpower				
CryoTel MT	Stirling		5.0	77	80.0	296	16.00		18.0	17.8	2.10	Sunpower				
	JT precooled by PT											Northrop	MIRI on JWST		Durand	2007
SB235E			10.0	85	255.0	293	25.50			9.6	14.40	Ball	PIXIE		Gully	2007
			8.0		150.0		18.75						AMS		Wang	2013
		1	1100.0	77	24600.0	300	22.36		13.0	13.0	270.00	Praxair		10 yrs	Potratz	2008
		1	140.0	80					11.0			American Superconducto			Sun	2010
		1	50.0	55					6.6			American Superconducto			Sun	2010
		1	302.0	77					11.7			Air Liquide			Sun	2010
		1	210.0	65					10.1			Air Liquide			Sun	2010
RSPL	pulse tube	1	21.9												Nguyen	2010
		2	2.3													
	Stirling	1											SXS on Astro-H			
		2														
			165.0	80					7.0						Ghahremani	2011

Model #	Type	Stages	Cooling Power (W)	Cold Tip (K)	Input Power (W)	Hot Side (K)	Calc'd specific power	Reported specific power	Reported % of COP	Calc'd % of COP	Mass (kg)	Manufacturer	Space Mission	Operational time	Author	Year
	pulse tube	1	10.0	95	156.5	290	15.65		14.0	13.1					Dang	2012
	pulse tube	1	4.1	60	180.0	300	44.33			9.0					Dang	2012
RDK415D	GM	1	35.0	50		300					7.50	Janis		10,000 hours	Wang	2012
		2	1.5	4												
	pulse tube		18.3	30	3850.0		210.38									
	pulse tube	1	1.2	80	42.0	300	35.00	35.00		7.9	0.90	Northrop			Nguyen	2011
	coaxial	1	6.5	67	165.0	300	25.38	25.00		13.7	5.00	Northrop	JAMI,		Nguyen	2011

Appendix B: Thermal testing data

Temperature measurements at x = L/2

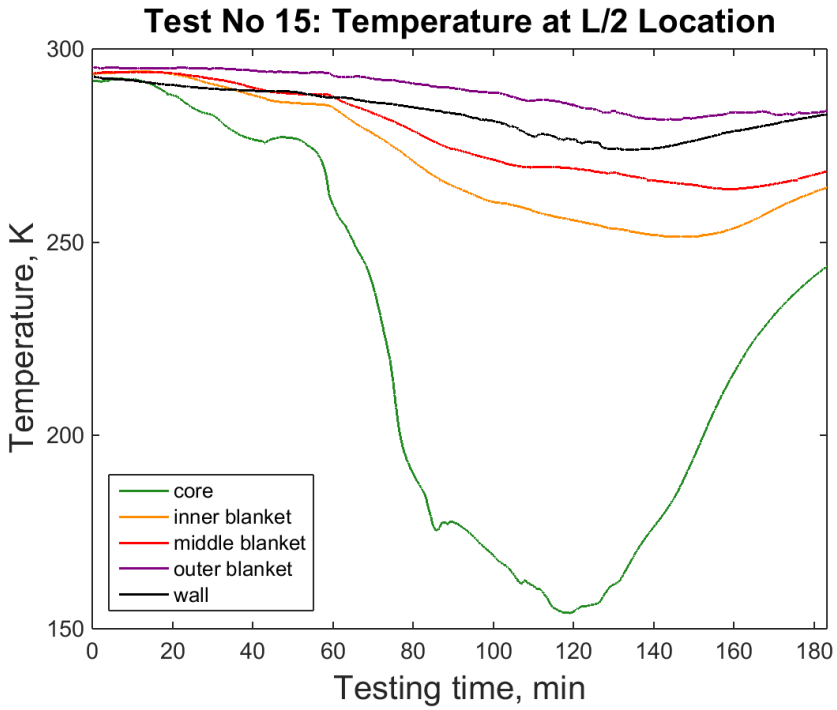

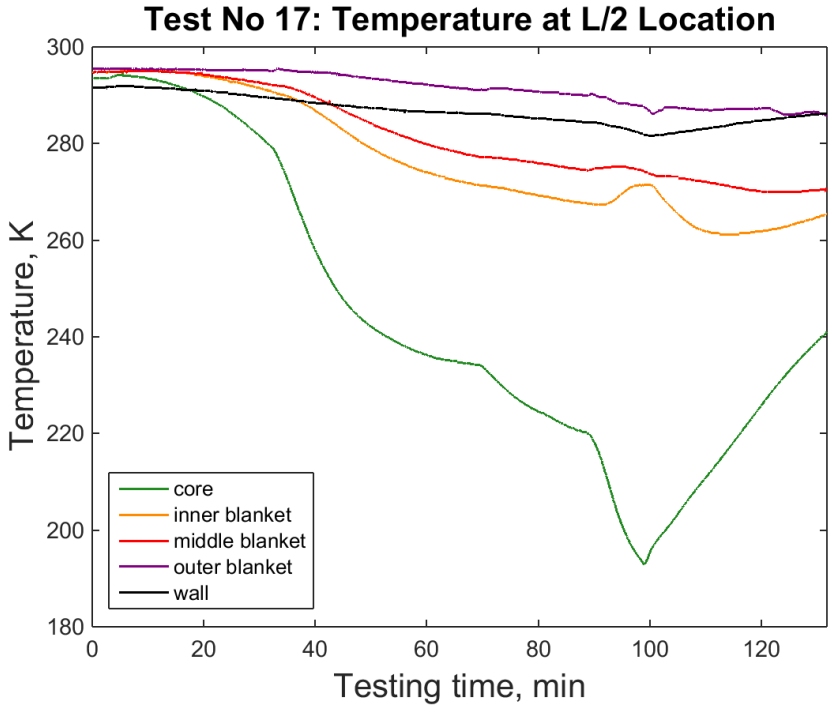

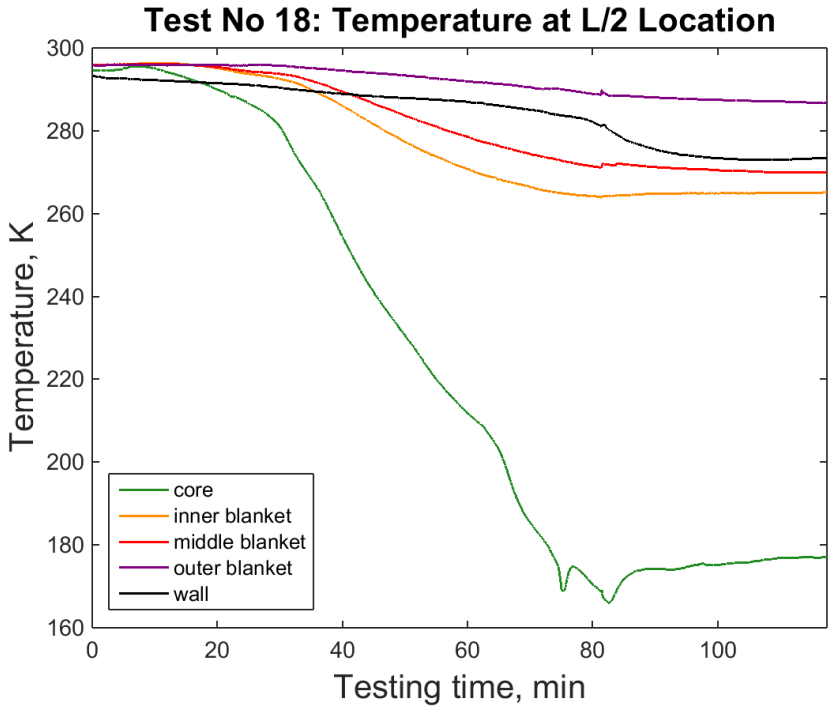
Test No 18: Temperature at L/2 Location
Temperature, K
Testing time, min
core
inner blanket
middle blanket
outer blanket
wall

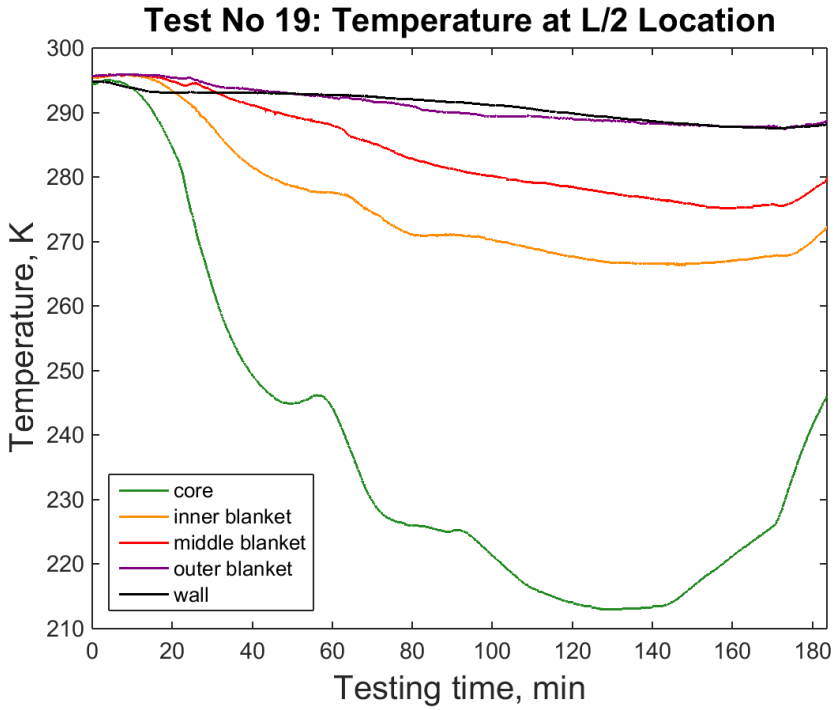
Test No 19: Temperature at L/2 Location
Temperature, K
Testing time, min
core
inner blanket
middle blanket
outer blanket
wall

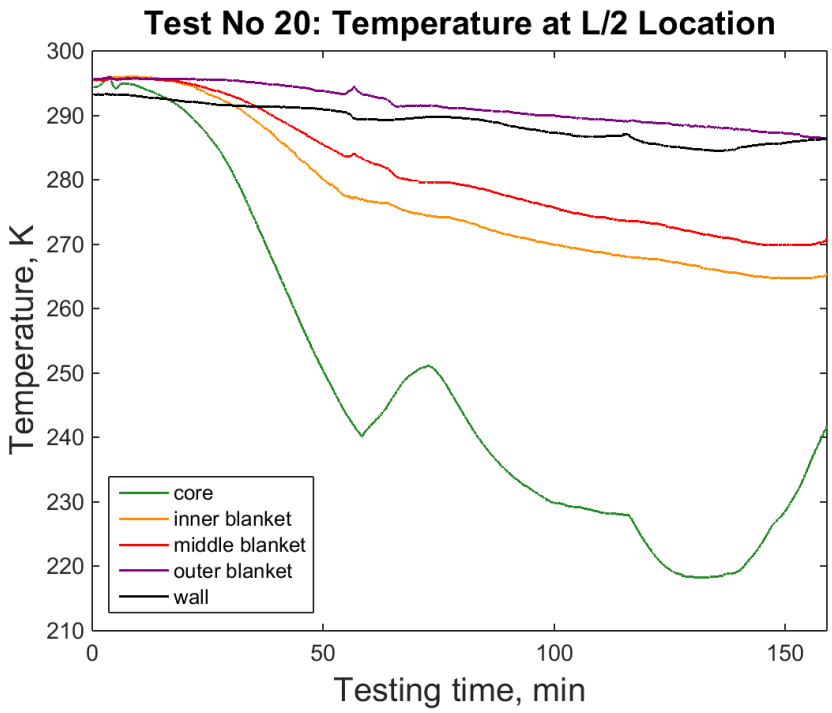
Test No 20: Temperature at L/2 Location
Temperature, K
Testing time, min
300
290
280
270
260
250
240
230
220
210
0
50
100
150
core
inner blanket
middle blanket
outer blanket
wall

Vacuum chamber pressure measurements

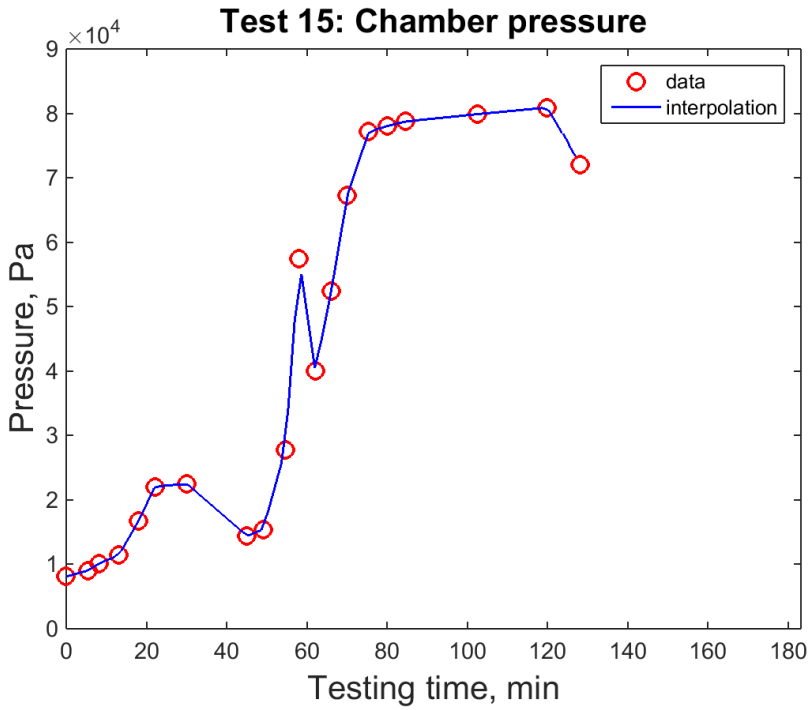

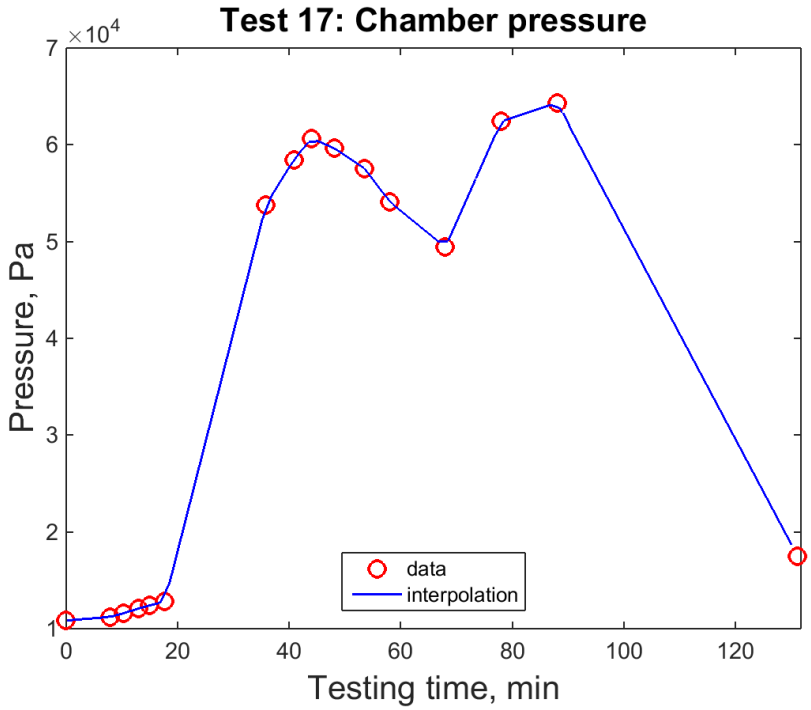

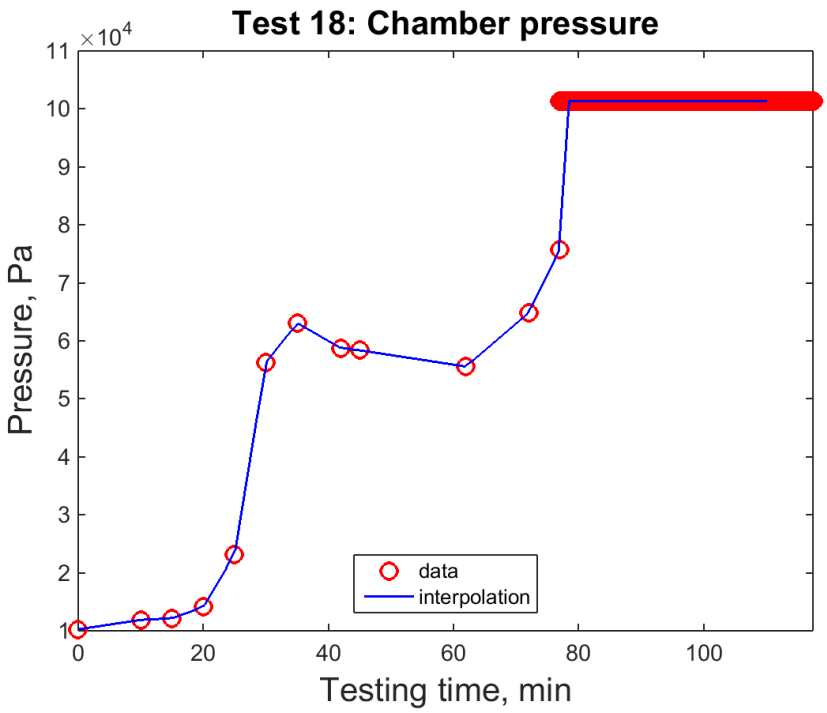
Test 18: Chamber pressure
×10^4
Pressure, Pa
Testing time, min
data
interpolation

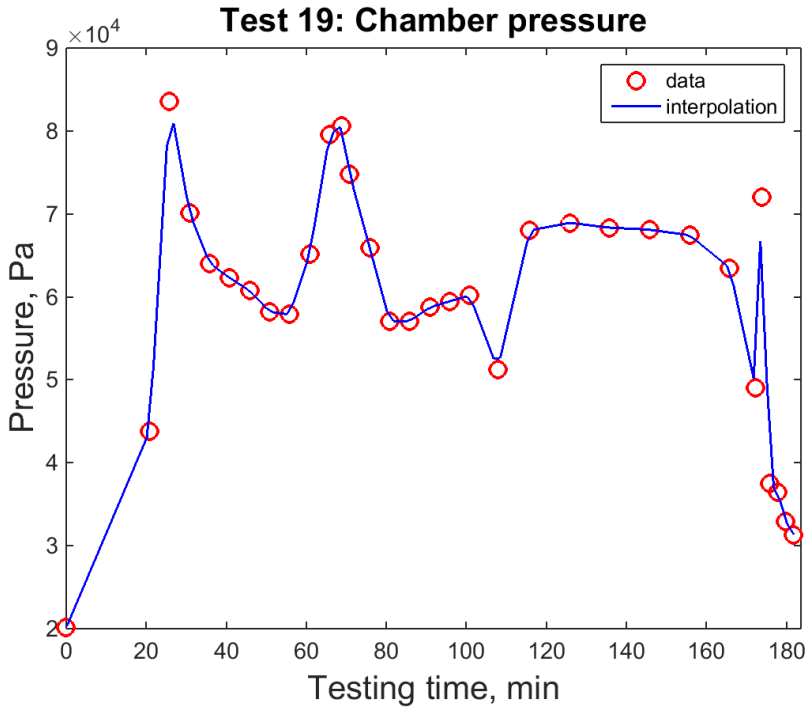
Test 19: Chamber pressure
×10^4
Pressure, Pa
Testing time, min
data
interpolation

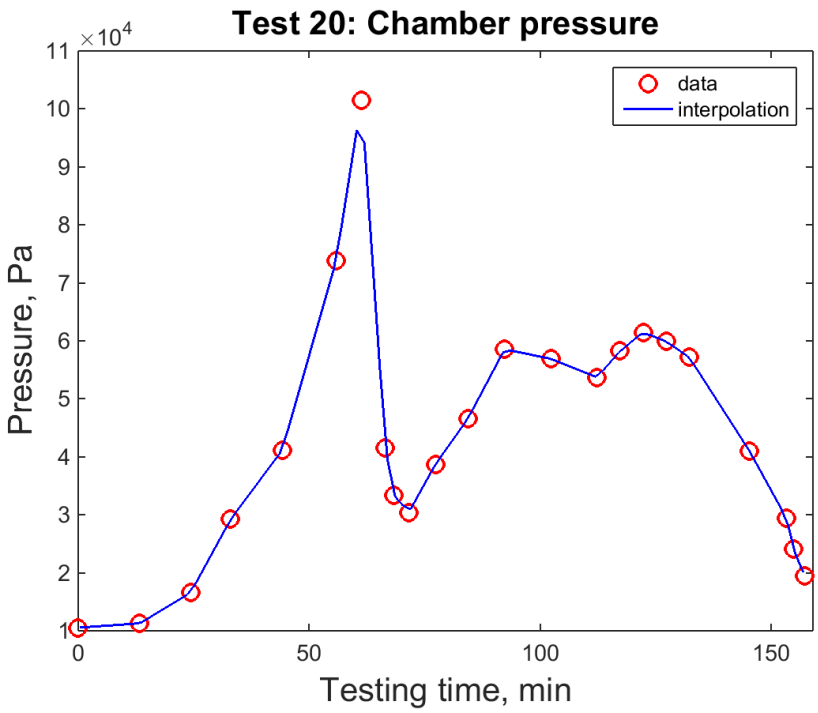
Test 20: Chamber pressure
×10^4
11
10
9
8
7
6
5
4
3
2
1
Pressure, Pa
0
50
100
150
Testing time, min
data
interpolation

Volumetric flow rate measurements

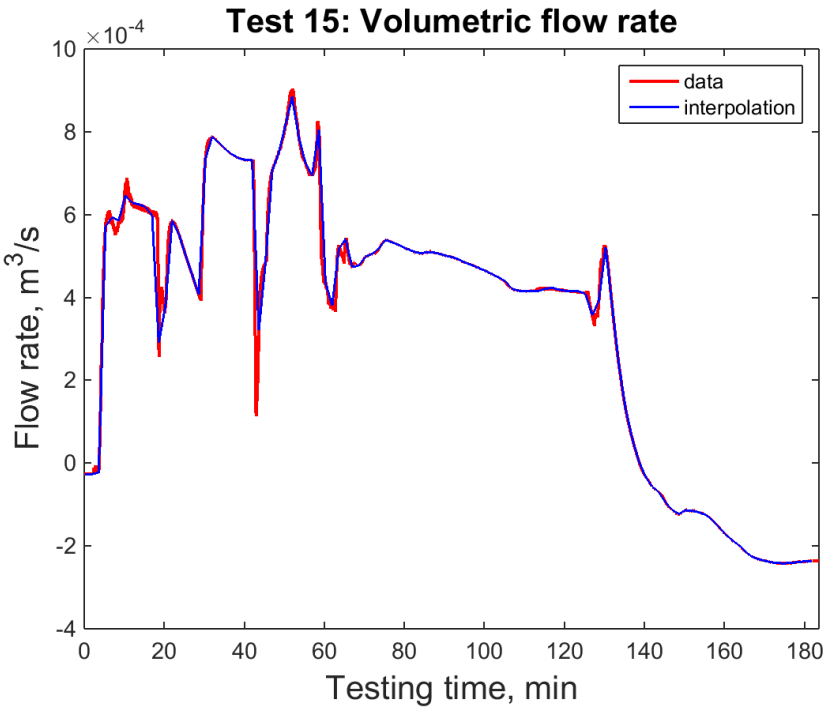

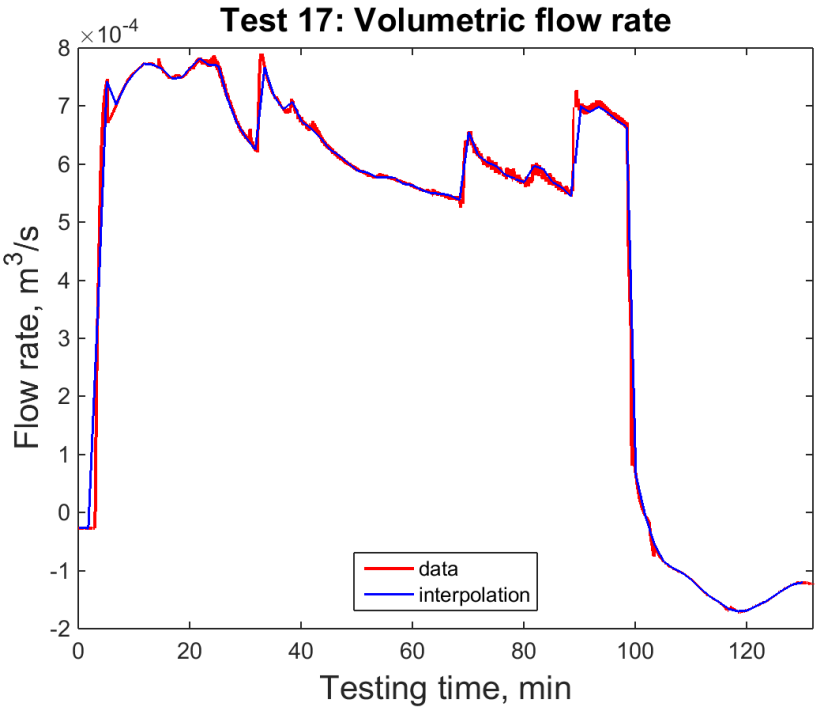

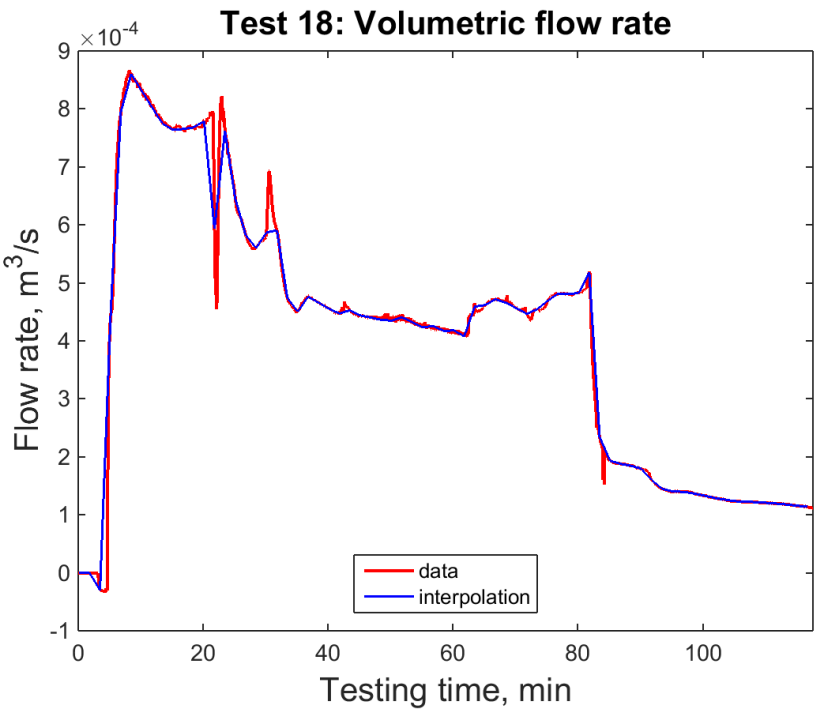
Test 18: Volumetric flow rate
×10^-4
Flow rate, m^3/s
Testing time, min
data
interpolation

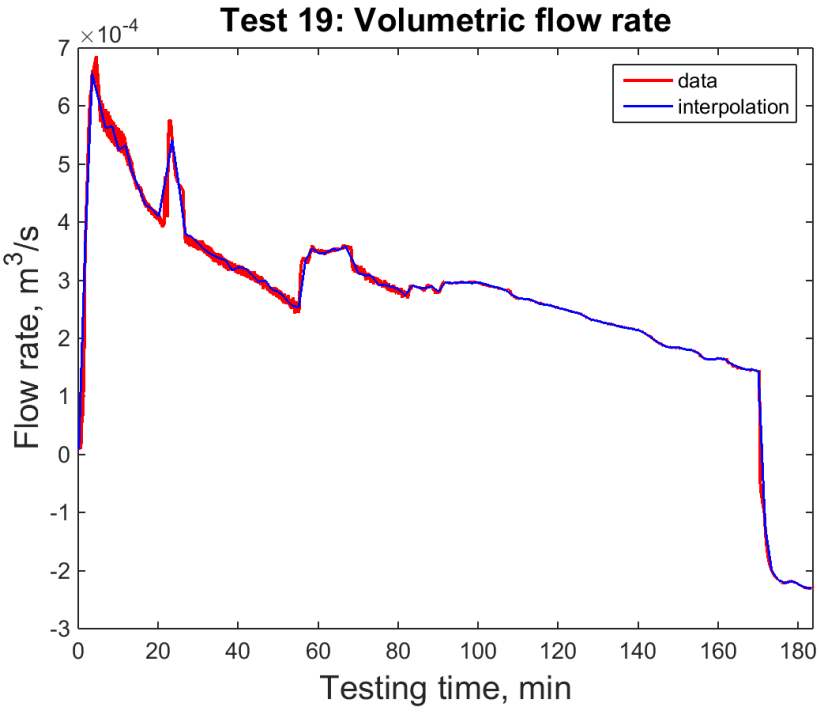
Test 19: Volumetric flow rate
×10^-4
Flow rate, m^3/s
Testing time, min
data
interpolation

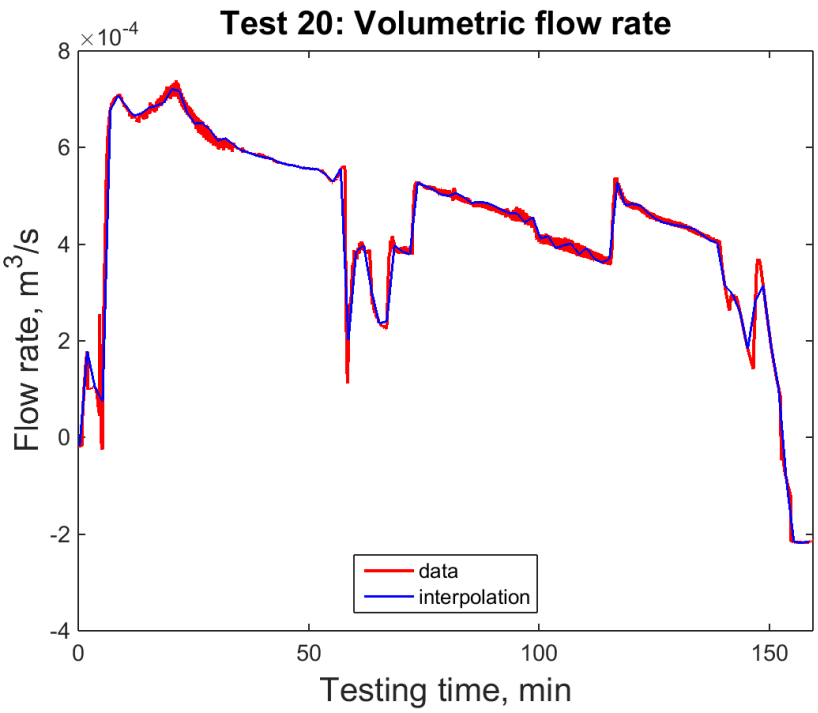
Test 20: Volumetric flow rate
×10^-4
8
6
4
2
0
-2
-4
Flow rate, m^3/s
0
50
100
150
Testing time, min
data
interpolation

Appendix C: Thermal model results

Recreation of temperature profile at x = L/2

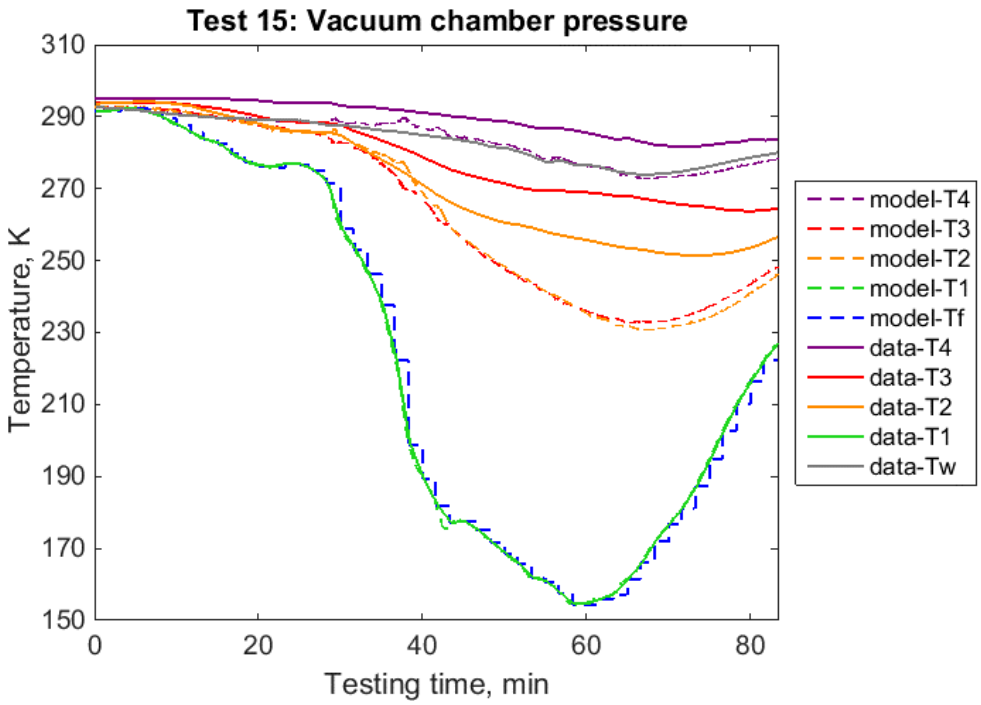

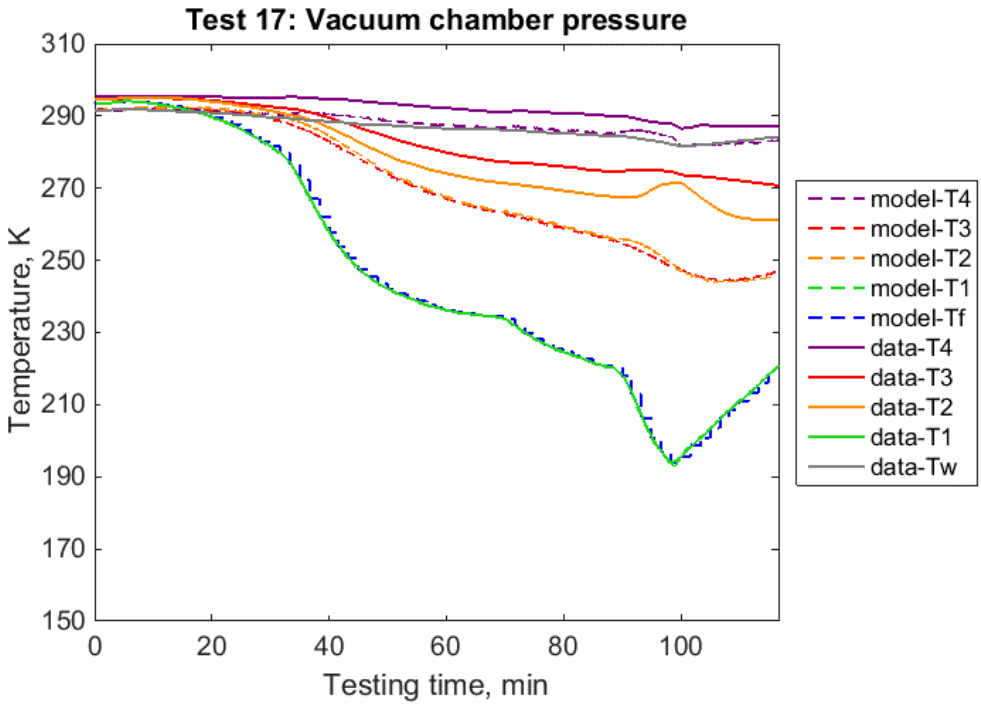

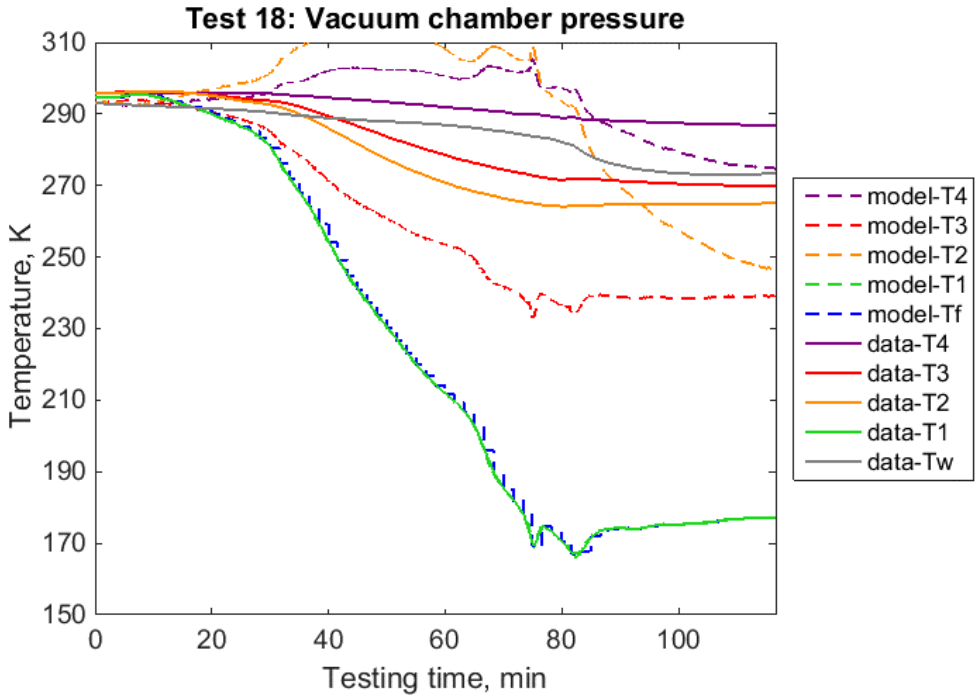
Test 18: Vacuum chamber pressure
Temperature, K
Testing time, min
310
290
270
250
230
210
190
170
150
0
20
40
60
80
100
model-T4
model-T3
model-T2
model-T1
model-Tf
data-T4
data-T3
data-T2
data-T1
data-Tw

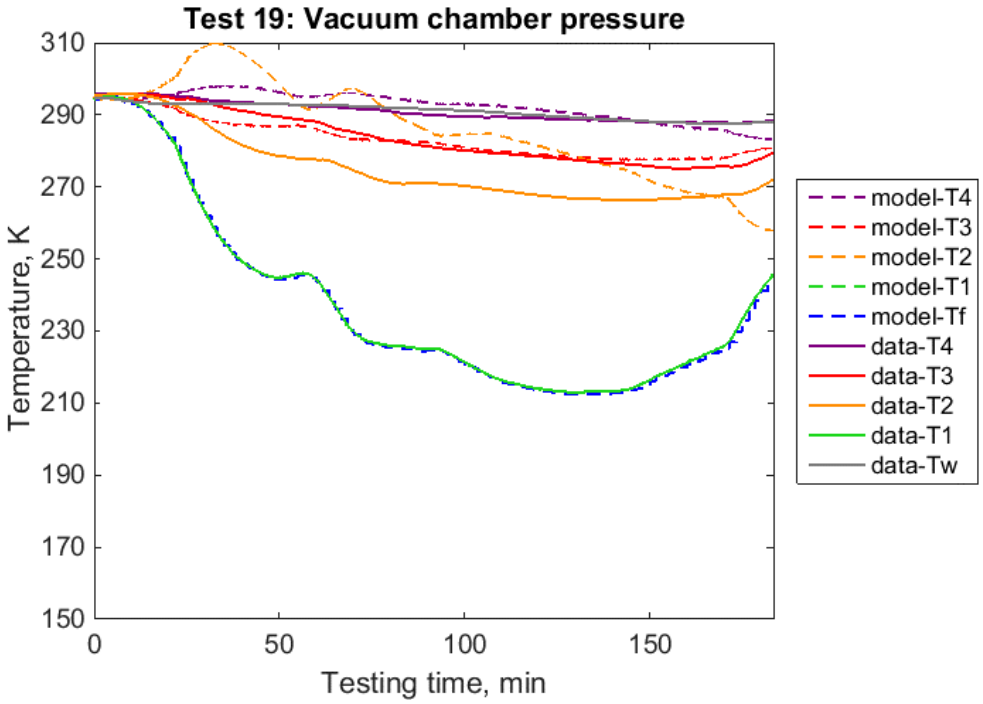
Test 19: Vacuum chamber pressure
Temperature, K
Testing time, min
310
290
270
250
230
210
190
170
150
0
50
100
150
model-T4
model-T3
model-T2
model-T1
model-Tf
data-T4
data-T3
data-T2
data-T1
data-Tw

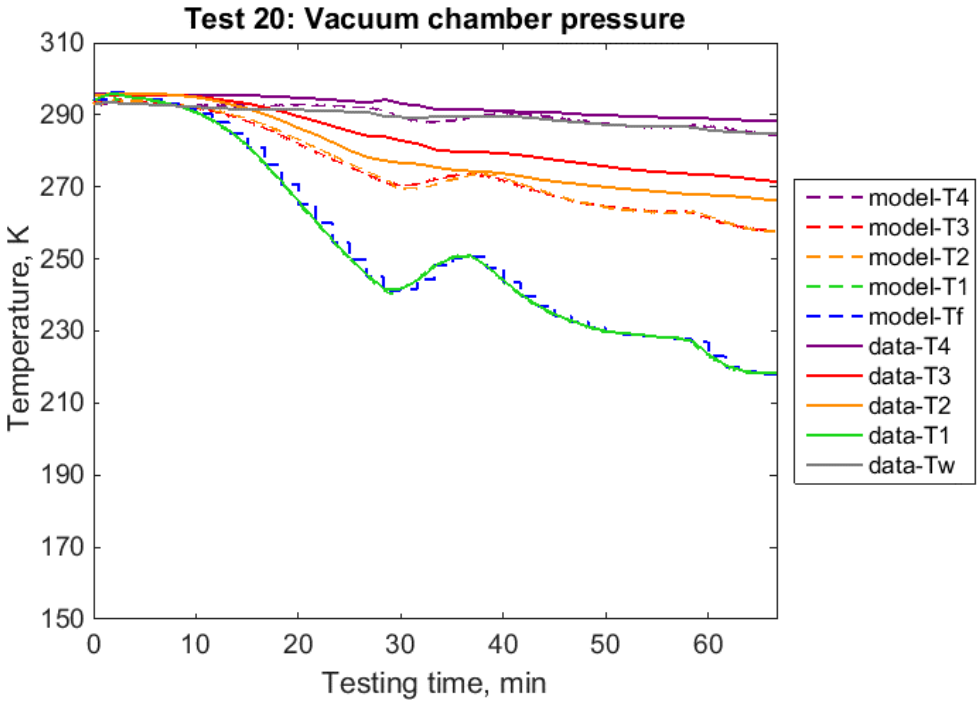
Test 20: Vacuum chamber pressure
Temperature, K
Testing time, min
310
290
270
250
230
210
190
170
150
0
10
20
30
40
50
60
model-T4
model-T3
model-T2
model-T1
model-Tf
data-T4
data-T3
data-T2
data-T1
data-Tw

Comparison of modes of heat transfer

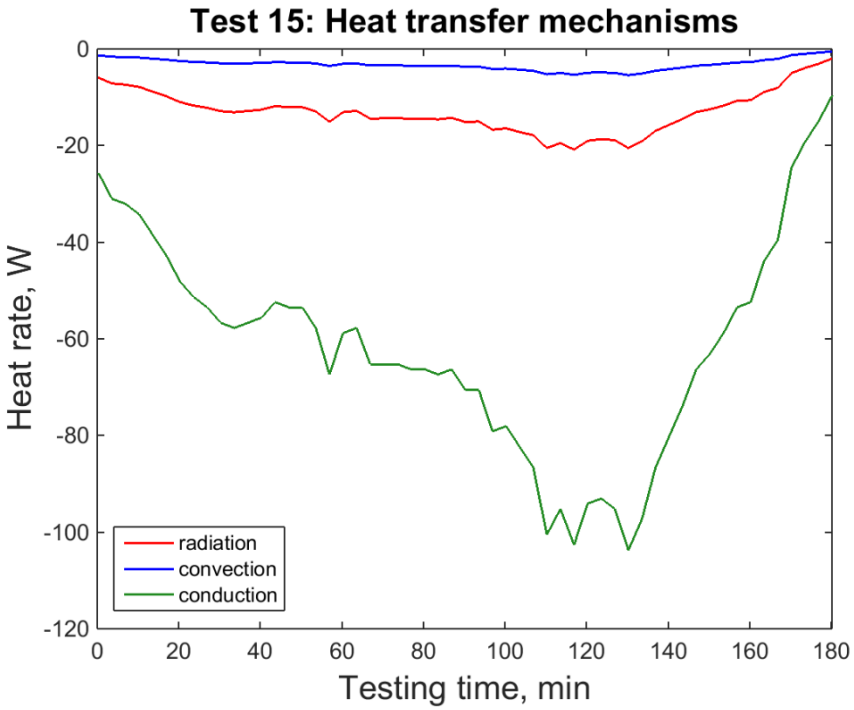

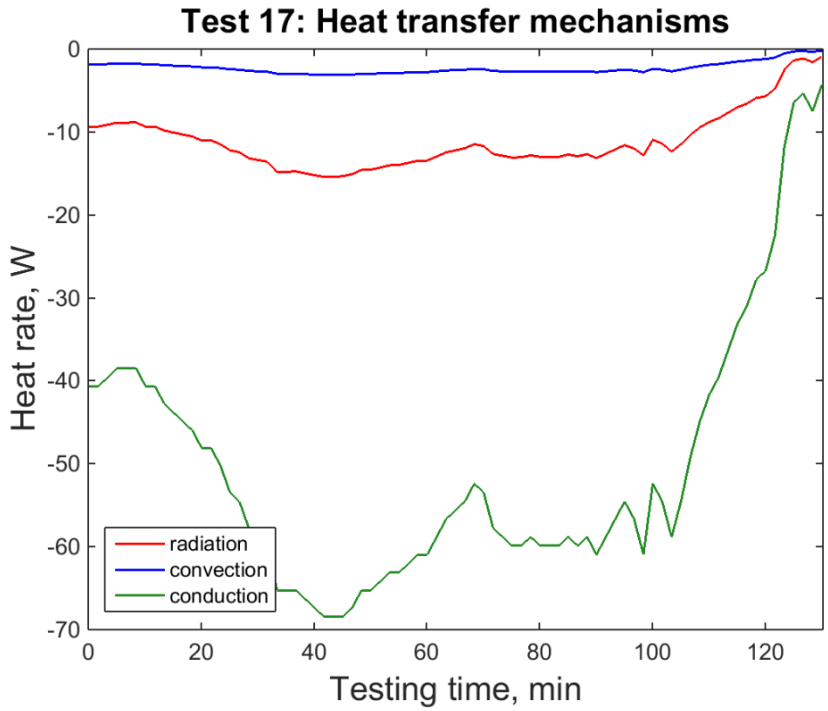

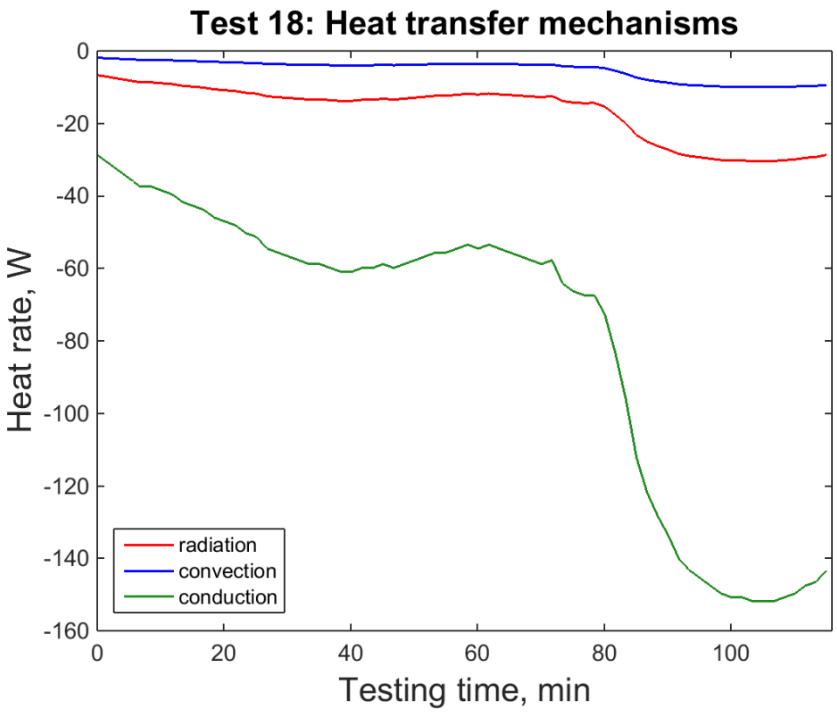
Test 18: Heat transfer mechanisms
Heat rate, W
Testing time, min
radiation
convection
conduction
0
-20
-40
-60
-80
-100
-120
-140
-160
0
20
40
60
80
100

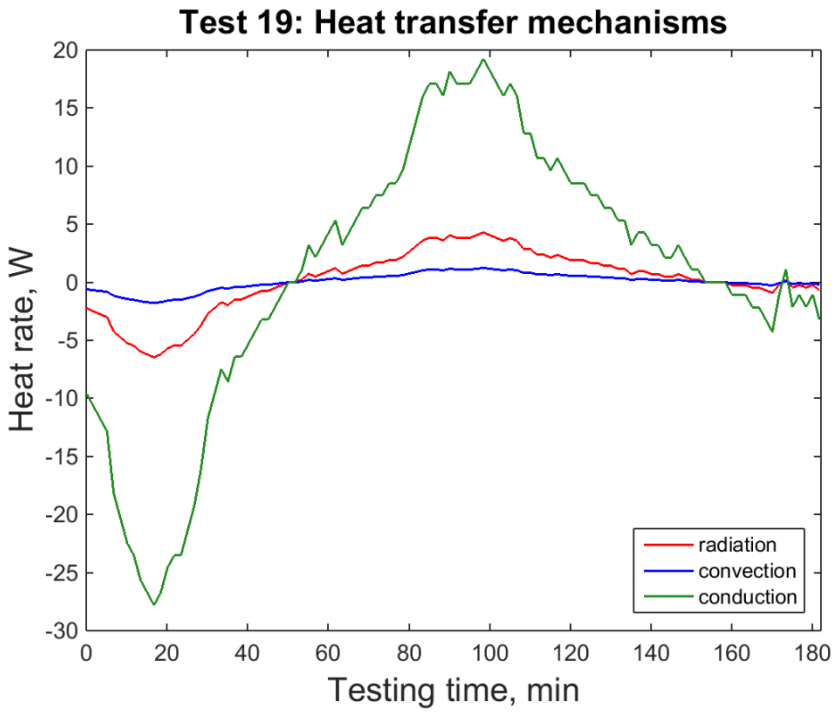
Test 19: Heat transfer mechanisms
Heat rate, W
Testing time, min
radiation
convection
conduction
20
15
10
5
0
-5
-10
-15
-20
-25
-30
0
20
40
60
80
100
120
140
160
180

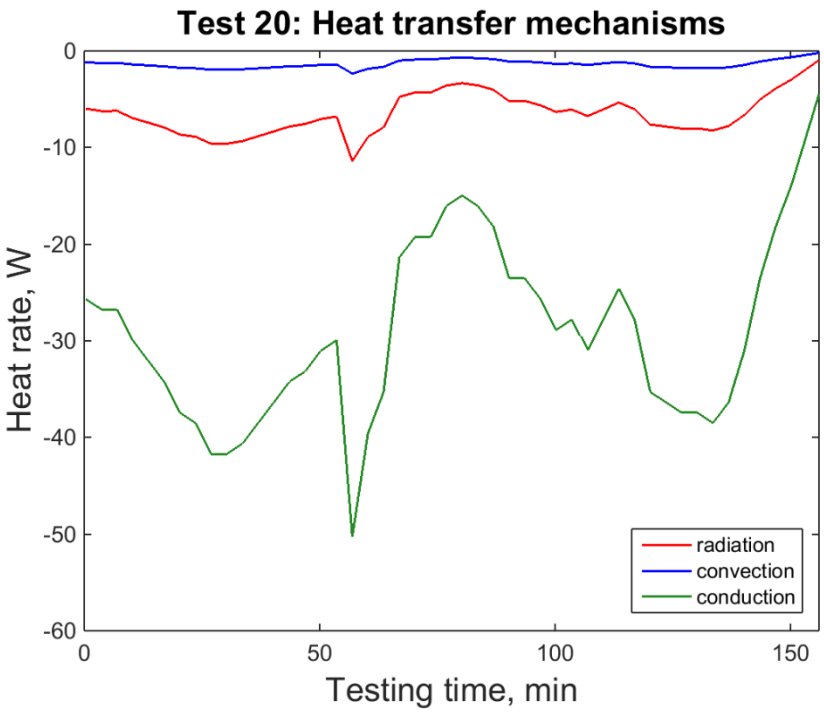
Test 20: Heat transfer mechanisms
Heat rate, W
Testing time, min
0
-10
-20
-30
-40
-50
-60
0
50
100
150
radiation
convection
conduction

Appendix D: Deployment test data

All recorded markers compared with tracked markers

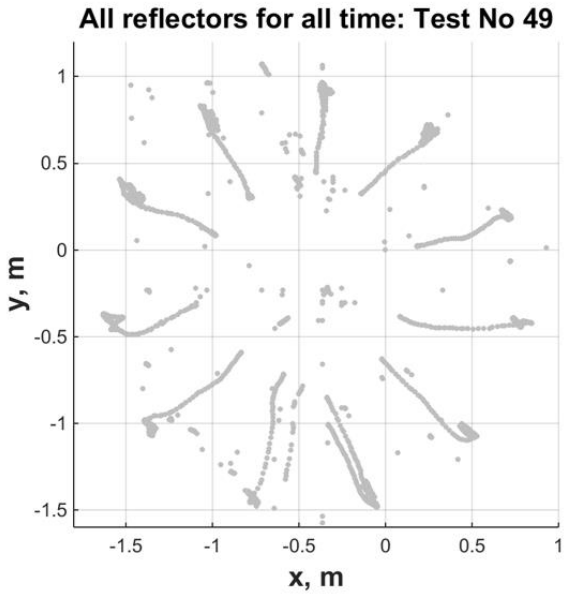

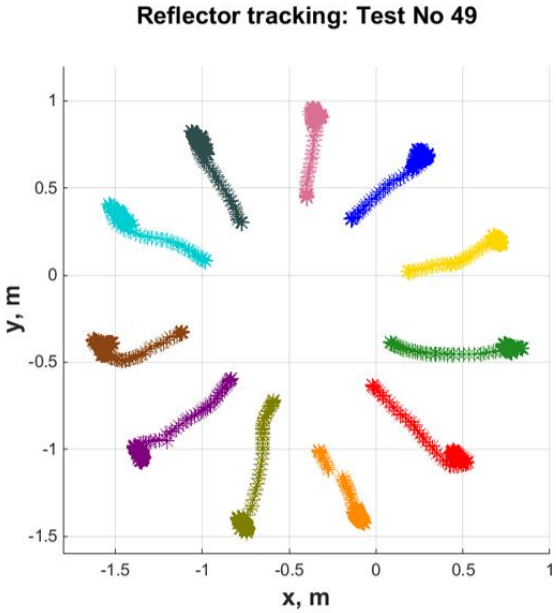

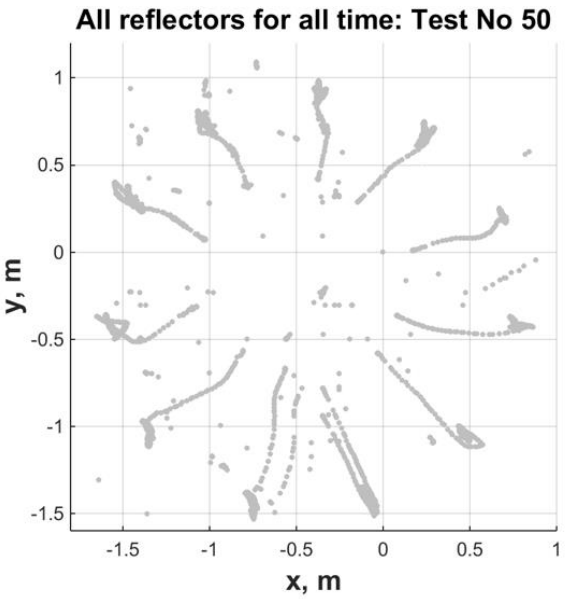

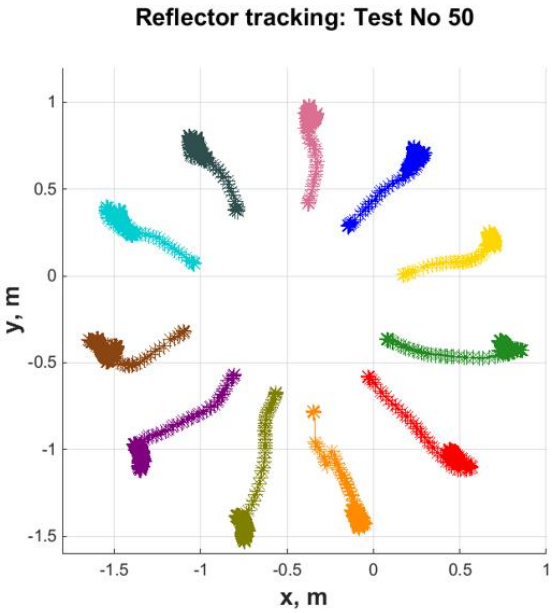

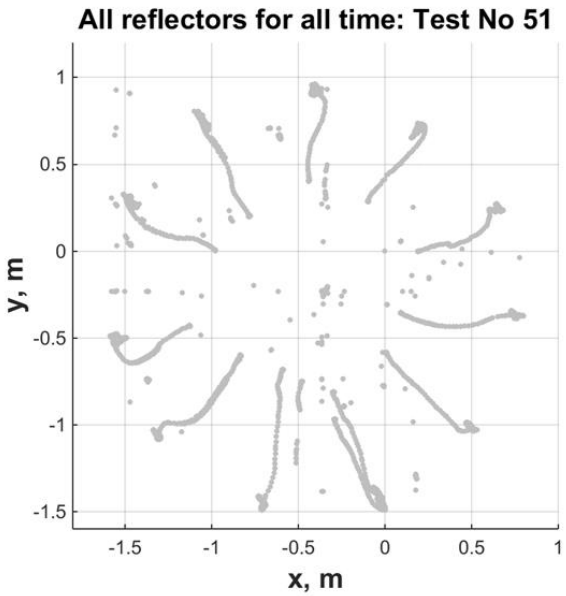
All reflectors for all time: Test No 51
y, m
x, m
1
0.5
0
-0.5
-1
-1.5
-1.5
-1
-0.5
0
0.5
1

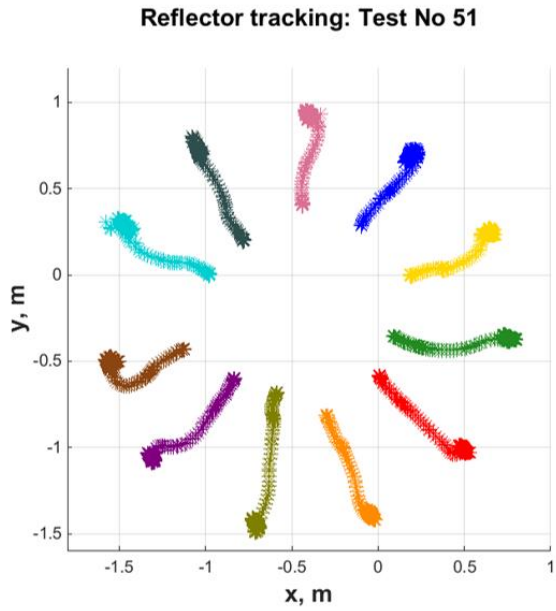
Reflector tracking: Test No 51
y, m
x, m
1
0.5
0
-0.5
-1
-1.5
-1.5
-1
-0.5
0
0.5
1

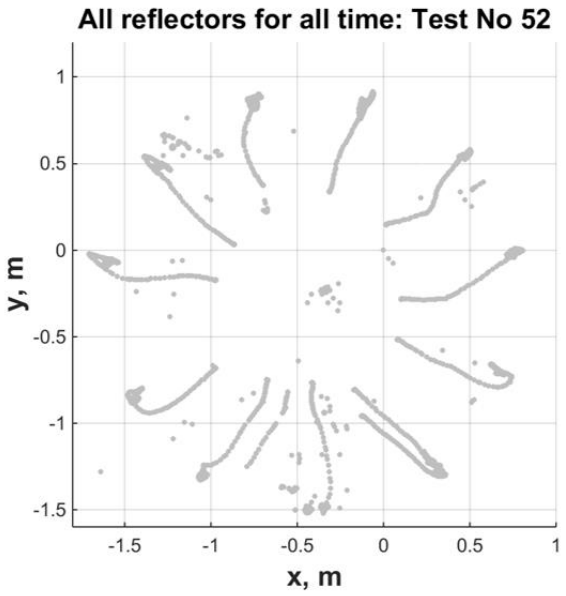
All reflectors for all time: Test No 52
y, m
x, m
1
0.5
0
-0.5
-1
-1.5
-1.5
-1
-0.5
0
0.5
1

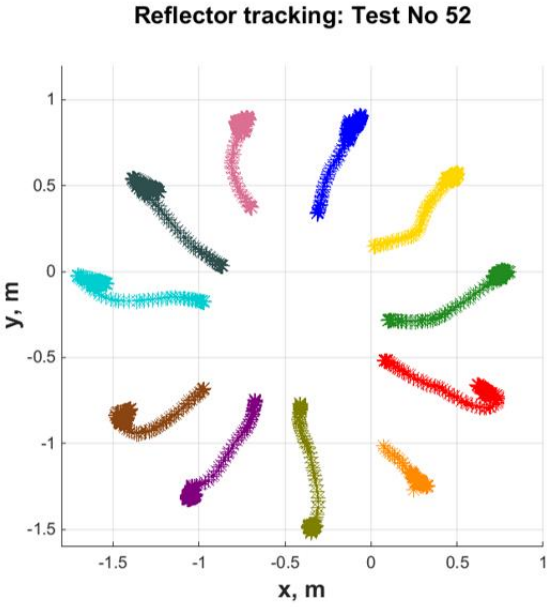
Reflector tracking: Test No 52
y, m
x, m
1
0.5
0
-0.5
-1
-1.5
-1.5
-1
-0.5
0
0.5
1

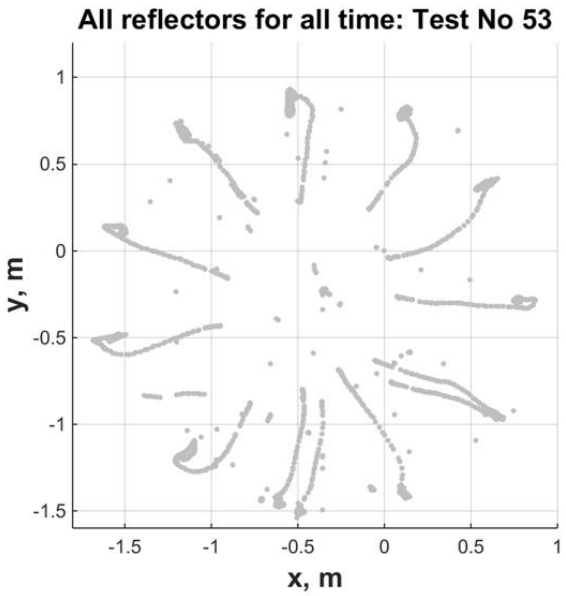
All reflectors for all time: Test No 53
y, m
x, m
1
0.5
0
-0.5
-1
-1.5
-1.5
-1
-0.5
0
0.5
1

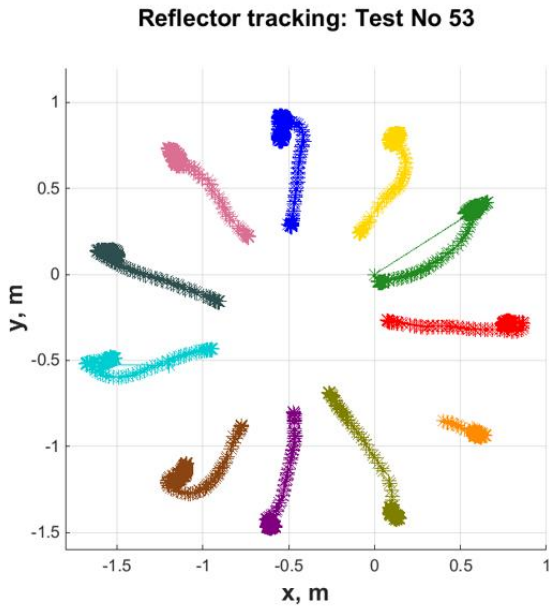
Reflector tracking: Test No 53
y, m
x, m
1
0.5
0
-0.5
-1
-1.5
-1.5
-1
-0.5
0
0.5
1

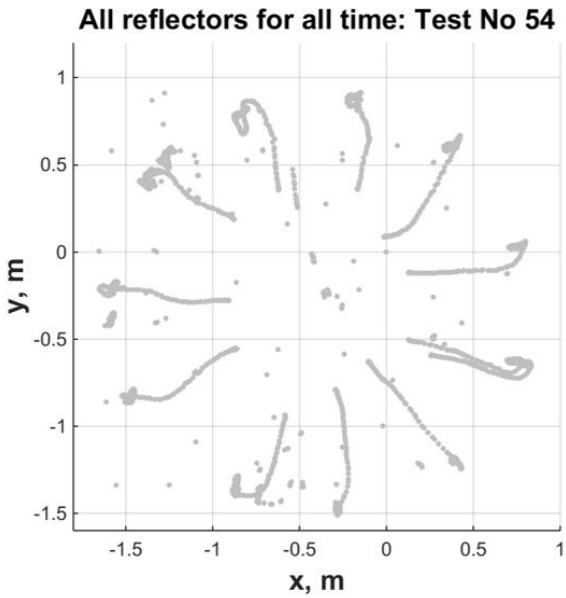
All reflectors for all time: Test No 54
y, m
x, m
1
0.5
0
-0.5
-1
-1.5
-1.5
-1
-0.5
0
0.5
1

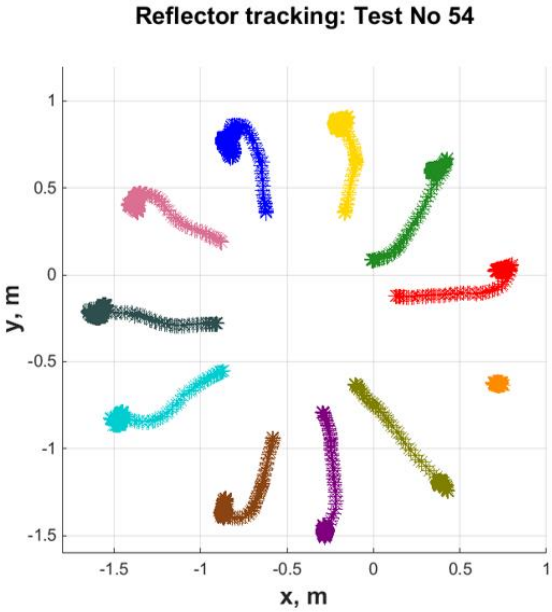
Reflector tracking: Test No 54
y, m
x, m
1
0.5
0
-0.5
-1
-1.5
-1.5
-1
-0.5
0
0.5
1

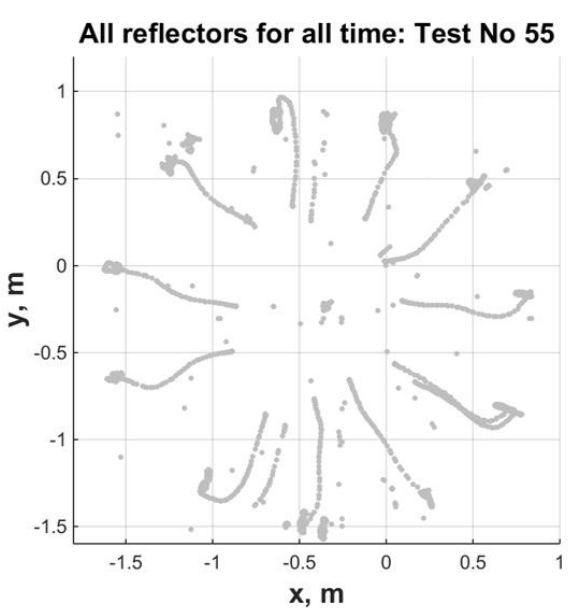
All reflectors for all time: Test No 55
y, m
x, m
1
0.5
0
-0.5
-1
-1.5
-1.5
-1
-0.5
0
0.5
1

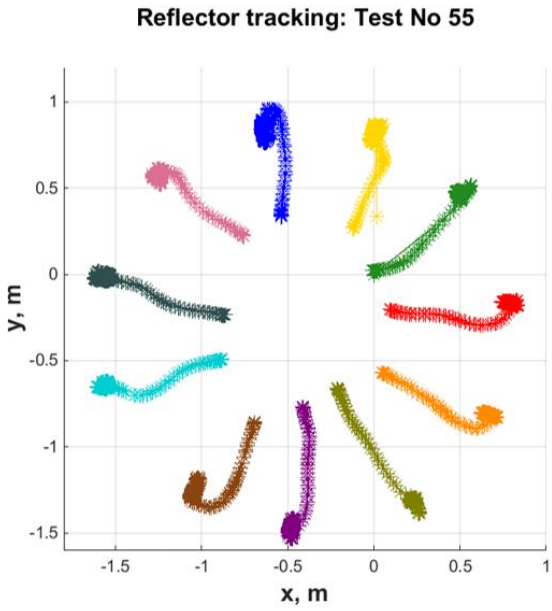
Reflector tracking: Test No 55
y, m
x, m
1
0.5
0
-0.5
-1
-1.5
-1.5
-1
-0.5
0
0.5
1

Radial speed and acceleration of point masses

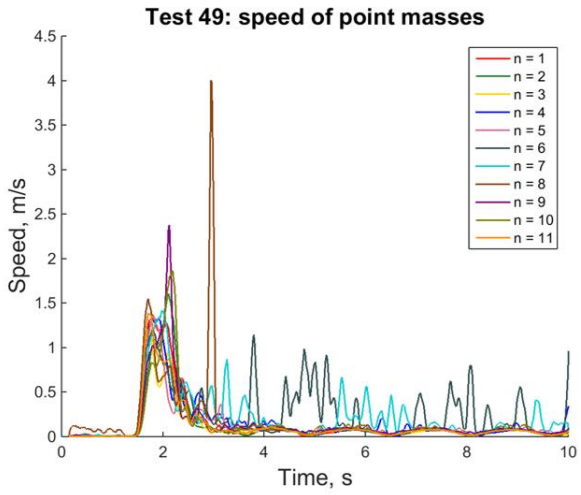

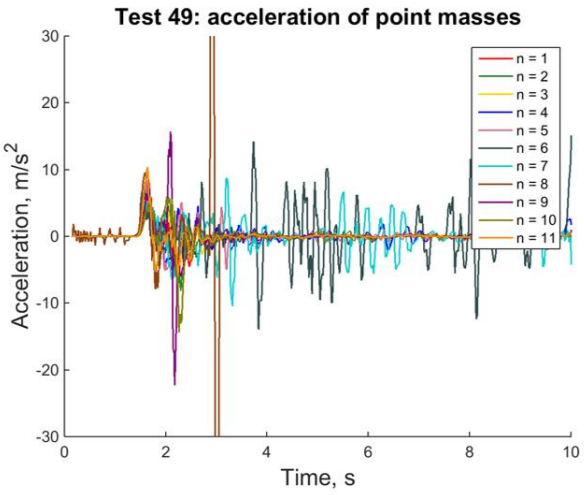

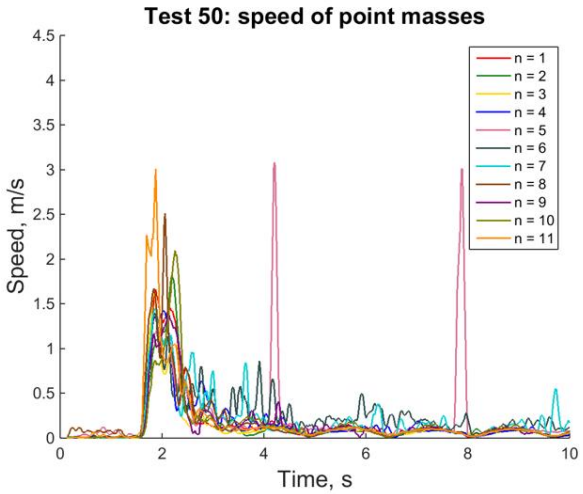

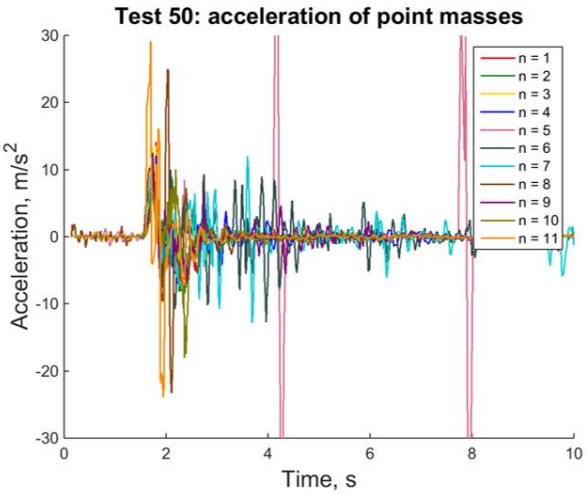

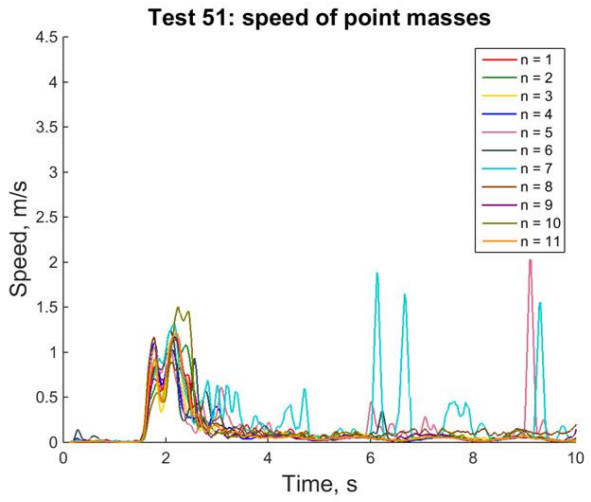
Test 51: speed of point masses
Speed, m/s
Time, s
n = 1
n = 2
n = 3
n = 4
n = 5
n = 6
n = 7
n = 8
n = 9
n = 10
n = 11

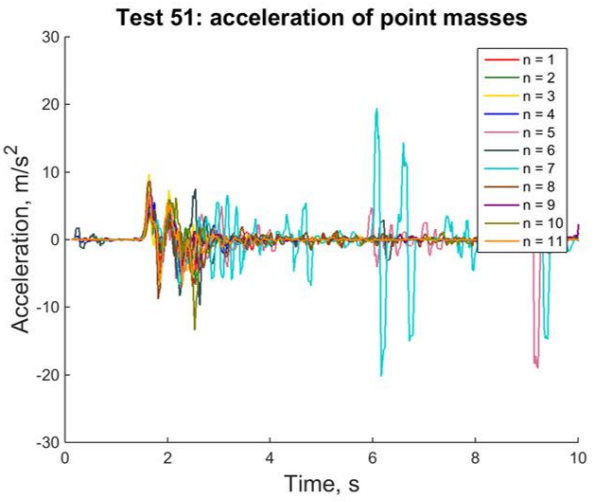
Test 51: acceleration of point masses
Acceleration, m/s2
Time, s
n = 1
n = 2
n = 3
n = 4
n = 5
n = 6
n = 7
n = 8
n = 9
n = 10
n = 11

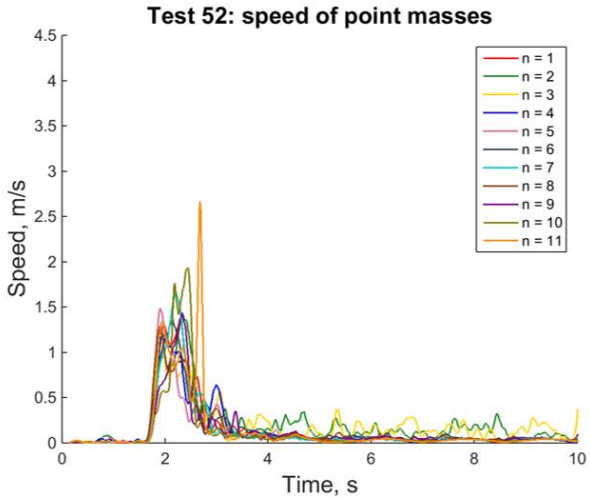
Test 52: speed of point masses
Speed, m/s
Time, s
n = 1
n = 2
n = 3
n = 4
n = 5
n = 6
n = 7
n = 8
n = 9
n = 10
n = 11

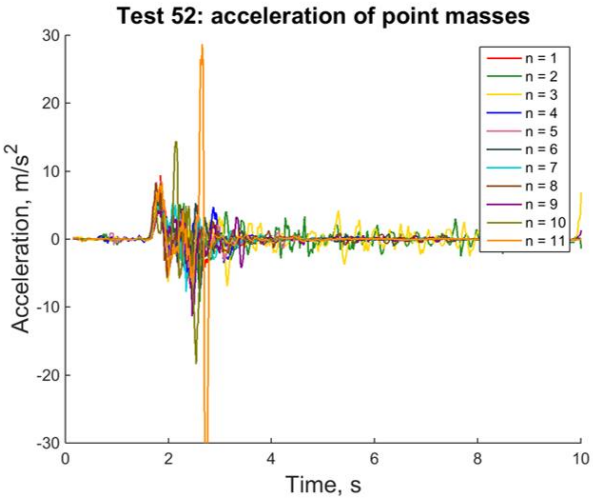
Test 52: acceleration of point masses
Acceleration, m/s2
Time, s
n = 1
n = 2
n = 3
n = 4
n = 5
n = 6
n = 7
n = 8
n = 9
n = 10
n = 11

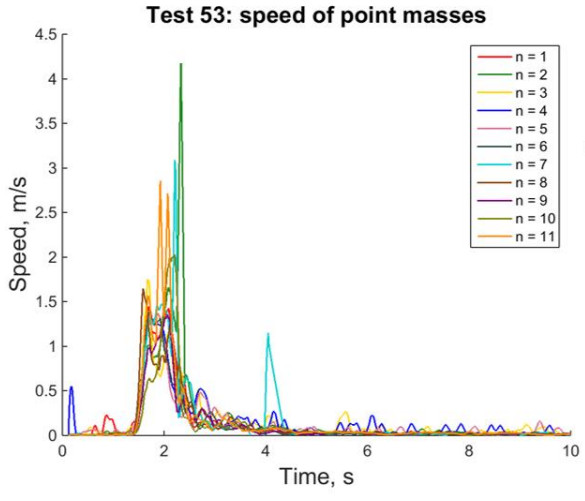
Test 53: speed of point masses
Speed, m/s
Time, s
n = 1
n = 2
n = 3
n = 4
n = 5
n = 6
n = 7
n = 8
n = 9
n = 10
n = 11

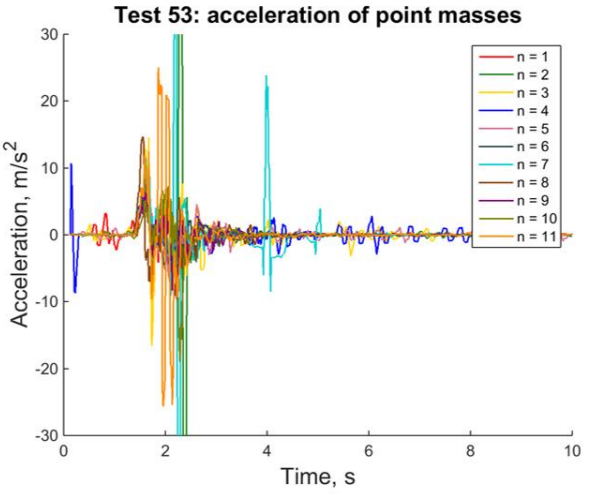
Test 53: acceleration of point masses
Acceleration, m/s2
Time, s
n = 1
n = 2
n = 3
n = 4
n = 5
n = 6
n = 7
n = 8
n = 9
n = 10
n = 11

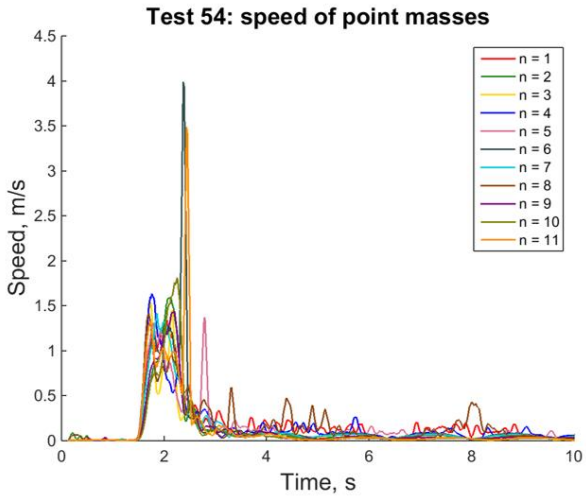
Test 54: speed of point masses
Speed, m/s
Time, s
n = 1
n = 2
n = 3
n = 4
n = 5
n = 6
n = 7
n = 8
n = 9
n = 10
n = 11

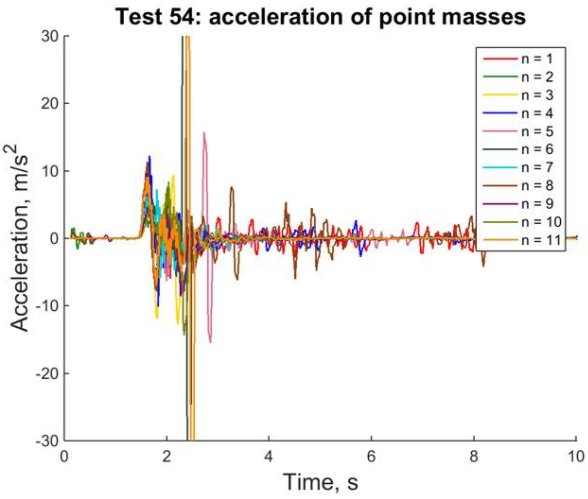
Test 54: acceleration of point masses
Acceleration, m/s2
Time, s
n = 1
n = 2
n = 3
n = 4
n = 5
n = 6
n = 7
n = 8
n = 9
n = 10
n = 11

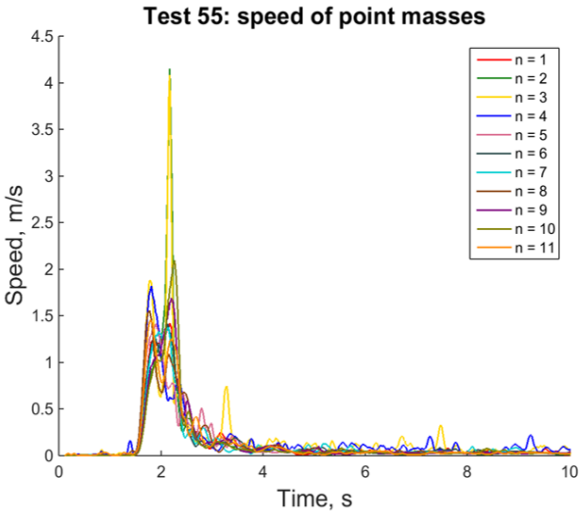
Test 55: speed of point masses
Speed, m/s
Time, s
n = 1
n = 2
n = 3
n = 4
n = 5
n = 6
n = 7
n = 8
n = 9
n = 10
n = 11

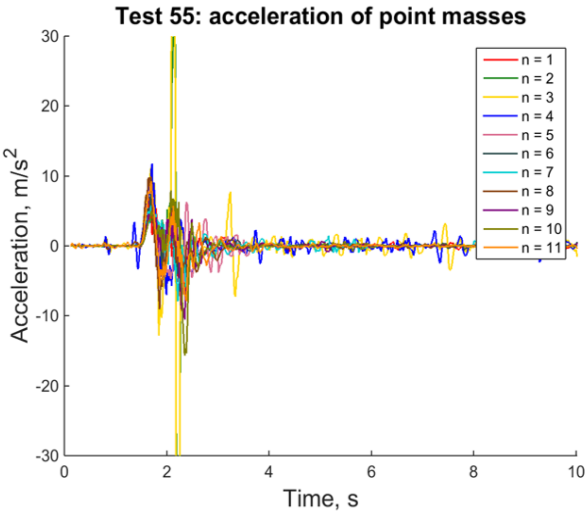
Test 55: acceleration of point masses
Acceleration, m/s2
Time, s
n = 1
n = 2
n = 3
n = 4
n = 5
n = 6
n = 7
n = 8
n = 9
n = 10
n = 11

Appendix E: Deployment model results

Test 49 data and model predictions

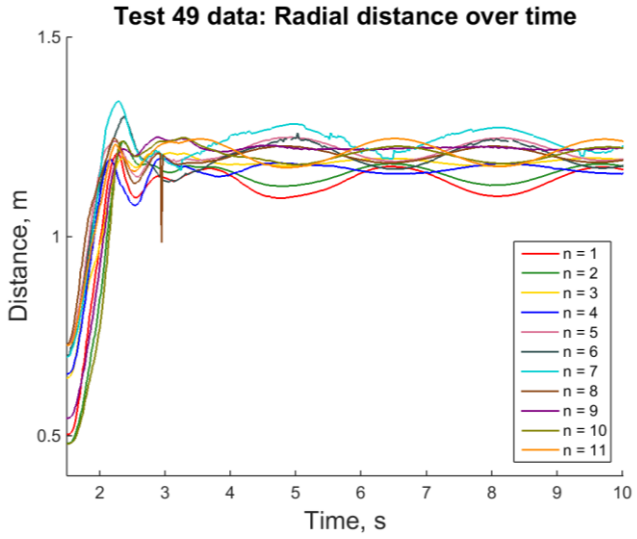

k = 6.9 N/m, c = 14 N-s/m

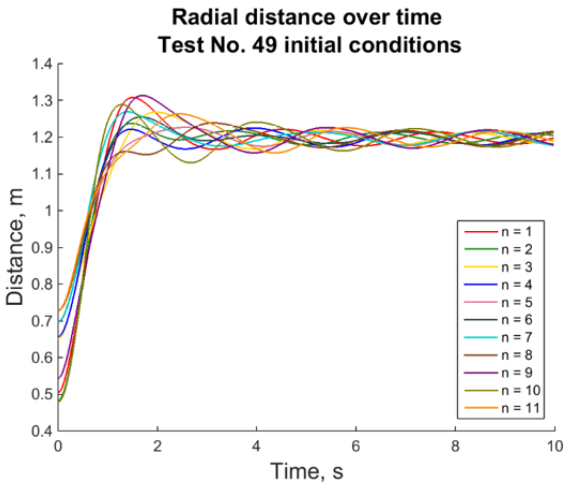

t < 1.5 s: k = 20 N/m, c = 15 N-s/m
t ≥ 1.5 s: k = 2 N/m, c = 5 N-s/m

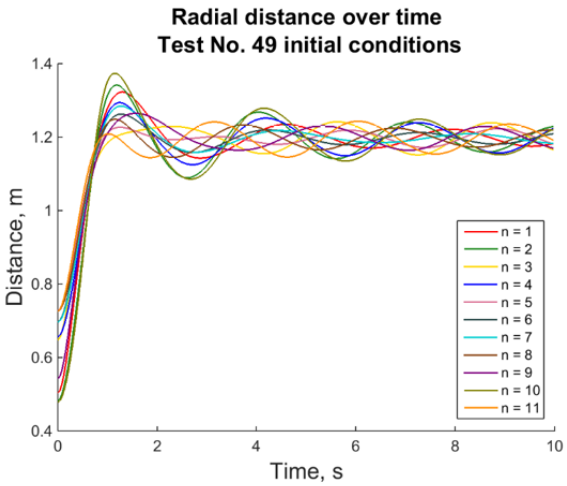

Test 50 data and model predictions

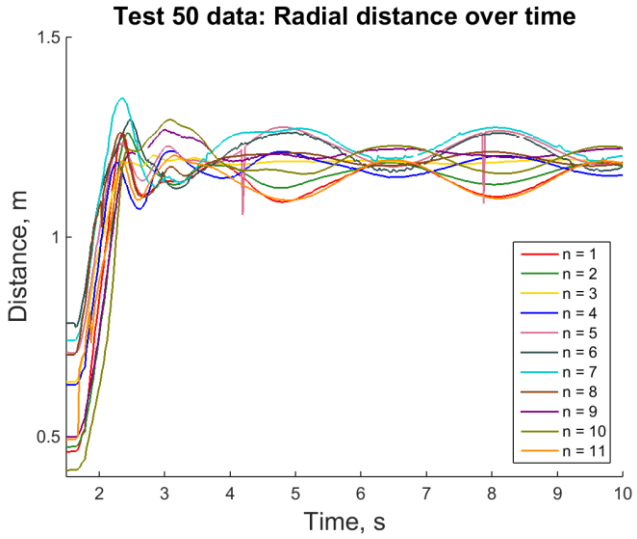

k = 6.9 N/m, c = 14 N-s/m

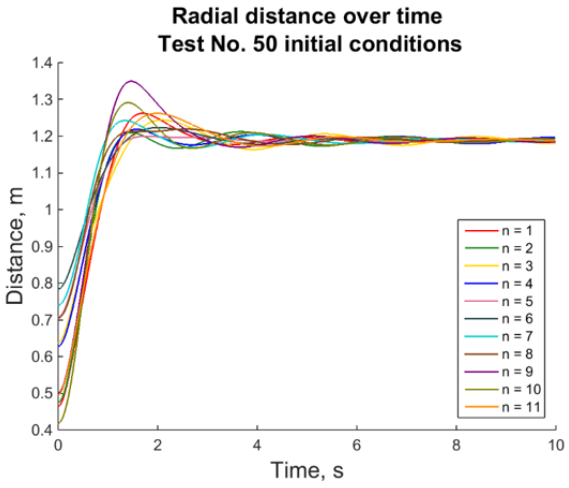

t < 1.5 s: k = 22 N/m, c = 15 N-s/m
t ≥ 1.5 s: k = 2 N/m, c = 4 N-s/m

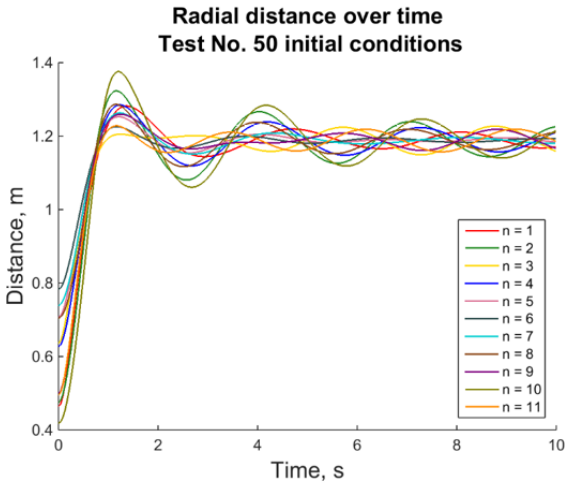

Test 51 data and model predictions

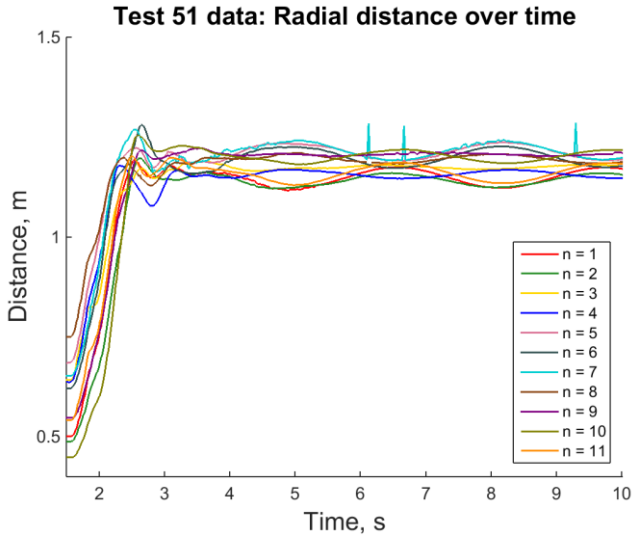

k = 6.9 N/m, c = 14 N-s/m

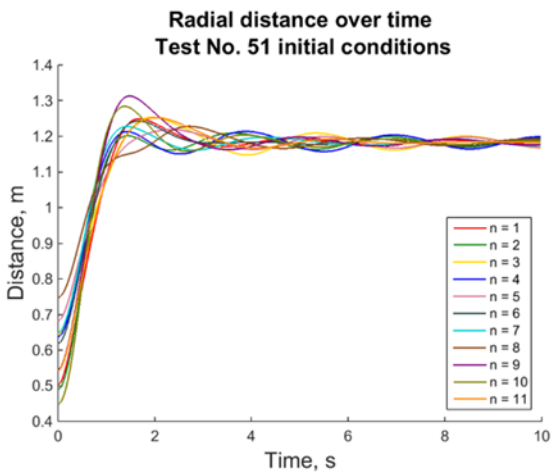

t < 1.5 s: k = 15 N/m, c = 15 N-s/m
t ≥ 1.5 s: k = 2 N/m, c = 4 N-s/m

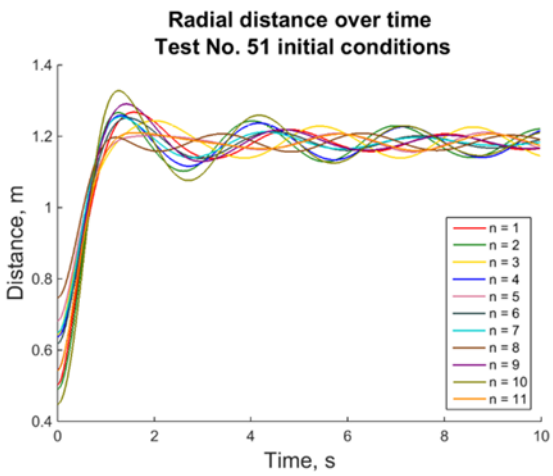

Test 52 data and model predictions

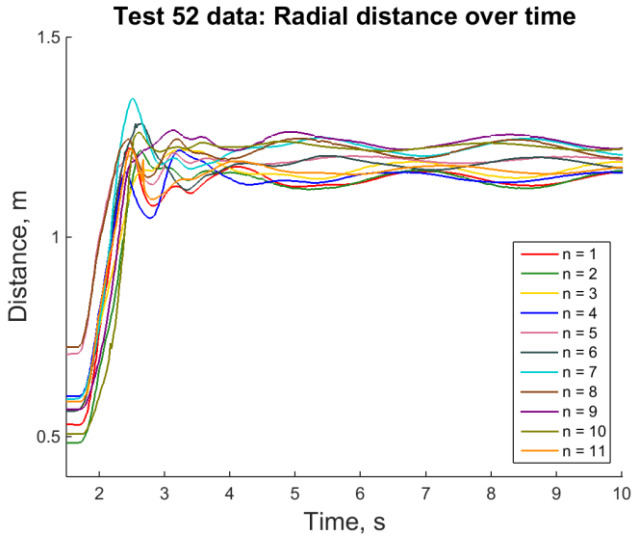

k = 6.9 N/m, c = 14 N-s/m

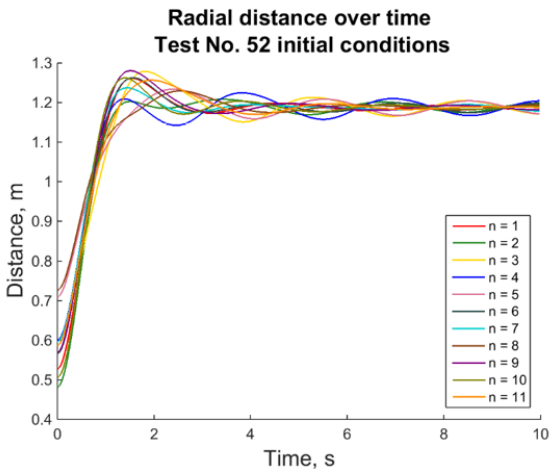

t < 1.5 s: k = 22 N/m, c = 15 N-s/m
t ≥ 1.5 s: k = 2 N/m, c = 3 N-s/m

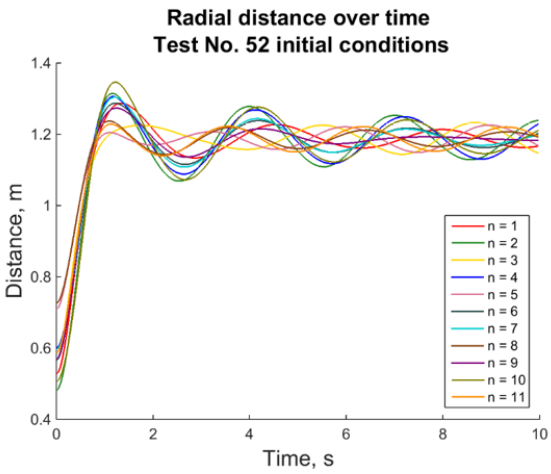

Test 53 data and model predictions

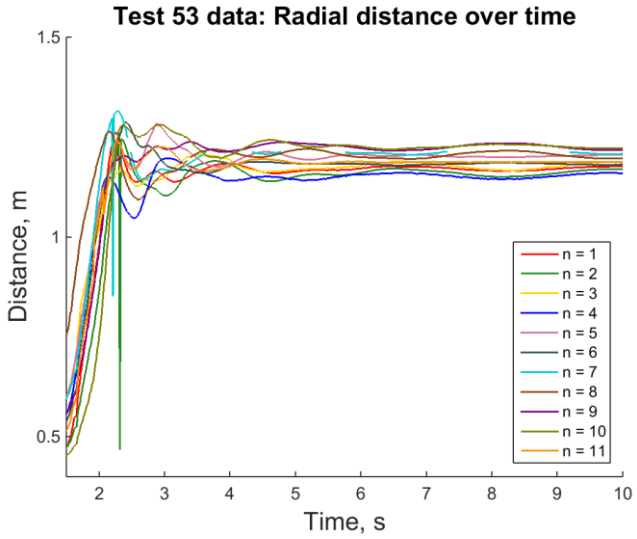

k = 6.9 N/m, c = 14 N-s/m

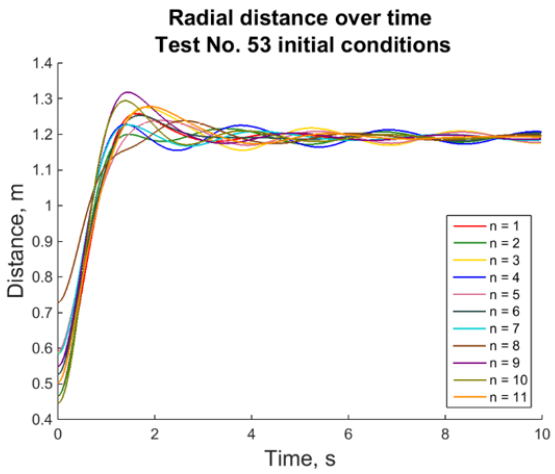

t < 1.5 s: k = 27 N/m, c = 20 N-s/m
t ≥ 1.5 s: k = 1 N/m, c = 20 N-s/m

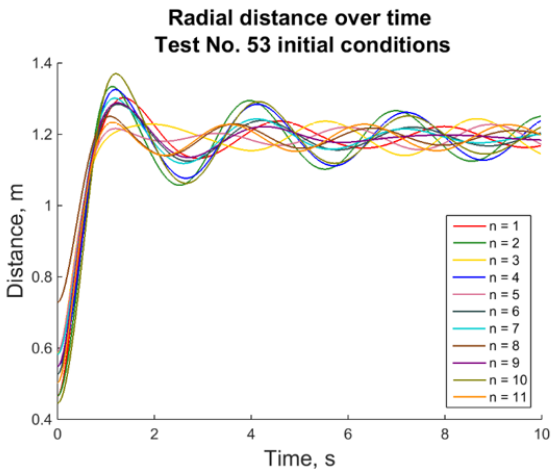

Test 54 data and model predictions

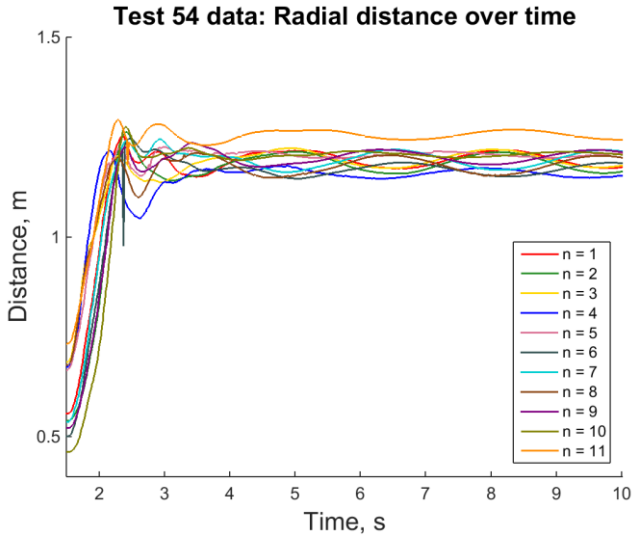

k = 6.9 N/m, c = 14 N-s/m

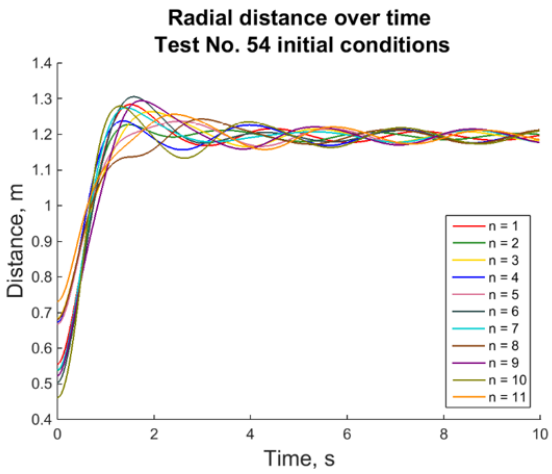

t < 1.5 s: k = 27 N/m, c = 20 N-s/m
t ≥ 1.5 s: k = 5 N/m, c = 15 N-s/m

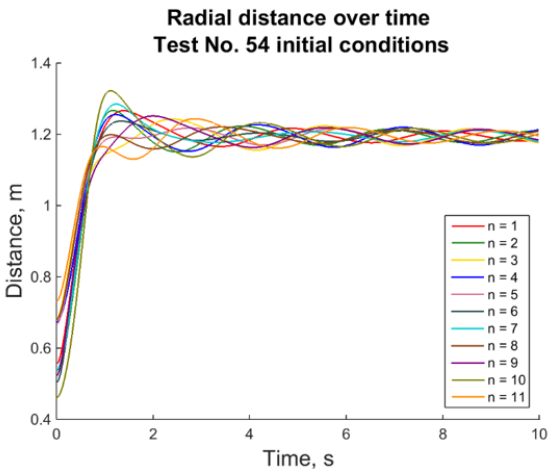

Test 55 data and model predictions

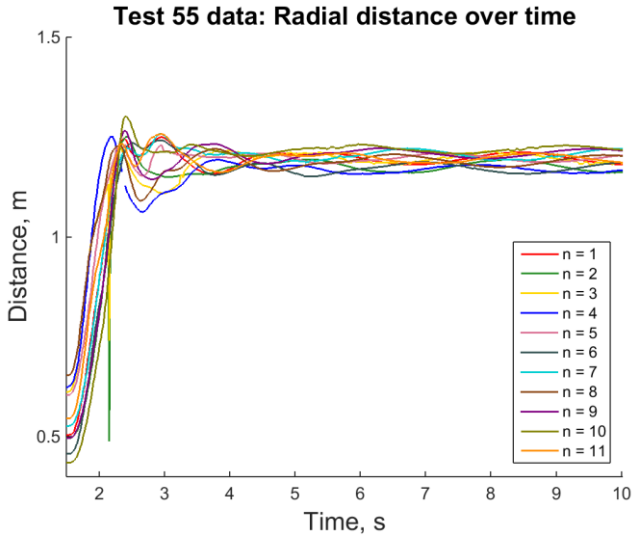

k = 6.9 N/m, c = 14 N-s/m

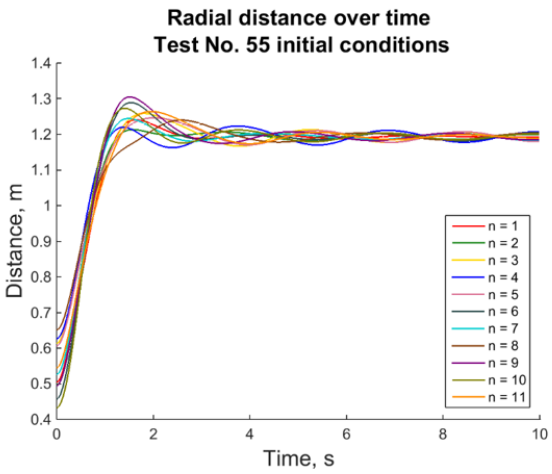

t < 1.5 s: k = 25 N/m, c = 20 N-s/m
t ≥ 1.5 s: k = 1 N/m, c = 10 N-s/m

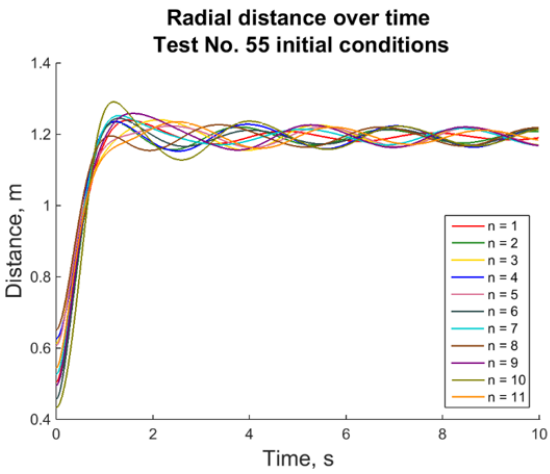

References

[1] Super Power, "SuperPower® 2G HTS Wire Specifications," URL: http://www.superpower-inc.com/ [cited 23 Jan. 2014].

[2] Villani, D.D., Landecker, P.B., Hughes Electronics Corporation, El Segundo, CA, U.S. Patent Application for "Magnetic Systems and Methods for Realizing Spacecraft Maneuvers," Patent No. 6,089,510, filed 18 Jul. 2000.

[3] Kwon, D.W., Sedwick, R.J., Sakaguchi, A., "Micro-electromagnetic Formation Flight of Satellite Systems," *AIAA SPACE 2010 Conference & Exposition*, Anaheim, California, 2010.

[4] Porter, A.K., Alinger, D.J., Sedwick, R.J., Merk, J., Opperman, R.A., Buck, A., Eslinger, G., Fisher, P., Miller, D.W., Bou, E., "Demonstration of Electromagnetic Formation Flight and Wireless Power Transfer", J*ournal of Spacecraft and Rockets*, Vol. 51, No. 6, 2014, pp. 1914-1923. doi: 10.2514/1.A32940

[5] Kwon, D.W., Sedwick, R.J., Lee, S., Ramirez-Riberos, J.L., "Electromagnetic Formation Flight Testbed Using Superconducting Coils," *Journal of Spacecraft and Rockets*, Vol. 48, No. 1, Jan-Feb 2011, pp. 124-134.

[6] Tesla, N., "Experiments with Alternate Currents of High Potential and High Frequency," Institution of Electrical Engineers, London, England, 1892.

[7] Sedwick, R.J. "Long range inductive power transfer with superconducting oscillators", *Annals of Physics*, Vol. 325, 2010, pp. 287–299. doi:10.1016/j.aop.2009.08.011

[8] Alinger, D.J., Porter, A.K., Sedwick, R.J., "Optimization of Resonant Inductive Wireless Power Transfer Using Multi-layer Flat Spiral Coils", *Journal of Spacecraft and Rockets*, Vol. 52, No. 2 (2015), pp. 560-568. doi: 10.2514/1.A32901

[9] Levy, R. H., "Radiation Shielding of Space Vehicles by Means of Superconducting Coils," *American Rocket Society*, Vol 31, Iss. 11, pp 1568-1570.

[10] Shepard, S.G., Shepard J.P.G., "Toroidal Magnetic Spacecraft Shield Used to Deflect Energetic Charged Particles," *Journal of Spacecraft and Rockets*, Vol. 46, No. 1, Jan-Feb 2009, pp. 177-184.

[11] Cocks, F.H., "A Deployable High Temperature Superconducting Coil," *Journal of the British Interplanetary Society*, Vol. 44, 1991, pp 99-102.

[12] Cocks, J.C., Watkins, S.A., Cocks, F.H., Sussingham, C., "Applications for Deployed High Temperature Superconducting Coils in Spacecraft Engineering: A Review and Analysis," *Journal of the British Interplanetary Society*, Vol. 50, 1997, pp. 479-484.

[13] Schenck, J.F., "Safety of Strong, Static Magnetic Fields," *Journal of Magnetic Resonance Imaging*, Vol. 12, Iss. 1, Jul 2000, pp 2-19.

[14] Kervendal, E.A., Kirk, D.R., Meinke, R.B., "Spacecraft Radiation Shielding Using Ultralightweight Superconducting Magnets," *Journal of Spacecraft and Rockets*, Vol. 46, No. 5, Sept-Oct 2009, pp. 982-988.

[15] Joshi, R.P., Qiu, H., Tripathi, R.K., "Evaluation of a Combined Electrostatic and Magnetostatic Configuration for Active Space-radiation Shielding," *Advances in Space Research*, Vol. 51, 2013, pp. 1784-1791.

[16] Thienel, L., Lewis, M.R., Brennan, P.J., Buchko, M., Glaister, D., Stoyanof, M., "Design and Performance of the Cryogenic Flexible Diode Heat Pipe (CRYOFD) Flight Experiment," Air Force Research Laboratory, Society of Automotive Engineers, Inc, 1998.

[17] Kwon, D.W., Sedwick, R.J., "Cryogenic Heat Pipe for Cooling High-Temperature Superconducting Coils," *Journal of Thermophysics and Heat Transfer*, Vol. 23, No. 4, 2009, pp. 732-740. DOI: 10.2514/1.43728

[18] Chen, J., Guo, Z., Yu, W., "Heat Transfer Analysis of Insulation Materials with Flexible Multilayers," *Thermal Science*, Vol. 17, No. 5, 2013, pp. 1415-1420.

[19] Neumann, H., "Concept for Thermal Insulation Arrangement within a Flexible Cryostat for HTS Power Cables," *Cryogenics*, Vol. 44, 2004, pp. 93-99.

[20] Finckenor, M.M., Dooling, D., NASA Multilayer Insulation Material Guidelines, 1999

[21] Okazaki, S., Kawasaki, H., Murakami, M., Sugita, H., Kanamori, Y., "Influence of Processing on Thermal Performance of Space Use Multilayer Insulation," *Journal of Thermophysics and Heat Transfer*, Vol. 28, No. 2, 2014, pp. 334-342. DOI: 10.2514/1.T4163

[22] Donabedian, M., Gilmore, D.G., Stultz, J.W., Tsuyuki, G.T., Lin, E.I., "Insulation", *Spacecraft Thermal Control Handbook: Volume 1: Fundamental Technologies*, The Aerospace Press, El Segundo, 2002, pp. 161-205.

[23] Lin, E.I., Stultz, J.W., Reeve, R.T., "Effective Emittance for Cassini Multilayer Insulation Blankets and Heat Loss near Seams," *Journal of Thermophysics and Heat Transfer*, Vol. 10, No. 2, 1996, pp. 357-363. DOI: 10.2514/3.795

[24] Ross, R.G., Boyle, R.F., "An Overview of NASA Space Cryocooler Programs – 2006," *Cyrocoolers 14*, International Cryocooler Conference, Boulder, CO, 2006, pp. 1-10.

[25] Johnson, D.L., Carroll, B.C., Leland, R.S., "MSL/CheCheMin Cryocooler System Requirements and Characterization Tests," *Cryocoolers 15*, International Cryocoolers Conference, Boulder, CO, 2009, pp. 621-630.

[26] Zia, J.H., "A Pulse Tube Cryocooler with 300 W Refrigeration at 80 K and an Operating Efficiency of 19% Carnot" *Cyrocoolers 14*, International Cryocooler Conference, Boulder, CO, 2007, pp. 141-147.

[27] Ross, R.G Jr., Johnson, D.L., Elliott, D., Licata, S.J., Overoye, K., "AIRS Pulse Tube Coolers Performance Update – Six Years in Space," *Cryocoolers 15*, International Cryocooler Conference, Boulder, CO, 2009, pp. 613-620.

[28] Sunpower, Inc., "CryoTel® Family," URL: http://sunpowerinc.net/cryocoolers/cryotel [cited: 27 March 2014].

[29] van de Groep, W.L., Mullié, J.C., Willems, W.J., Benschop, T., "Development of a 15W Coaxial Pulse Tube Cooler," *Cryocoolers 15*, International Cryocooler Conference, Boulder, CO, 2009, pp. 157-165.

[30] Barr, M.C., Price, K.D., Pruitt, G.R., "Raytheon RS1 Cryocooler Performance," *Cryocoolers 13*, Springer Science+Business Media, Inc., New York, 2004, pp. 59-63.

[31] Dietrich, M., Yang, L.W., Thummes, G., "High-power Stirling-type pulse tube cryocooler: Observation and reduction of regenerator temperature-inhomogeneities," *Cryogenics*, Vol. 47, 2007, pp. 306-314.

[32] Nguyen, T., Petach, M., Michaelian, M., Raab, J., Tward, E., "Space Micro Pulse Tube Cooler," *Cryocoolers 16*, International Cryocooler Conference, Boulder, CO, 2011, pp. 97-101.

[33] Ladner, D.R., "Performance and Mass vs. Operating Temperature for Pulse Tube and Stirling Cryocoolers," Cryocoolers 16, International Cryocooler Conference, Boulder, CO, 2011, pp. 633-644.

[34] Trollier, T., Tanchon, J., Buquet, J., Ravex, A., "Status of Air Liquide Space Pulse Tube Cryocoolers," *Cryocoolers 15*, International Cryocooler Conference, Boulder, CO, 2009, pp. 115-123.

[35] Nguyen, T., Toma, G., Jaco, C., Michaelian, M., Raab, J., "HEC Pulse Tube Coaxial Cold Head Coolers," *Cryocoolers 16*, International Cryocooler Conference, Boulder, CO, 2011, pp. 143-148.

[36] Swift, W.L., McCormack, J.A., Zagarola, M.V., Dolan, F.X., Sixsmith, H., "The NICMOS Turbo-Brayton Cryocooler – Two Years in Orbit," *Cryocoolers 13*, Springer Science+Business Media, Inc., New York, 2004, pp. 633-639.

[37] Brandon, E., Vozoff, M., Kolawa, E.A., Studor, G.F., Lyons, F., Keller, M.W., Beiermann, B., White, S.R., Sottos, N.R., Curry, M.A., Banks, D.L., Brocato, R., Zhou, L., Jung, S., Jackson, T.N., Champaigne, K., "Structural health management technologies for inflatable/deployable structures: Integrating sensing and self-healing," *Acta Astronautica*, Vol. 68, 2011, pp. 883-903.

[38] Freeland, R.E., Bilyeu, G., "IN-STEP Inflatable Antenna Experiment," *Acta Astronautica*, Vol. 30, 1993, pp. 29-40.

[39] Freeland, R.E., Bilyeu, G., "IN-STEP Inflatable Antenna Experiment," *Acta Astronautica*, Vol. 30, 1993, pp. 29-40.

[40] Freeland, R.E., Bilyeu, G.D., Veal, G.R., "Validation of a Unique Concept for a Low-cost, Lightweight Space-deployable Antenna Structure," *Acta Astronautica*, Vol. 35, No. 9-11, 1995, pp. 565-572.

[41] Freeland, R.E., Bilyeu, G.D., Veal, G.R., "Development of Flight Hardware for a Large, Inflatable-deployable Antenna Experiment," *Acta Astronautica*, Vol. 38, No. 4-8, 1996. Pp. 251-260.

[42] Freeland, R.E., Bilyeu, G.D., Steiner, M.D., Carson, D.E., "Large Inflatable Antenna Flight Experiment Results," *Acta Astronautica*, Vol. 41, No. 4-10, pp. 267-277.

[43] Huang, J., "The Development of Inflatable Array Antennas," *IEEE Antennas and Propagation Magazine*, Vol. 43, No. 4, Aug. 2001, pp. 44-50.

[44] Pappa, R.S., Lassiter, J.O., Ross, B.P., "Structural Dynamics Experimental Activities in Ultralightweight and Inflatable Space Structures," *Journal of Spacecraft and Rockets*, Vol. 40, No. 1, 2003.

[45] Gajbhiye, S.C., Upadhyay, S.H., Harsha, S.P., "Vibration Analysis of an Inflatable Torus Based on Mode Shape," *AIAA Journal: Technical Notes*, Vol. 51, No. 6, Jun 2013, pp. 1526-1531.

[46] Rohsenow, W.M., Hartnett, J.P., Cho, Y.I., *Handbook of Heat Transfer*, 3rd ed., McGraw-Hill, New York, 1998, pp. 5.32-5.44.

[47] Incropera, F.P., and DeWitt, D.P., *Fundamentals of Heat and Mass Transfer*, 6th ed., John Wiley & Sons, New Jersey, 2007, pp. 488-491.

[48] Wertz, J. R., and Larson, W. J., "Space Mission Analysis and Design", 3rd ed., Microcosm Press, 1999

[49] Brewster, M.Q., Thermal Radiative Transfer and Properties, John Wiley & Sons, Inc, New York, 1992, pp. 501.

[50] Wertz, J.R., and Larson, W.J., *Space mission analysis and design*, 3rd ed., Space Technology Library, 1999, pp. 332-335.

[51] Johnson, W., Fesmire, J., "Thermal performance of low layer density multilayer insulation using liquid nitrogen", *AIP Conference Proceedings*, Vol. 1434, 2012, pp. 39-46. doi: 10.1063/1.470690

[52] Brandon, E., Vozoff, M., Kolawa, E.A., Studor, G.F., Lyons, F., Keller, M.W., Beiermann, B., White, S.R., Sottos, N.R., Curry, M.A., Banks, D.L., Brocato, R., Zhou, L., Jung, S., Jackson, T.N., Champaigne, K., "Structural health management technologies for inflatable/deployable structures: Integrating sensing and self-healing," *Acta Astronautica*, Vol. 68, 2011, pp. 883-903.

[53] Hager, M.D., Greil, P., Leyens, C., van der Zwaag, S., Schubert, U.S., "Self-Healing Materials", *Advanced Materials*, Vol. 22, No. 47, 2010, pp. 5424-5430. doi: 10.1002/adma.201003036

[54] Corten, C.C., Urban, M.W., "Repairing Polymers Using an Oscillating Magnetic Field", *Advanced Materials*, Vol. 21, 2009, pp. 5011-5015. doi: 10.1002/adma.200901940

[55] Zhong, N., Post, W., "Self-repair of structural and functional composites with intrinsically self-healing polymer matrices: A review", Composites: Part A, Vol. 69, 2015, pp. 226-239. doi: 10.1016/j.compositesa.2014.11.028

[56] White, S.R., Sottos, N.R., Geubelle, P.H., Moore J.S., Kessler, M.R., Sriram, S.R., Brown, E.N., Viswanathan, S., "Autonomic healing of polymer composites", Nature, Vol. 409, 2001, pp. 794-817. doi: 10.1038/35057232

[57] Ferl, J., Ware, J., Cadogan, D., Yavorsky, J., "Self-healing Technology for Gas Retention Structures and Space Suit Systems", *SAE International*, 2007. doi: 10.4271/2007-01-3211

[58] Rampf, M., Speck, O., Speck, T., Luchsinger, R.H., "Investigation of a fast mechanical self-repair mechanism for inflatable structures", *International Journal*

of Engineering Science, Vol. 63, 2013, pp 61-70. doi: 10.1016/j.ijengsci.2012.11.002